THE UNIVERSITY OF CHICAGO

THERMAL AND MAGNETIC HISTORY OF ROCKY EXTRA-SOLAR PLANETS

A DISSERTATION SUBMITTED TO
THE FACULTY OF THE DIVISION OF THE PHYSICAL SCIENCES
IN CANDIDACY FOR THE DEGREE OF
DOCTOR OF PHILOSOPHY

DEPARTMENT OF ASTRONOMY AND ASTROPHYSICS

BY

JISHENG ZHANG

CHICAGO, ILLINOIS
DECEMBER 2023

Dedicated to my parents, friends and mentors, without whom I could not finish this dissertation

TABLE OF CONTENTS

LIST OF FIGURES

LIST OF TABLES

ABSTRACT

Planetary-scale magnetic fields provide a unique window into a planet's deep interior. From the magnetic field of Earth to that of Jupiter, the existence of such fields is tied to the presence of an electrically conductive convecting fluid (dynamo source region) in the interior. Thus, detections of planetary-scale magnetic field signals offer constraints on the planets' thermal state, interior structure, and dynamics. In this thesis, we present thermal evolution calculations for rocky exoplanets. We aim to determine whether super-Earths can host dynamo-generated magnetic fields and explore how dynamo lifetimes scale with planet properties (such as planet mass, $M_{\rm pl}$, and core mass fraction, CMF). To achieve this, we couple a 1D thermal evolution model with a Henyey solver to calculate their thermal evolution. The code solves the energy balance equation in the iron-dominated core and the silicate mantle. We use a modified mixing length formulation to model convection in the silicate mantle with low and high Reynolds numbers. In addition, by including the Henyey solver, the model self-consistently accounts for adjustments in the interior structure as the planet evolves in time. We explore the possibility of the planet hosting a dynamo source in its iron-dominated core and/or magma ocean. We find that the heat loss rate of the core scales with $M_{\rm pl}$. This results in a greater dynamo lifetime in the core of a more massive planet with $M_{\rm pl} < 6M_{\oplus}$. However, for planets with $M_{\rm pl} > 6M_{\oplus}$, the core fully solidifies before liquid core convection shuts off. The dynamo lifetime in the core decreases with increasing $M_{\rm pl}$, owing to the short lifetime of the liquid core associated with the high core heat loss rate. In addition, a magma ocean could only host a dynamo if its melt fraction is high enough to have liquid-like convection. The dynamo in the magma ocean in an Earth-like planet ($M_{\rm pl} = 1M_{\oplus}$, CMF=0.33 and $T_{\rm pl} = 255$K) could only last $\sim$0.25 Myr. However, a magma ocean may sustain a long-term dynamo on a lava planet or a sub-Neptune, whose silicate mantle could stay molten or partially molten on a billion-year timescale. Future studies of these planets may shed light on the role of a magma ocean sustaining a planetary-scale magnetic field.

CHAPTER 1

INTRODUCTION

Planetary magnetic fields are ubiquitous in the solar system and the explanation for their existence has been linked to planetary interiors. Strong planet-scale magnetic fields have been detected for Mercury, Earth, Ganymede, and all of the gas giants in the solar system [Ness et al., 1975, 1986, 1989, Finlay et al., 2010, Kivelson et al., 1996, Burke and Franklin, 1955, Smith et al., 1980]. These magnetic fields have been attributed to dynamo currents, which are generated by thermal convection, compositional convection, differential rotation, or a combination of several processes within the planetary interior. Consequently, the presence or absence of strong planet-scale magnetic fields constrains the planet's thermal evolution history and interior dynamics. For example, the discovery of Jupiter's magnetic field indicates a convectively-driven dynamo action in the electrically conductive metallic hydrogen layer [Stanley and Glatzmaier, 2010], whereas the lack of a magnetic field for Venus indicates an inefficient core cooling rate due to the lack of plate tectonics [Stevenson, 2010].

The observational detection of an exoplanet's magnetic field would open an unprecedented window into exoplanet interiors and add a new dimension to exoplanet characterization. To date, the characterization of exoplanets has largely focused on their shrouding atmospheres, mass-radius relationships and orbital architectures. Radius and mass measurements derived from transit photometry and radial velocity data constrain planetary average densities and bulk compositions. Additionally, transmission and emission spectroscopy provide information about the atmospheric thermal budget and chemical composition. However, exoplanet interior structure and dynamics remain ambiguous. The interpretation of planet mass-radius measurements suffers from degeneracies; a single mass-radius measurement can be consistent with various bulk compositions and interior structures [e.g., Adams et al., 2008, Rogers and Seager, 2010]. Eventually, observational measurements of exoplanet magnetic fields may extend the current mass-radius relationship to a mass-radius-magnetic field strength diagram and help reduce the degeneracy in the interpretation. Most generally, a strong planetary

scale magnetic field requires an electrically conductive convecting fluid region within the planet. In the case of a rocky exoplanet, a magnetic field detection would imply the existence of a convecting liquid iron core or a layer of molten silicate in the mantle [Soubiran and Militzer, 2018].

Detection of planetary-scale magnetic fields on planets with a range of atmosphere compositions enables studies of the influence of magnetic fields on atmosphere preservation. The comparison among the atmospheres of Earth, Venus and Mars is often used to argue that a dynamo-generated magnetic field could protect the atmosphere of a rocky planet from losing its water [Lundin et al., 2007]. However, the mechanism of such protection remains unclear. Moreover, despite of Earth having a global magnetic field, its atmosphere loss rate is comparable to other rocky planets in the solar system [Gunell et al., 2018]. Ideally, a large sample of planets with a range of atmospheric compositions and magnetic field properties will allow studies of the interactions between magnetic fields and atmosphere loss rate. The results would have implications for the assessment of the habitability of exoplanets, and complement the current focus on biosignatures in exoplanetary spectra.

Given the importance of dynamo-generated magnetic fields, their detection will be a frontier in exoplanetary science in the coming decades. So far, various groups have looked for observational signatures of magnetic fields from exoplanets [e,g., Winterhalter et al., 2006, Zarka, 2007, Hallinan et al., 2013]. Kao et al. [2018] determined the magnetic field strength of a brown dwarf by detecting its radio aurora emission. The recently commissioned Low Frequency Array [LOFAR, van Haarlem et al., 2013] and Long Wavelength Array [LWA, Ellingson et al., 2009] reach $\sim$mJy sensitivities at frequencies below 100MHz, enabling searches for the magnetic fields of gas giants. Using LOFAR, Turner et al. [2020] detected radio signals from τ Boötis and ν Andromedae systems, which are attributed to the self-sustaining magnetic fields of Jovian-sized planets. Due to their weaker expected magnetic field strength [$\lesssim 3G$, Bonati et al., 2021], detections of radio signals from sub-Neptunes and

super-Earths may require observations at frequency below 10 MHz, which are inaccessible to ground-based telescopes due to Earth's ionospheric cutoff. The Sun Radio Interferometer Space Experiment [SunRISE, Alibay et al., 2017] is a spaced-based telescope designed to study the sun at frequencies below 15 MHz. SunRISE will not be sensitive enough to detect exoplanets, but may observe auroral emission from Saturn, and thus prove the concept of using space-based telescopes to detect planetary radio aurora in a bandpass below 15 MHz. To guide future surveys for exoplanetary magnetic fields and to eventually translate detected signals into constraints on the planets' interior structure and dynamics, extensive modeling of the thermal evolution history of exoplanets across a range of masses, compositions, and stellar incident flux is needed.

Multiple groups have investigated the thermal and magnetic evolution of rocky planets using a box model [e.g., Stevenson et al., 1983, Papuc and Davies, 2008, Driscoll and Bercovici, 2014]. In their models, the mantle and core are treated as two boxes, and the thermal history is described by the time evolution of the average mantle and core temperatures. The heat flow throughout the planet is evaluated by modeling conduction across the thermal-boundary layers at the core-mantle boundary (CMB) and the planetary surface. Under the assumption of whole mantle convection, the heat flow across the thermal boundary layers are set by the critical Rayleigh number, a dimensionless number describing the onset of convection flow. Boundary layer theory and box models are effectively zero-dimensional energy-balance models. The thermophysical properties of mantle and core materials (e.g., heat capacity, viscosity, and thermal expansion coefficient) are modeled with an effective value that is constant throughout each "box" (upper mantle, lower mantle, core, and thermal boundary layers). They are not true 1-D treatments wherein thermophysical and structure quantities are calculated as a function of radius. In addition, with constant pressure and density profiles adopted for the core and mantle, the work done by planet expansion/contraction is not self-consistently included.

We have developed a new fully 1-D thermal evolution model for rocky planets to explore the possibility of molten silicate or liquid iron serving as dynamo source regions. Our code solves for the radial distribution of temperature, melt fraction, pressure, density, and conductive and convective heat fluxes, and evolves these profiles forward in time. Thermophysical properties that affect the planet's structure and evolution, such as viscosity and thermal expansion coefficient, are evaluated based on the local pressure and temperature. We use a generalized Schwarzschild criterion based on the density gradient to determine where convection occurs in the mantle and a modified mixing length theory to model the convective heat flow. The mixing length theory is traditionally used to estimate the convective heat flow of an inviscid fluid [e.g. heat transport in stars, Vitense, 1953]. The modified formulation [e.g., Sasaki and Nakazawa, 1986a, Abe, 1995, Tachinami et al., 2011, Wagner et al., 2019] accounts for the viscous drag force induced by viscous fluid with a small Reynolds number, such as solid phase mantle silicate. We further extend the modified mixing length theory to estimate the convective heat flow in both single- and multi-phase regions (Appendix 2.B). Additionally, we include a Henyey solver (section 2.2) to adjust the pressure and density profiles within the model as the planet cools. This feature allows us to include heating (cooling) due to planetary contraction (expansion) self-consistently. The ultimate output is to obtain the time evolution of the convective heat flow throughout the planet, which we use to determine the location and duration of possible dynamo source regions.

In this dissertation, we aim to explore the effect of planet mass and core mass fraction on the rocky planet thermal and magnetic history, and assess which combinations of these two parameters would lead to the greatest predicted dynamo lifetime. In chapter 2, we describe the theoretical framework to calculate planet interior and thermal evolution. In chapter 3, we validate our modeling approach by computing the thermal and magnetic history of an Earth-like case and comparing results to previous work and observations of Earth. In chapter 4, we present results for a grid of planets with planet masses between 1 and $8 M_{\oplus}$ and core

mass fractions between 0.1 and 0.8. Lastly, we offer a brief description of ways to further improve our model and ideas to utilize our model to explore thermal evolution of exoplanets.

CHAPTER 2

METHODOLOGY

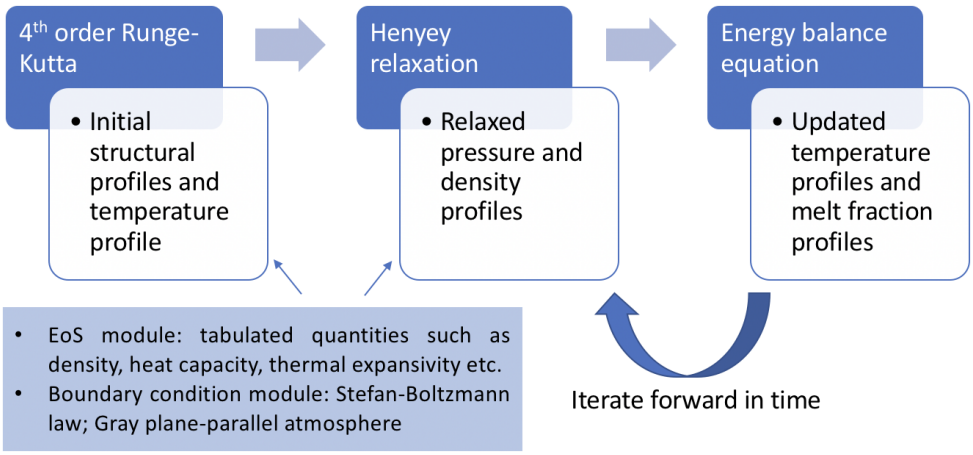

Figure 2.1: Algorithm of the model. Initial profiles are prepared in step 1. Subsequent updates in temperature, melt fraction and structural profiles are carried out by iterating step 2 and 3.

2.1 Introduction

We have developed a 1-D spherically symmetric discretized model to simulate the thermal evolution of rocky planets as they cool from an initial post-formation hot state with a liquid iron core and molten silicate mantle. We apply the model to explore the impact of planetary mass ($M_{\rm pl}$), core mass fraction (CMF), and equilibrium temperature ($T_{\rm eq}$) on the thermal history of rocky planets and the timing and duration of possible dynamos in both the liquid core and magma ocean.

We consider planets consisting of a silicate mantle surrounding a iron dominated core with 10% light elements by mass. Future work will explore the effect of different chemical compositions in the core and mantle as well as the level of differentiation between the iron and silicates in the planets.

The overall algorithm is briefly summarized in figure 2.1 and here:

1. The planet is discretized radially into multiple cells with equal mass in the core and mantle depending on M_{pl} and CMF. An initial structure profile, including radius (r), pressure (P) and density (ρ) as a function of mass interior (m), is prepared by in-

tegrating the structural equations (section 2.2) with appropriate equations of state (EoS, section 2.3) using a fourth order Runge-Kutta method. A hot adiabatic initial temperature profile (T) is assumed in both the core and the mantle.

2. The solution to the interior structure (r, P and ρ as a function of m) — be it the initial structure from step 1 or a subsequent structure updated after a thermal timestep from step 3 — is updated by a Henyey solver (section 2.2) so that it satisfies the boundary conditions at both the center and the surface. The relative tolerance in the Henyey relaxation for both radius and pressure is set to be 10^{-4}.

3. A new thermal profile at the new thermal timestep, $t + \Delta t$, is obtained by solving the energy balance equation in both the core and the mantle (sections 2.4 and 2.5). The surface heat flow is set by gray-body radiation with an emissivity of one. The cooling rate of the core is determined by heat conduction through the core-mantle boundary as well as the rate of inner solid core nucleation. Radial profiles of thermophysical properties, such as viscosity, are updated based on the new thermal profile.

Time evolution is calculated by iterating steps 2 and 3 forward in time.

Compared to a parameterized model [e.g., Papuc and Davies, 2008, Driscoll and Bercovici, 2014] that estimates the convective flux under the assumption of whole mantle convection using a global Rayleigh number, our approach has two key advantages. First, our model takes variations of thermophysical properties with depth in the planet into account. Second, instead of assuming whole mantle convection, we directly evaluate which layers are unstable to convection with a generalized Schwarzschild criterion based on the entropy gradient.

In the rest of the section, we explain each component in more detail. We discuss the interior structure calculation in section 2.2, choice of bulk composition and the corresponding equation of state (EoS) in section 2.3, energy transport in the core and the mantle in sections 2.4 and 2.5, mantle viscosity in section 2.6, internal heat production in section 2.7,

initial conditions in section 2.8, boundary conditions in section 2.9, and the dynamo criterion in section 2.10.

2.2 Interior structure

We consider a spherically symmetric planet that evolves quasi-statically in hydrostatic equilibrium. In our interior structure model, the iron core and silicate mantle are each divided into hundreds to thousands of cells with equal mass of dm (a Langrangian formulation), depending on M_{pl} and CMF. For example, the iron core and silicate mantle of an Earth-like planet ($M_{pl} = 1M_{\oplus}$ and CMF=0.326) are each divided into 1000 cells. At each instant in time, the interior structure is described by the following coupled differential equations for radius $r(m)$ and pressure $P(m)$:

$$\frac{\partial r}{\partial m} = \frac{1}{4\pi r^2 \rho}, \tag{2.1}$$

$$\frac{\partial P}{\partial m} = -\frac{Gm}{4\pi r^4}, \tag{2.2}$$

where r is the radial distance from the center of the planet, G is the gravitational constant, and ρ is the local density, calculated based on the EoS (described in section 2.3) for a given material at the local pressure and temperature level.

The coupled differential equations 2.1 and 2.2 have boundary conditions at both the center and the surface. The radius at the center ($m = 0$) is to 0, while the pressure level at the surface ($m = M_{pl}$) is set by the atmospheric boundary condition (herein chosen to be 1 bar). A detailed description of the surface boundary conditions can be found in section 2.9.

To start the evolution, the initial structure profile is obtained by numerically solving the above differential equations using a fourth order Runge-Kutta technique integrating from the planet center to the surface (a shooting technique). We set the initial temperature

at the planet center to be 500 K above the melting temperature. The initial temperature distribution in the core and the mantle is assumed to be adiabatic. Our choice of the initial temperature distribution is hot enough such that both the core and the mantle are fully molten. We reiterate the shooting technique to search for an appropriate central pressure corresponding to the chosen M_{pl} and CMF until the surface pressure satisfies the surface boundary condition with a relative error less than 10^{-4}. The resulting solution is fed into the Henyey solver (discussed below) to further reduce the relative error in the surface pressure.

When applying shooting techniques (like the well-known Runga-Kutta method) to model the planet interior structure, the boundary conditions are only fully satisfied at either the planet surface (when integrating from the outside in) or at the center (when integrating from the inside out), not both. Iteration is needed to reach a solution that satisfies the second boundary condition within a preset tolerance. For example, when setting the initial starting structure, we iterate to find the central pressure corresponding to the desired total planet mass, M_{pl}, whereas other models that apply a shooting method to integrate from the outside in [e.g. Valencia et al., 2006, Rogers and Seager, 2010] iterate to solve for the total planet radius that leads to $r \approx 0$ at $m = 0$. To model the detailed time evolution and energy transport throughout the planet, it is necessary to simultaneously match the boundary conditions at the center and the surface.

We use a Henyey solver [Henyey et al., 1959], an implicit iterative Newton-Raphson integration scheme, to solve equations 2.1 and 2.2, while simultaneously satisfying the specified boundary conditions at both the planet center and the surface. The Henyey solver approximates the spatial derivatives in equations 2.1 and 2.2 at the boundary between two adjacent mass cells using the finite difference method, resulting in $2(n-1)$ difference equations for n mass cells. Together with 2 boundary conditions at planet center and surface, there are $2n$ equations governing $2n$ unknowns (P and r at each cell). Provided with an approximated solution to the unknowns, an improved solution can be found with the Newton-Raphson

method. The Henyey solver iterates the procedure a few times until a converged solution is reached (i.e. the maximum change in the radius and pressure profiles is less than the relative tolerance of 10^{-4}). We run the Henyey solver after each thermal timestep to update the radius, pressure, and volume of each cell based on the new temperature and melt fraction profiles. A major advantage of the method is that it can reach convergence rapidly given a reasonable starting point (which, in our case, is the solution for the pressure and radius profiles at the previous timestep). On top of this, adjustments in the interior structure due to phase transitions in the mantle and core are taken into account self-consistently.

2.3 Bulk composition and EoS

The density within each layer is calculated based on the composition and the appropriate choice of EoS, which is a unique function that relates density to temperature and pressure for a given material. Our code is modular and could be readily extended to include EoS options in addition to the ones described in this section, enabling sensitivity analyses over the uncertainty of various EoSs and assumed compositions (for example, MAGARATHEA compiles a list of EoSs appropriate for mantles and cores of super-Earths [Huang et al., 2022]). However, this is beyond the scope of this thesis. For this thesis, we have chosen a set of EoSs that are semi-empirical fits to experimental data by high-pressure experiments or *ab initio* calculations. In this section, we will discuss the bulk composition of the planets and the choice of EoS for the individual materials.

2.3.1 Composition and phase structure

In this study, we consider terrestrial planets with a iron-dominated core with 10wt% of Si and a $MgSiO_3$ mantle. The mantle is molten while the local temperature is above the liquidus of $MgSiO_3$, solid below the solidus of $MgSiO_3$ and a mixture of liquid and solid in between.

We adopt the solidus and liquidus for $MgSiO_3$ in [Stixrude, 2014] for post-perovskite,

$$\begin{aligned} T_{\mathrm{l,ppv}} &= 5400\mathrm{K}\left(\frac{P_{\mathrm{GPa}}}{140\mathrm{GPa}}\right)^{0.48} \\ T_{\mathrm{s,ppv}} &= T_{\mathrm{l,ppv}}(1-\log 0.79)^{-1}, \end{aligned} \tag{2.3}$$

where P_{GPa} is the value of pressure in GPa. For enstatite and bridgmanite, we consider the liquidus and solidus for the bulk silicate Earth from Fiquet et al. [2010] and Suer et al. [2021],

$$\begin{aligned} T_{\mathrm{l,bse}} &= 2022 + 54.21P_{\mathrm{GPa}} - 0.34P_{\mathrm{GPa}}^2 + 9.0747\times10^{-4}P_{\mathrm{GPa}}^3 \\ T_{\mathrm{s,bse}} &= 1621 + 38.415P_{\mathrm{GPa}} - 0.1958P_{\mathrm{GPa}}^2 + 3.8369\times10^{-4}P_{\mathrm{GPa}}^3. \end{aligned} \tag{2.4}$$

The latent heat release upon melting of mantle silicate, L, is 7.322×10^5 J kg^{-1}[Hess, 1990].

Upon solidification, the mantle is further divided into 3 layers consisting of enstatite, bridgmanite and post-perovskite from low to high pressures. The pressure-induced phase transition from enstatite to bridgmanite has a Clapeyron slope of -0.0013 GPa K^{-1}[Fei et al., 2004], and from bridgmanite to post-perovskite 8.5 MPa K^{-1}[Sun et al., 2018]. A study exploring other choices for the Mg/Si ratios in the mantle will be pursued in the future.

The iron-dominated core is divided into a solid inner core and a liquid outer core. For the melting cuvre of pure Fe, we adopt the *ab initio* simulation results from Morard et al. [2011] fitted by a Simon-like power law [Stixrude, 2014],

$$T_{\mathrm{Fe}} = 6500\mathrm{K}\left(\frac{P}{340\mathrm{GPa}}\right)^{0.515}. \tag{2.5}$$

The cores of rocky exoplanets are unlikely to be pure Fe. The exact composition of the cores depend on the composition of host stars and the formation history of individual planets. For this project, we consider 10wt% of silicon in the iron-dominated cores as a proxy for impurities. To account for freezing point depression owing to impurities in the liquid cores,

we estimate the freezing point using a cryoscopic equation [Stixrude, 2014],

$$T_{\mathrm{FeSi}} = T_{\mathrm{Fe}}(1 - \log x_0)^{-1}, \tag{2.6}$$

where x_0 is the molar fraction of Fe. The latent heat of fusion of iron due to core nucleation, L_{Fe}, is $1.2 \times 10^6 \mathrm{Jkg}^{-1}$[Anderson and Duba, 1997].

As the inner core solidifies, various amount of impurities is exsoluted into the liquid core depending on the partition of the specific impurity between solid- and liquid-phase Fe. We consider two extreme scenarios where the impurities are either distributed evenly throughout the core and the dynamo is driven by thermal convection alone, or all impurities are partitioned into the liquid outer core and the dynamo is driven by both thermal and compositional convection.

2.3.2 EoS of molten silicate

For molten silicate, we adopt the recently developed EoS for liquids under high temperature and pressure conditions [Wolf and Bower, 2018]. The EoS comprises an isothermal component and a thermal perturbation described by the generalized Rosenfeld-Tarazona model [Rosenfeld and Tarazona, 1998]. The EoS reads

$$P(\rho, T) = P(\rho, T_0) + \Delta P_E(\rho, T) + \Delta P_S(\rho, T), \tag{2.7}$$

where the first term on the right is the isothermal component and the second and the third terms are the energetic and entropic contributions to the thermal perturbation. The isothermal component is given by the Vinet EoS [Vinet et al., 1989],

$$P(\rho, T_0) = 3K_0 \left(\frac{\rho}{\rho_0}\right)^{2/3} \left[1 - \left(\frac{\rho}{\rho_0}\right)^{-1/3}\right] \exp\left[\frac{3}{2}\left(K_0' - 1\right)\left(1 - \left(\frac{\rho}{\rho_0}\right)^{-1/3}\right)\right], \tag{2.8}$$

where T_0 is the reference temperature of 3000 K, and ρ_0, K_0, and K_0' are the density, isothermal bulk modulus, and derivative of isothermal bulk modulus at the reference temperature and zero pressure. The thermal perturbation terms, which are described by the generalized Rosenfeld-Tarazona model, are written as:

$$\begin{aligned}
\Delta P_E(\rho, T) &= -b'(\rho)[f_T(T) - f_T(T_0)], \\
\Delta P_S(\rho, T) &= \frac{b'(\rho)}{m-1}[T(f_T'(T) - f_T'(T_{0S})) - T_0(f_T'(T) - f_T'(T_{0S}))] + \gamma_{0S}\rho c_{V,0S}(T - T_0).
\end{aligned} \tag{2.9}$$

In these two equations, $b'(\rho)$ is the derivative of thermal coefficients, which is given as

$$b(\rho) = \sum_n b_n \left(\frac{\rho_0}{\rho} - 1\right)^n, \tag{2.10}$$

where b_n are fitted polynomial parameters, and f_T measures the deviation from the reference temperature,

$$f_T = \left(\frac{T}{T_0}\right)^m - 1, \tag{2.11}$$

where m is a power law exponent with a theoretically expected value of 0.6 [Rosenfeld and Tarazona, 1998]. T_{0S}, $c_{V,0S}$ and γ_{0S} are the temperature, specific heat capacity at constant volume and Grüneisen parameter along the reference adiabat, whose expressions are given in Wolf and Bower [2018].

Model parameters, including ρ_0, K_0, K_0' and b_n, are fitted to molecular dynamic simulations of Spera et al. [2011] with data over a range of temperatures (∼2500 K-5000 K) and pressures (0-150 GPa). The resulting EoS accurately predicts densities of liquid $MgSiO_3$ from shock-wave experiments on $MgSiO_3$ glass [roughly in the range of 50-150 GPa and

3000-6000 K, Mosenfelder et al., 2009].

Thermophysical properties, such as specific heat capacity at constant volume and pressure per unit mass, c_V and c_P, and Grüneisen parameter, $\gamma = (\partial lnT/\partial lnV)_S$, are also directly output by the EoS, and expressions are provided in the Appendix of Wolf and Bower [2018]. The isothermal bulk modulus, K_T, and thermal expansion coefficient, α, are calculated using their definitions and quantities output by the EoS,

$$\begin{aligned} K_T &= -\rho \left.\frac{\partial P}{\partial \rho}\right|_T, \\ \alpha &= \frac{\gamma \rho c_V}{K_T}, \end{aligned} \tag{2.12}$$

where V is the volume at pressure, P, and temperature, T.

2.3.3 EoS for solid phase silicate and the iron-dominated core

Similar to the EoS of $MgSiO_3$ melt, the EoSs for enstatite, bridgmanite (Mg-perovskite), post-perovskite, liquid- and solid-phase iron, as well as Fe16Si (an Fe-Si alloy with 16wt% of Si) all consist of an isothermal component and a thermal perturbation. In this section, we provide a brief overview on the choices of EoSs.

In the mantle, the density at a given pressure level and a constant reference temperature, T_0 =300 K, for enstatite, bridgmanite and post-perovskite are calculated by the Vinet [Vinet et al., 1989], the third order Birch-Murnaghan (BM3) [Birch, 1952] and Keane's EoS [Stacey and Davis, 2008],

$$\begin{aligned} P_{\text{Vinet}}(\rho, T_0) &= 3K_0 \left[\left(\frac{\rho}{\rho_0}\right)^{\frac{2}{3}} - \left(\frac{\rho}{\rho_0}\right)^{\frac{1}{3}}\right] \exp\left\{\frac{3}{2}(K_0' - 1)\left[1 - \left(\frac{\rho}{\rho_0}\right)^{-\frac{1}{3}}\right]\right\} \\ P_{\text{BM3}}(\rho, T_0) &= \frac{3}{2}K_0 \left[\left(\frac{\rho}{\rho_0}\right)^{\frac{7}{3}} - \left(\frac{\rho}{\rho_0}\right)^{\frac{5}{3}}\right]\left[1 + \frac{3}{4}\left(K_0' - 4\right)\left(\left(\frac{\rho}{\rho_0}\right)^{\frac{3}{2}} - 1\right)\right] \\ P_{\text{Keane}}(\rho, T_0) &= K_0 \left\{\frac{K_0'}{K_\infty'^2}\left[\left(\frac{\rho}{\rho_0}\right)^{K_\infty'} - 1\right] - \left(\frac{K_0'}{K_\infty'} - 1\right) ln\left(\frac{\rho}{\rho_0}\right)\right\}, \end{aligned} \tag{2.13}$$

where T_0 is the reference temperature of 300 K, and ρ_0, K_0, K_0' and K_∞' are the density, isothermal bulk modulus, derivative of isothermal bulk modulus at the reference temperature and zero pressure, and derivative of isothermal bulk modulus in the limit of infinite pressure at the reference temperature. Fitted values for ρ_0, K_0, K_0' and K_∞' for the EoS of various phases of $MgSiO_3$ are summarized in table 2.1.

Material	EoS	$\rho_0(\mathrm{kg\,m^{-3}})$	K_0(GPa)	K_0'	K_∞'	T_0(K)	Ref.
Enstatite	Vinet	3215	105.8	8.5	N/A	300	a, b, c
Bridgmanite	BM3	4108	263	3.9	N/A	300	b, d
Post-perovskite	Keane	3977.6	197.7	4.82	2.56	300	e, f
Liquid Fe	Vinet	7037.8	83.7	5.97	N/A	1181	g
Solid Fe (ϵ)	Vinet	8267	163.4	5.38	N/A	300	h
Fe16Si	BM3	7179.4	206.5	4.0	N/A	300	i

Table 2.1: Fitted parameters for isothermal EoSs. References: (a) Aguichine et al. [2021]; (b) Sotin et al. [2007]; (c) Vacher et al. [1998]; (d) Hemley et al. [1992]; (e) Wagner et al. [2011]; (f) Oganov and Ono [2004]; (g) Dorogokupets et al. [2017]; (h) Dewaele et al. [2006]; (i) Fischer et al. [2012]

In the iron-dominated core, the isothermal component of the EoS of solid- and liquid-phase iron is calculated by the Vinet EoS with a reference temperature of 300 K and 1181 K respectively. The isothermal component of the EoS of all phases of Fe16Si is calculated by BM3 EoS with a reference temperature of 300 K. Fitted values for ρ_0, K_0, K_0' and K_∞' for the EoS of solid- and liquid-phase Fe and Fe16Si are summarized in table 2.1.

To incorporate the effect of temperature on density of enstatite, bridgmanite, post-perovskite, liquid Fe and Fe16Si, we add a Debye thermal pressure term, which accounts for the lattice vibrational energy with a cut-off frequency corresponding to the Debye frequency. The Debye thermal pressure is given as:

$$P_{De}(\rho, T) = \gamma \rho E_{in}(\rho, T), \tag{2.14}$$

where γ is the Grüneisen parameter, and E_{in} is the internal energy per unit mass. E_{in} is

calculated based on the Debye model:

$$E_{in} = 9nR_gT\left(\frac{T}{\theta}\right)^3 \int_0^{\frac{\theta}{T}} \frac{t^3}{e^t - 1} dt, \tag{2.15}$$

where n is the atomic molar density in (mol kg^{-1}), R_g is the molar gas constant,and θ is the Debye temperature. The complete equation of state is then:

$$P\left(\rho, T\right) = P\left(\rho, T_0\right) + \left[P_{De}\left(\rho, T\right) - P_{De}\left(\rho, T_0\right)\right]. \tag{2.16}$$

In addition to the effect of Debye thermal pressure, the density of solid iron is subject to an additional effect of anharmonic and electronic thermal pressures. The complete EoS for solid iron is

$$\begin{aligned} P(\rho, T) =& P\left(\rho, T_0\right) + \left[P_{De}\left(\rho, T\right) - P_{De}\left(\rho, T_0\right)\right] \\ &+ \left[P_{an}(\rho, T) - P_{an}(\rho, T_0)\right] + \left[P_{el}(\rho, T) - P_{el}(\rho, T_0)\right], \end{aligned} \tag{2.17}$$

where P_{an} and P_{el} are anharmonic and electronic thermal pressures, and given as:

$$\begin{aligned} P_{an} &= \frac{3}{2} R_g \rho m a_0 \left(\frac{\rho}{\rho_0}\right)^{-m} T^2 \\ P_{el} &= \frac{3}{2} R_g \rho g e_0 \left(\frac{\rho}{\rho_0}\right)^{-g} T^2. \end{aligned} \tag{2.18}$$

Parameters a_0, m, e_0 and g are given by Dewaele et al. [2006]: $a_0 = 3.7 \times 10^{-5}$ K^{-1}, m=1.87, $e_0 = 1.95 \times 10^{-4}$ K^{-1} and g=1.339.

The Grüneisen parameter, γ, and the Debye temperature, θ, vary with density. For enstatite and bridgmanite, these values are calculated as

Material	γ_0	γ_∞	θ_0 (K)	λ	n	Ref.
Enstatite	1.009	0	710	1	49.8058	a, b, c
Bridgmanite	1.96	0	1017	2.5	49.8058	b, d
Post-perovskite	1.553	1.114	1100	4.731	49.8058	e, f
Liquid Fe	2.033	0	263	1.168	17.907	g
Solid Fe (ϵ)	1.875	1.305	417	3.289	17.907	h
Fe16Si	1.8	0	417	1	20.7415	i

Table 2.2: Parameters used for the thermal correction according to Mie–Grüneisen–Debye. References: (a) Aguichine et al. [2021]; (b) Sotin et al. [2007]; (c) Vacher et al. [1998]; (d) Hemley et al. [1992]; (e) Wagner et al. [2011]; (f) Oganov and Ono [2004]; (g) Dorogokupets et al. [2017]; (h) Dewaele et al. [2006]; (i) Fischer et al. [2012]

$$\begin{aligned} \gamma &= \gamma_0 \left(\frac{\rho}{\rho_0}\right)^{-\lambda}, \\ \theta &= \theta_0 \left(\frac{\rho}{\rho_0}\right)^{\gamma}. \end{aligned} \tag{2.19}$$

For post-perovskite, Fe16Si, and solid- and liquid-phase iron, these values are given in the Al'Tshuler form [Al'Tshuler et al., 1987],

$$\begin{aligned} \gamma &= \gamma_\infty + (\gamma_0 - \gamma_\infty) \left(\frac{\rho}{\rho_0}\right)^{-\lambda}, \\ \theta &= \theta_0 \left(\frac{\rho}{\rho_0}\right)^{\gamma_\infty} \exp\left[\frac{\left(1 - (\rho/\rho_0)^{-\lambda}\right)(\gamma_0 - \gamma_\infty)}{\lambda}\right], \end{aligned} \tag{2.20}$$

where subscript 0 denotes values evaluated at reference state and ∞ at infinite large pressure. Parameters relevant to the thermal correction are summarized in table 2.2.

The specific heat capacity at constant pressure per unit mass, c_P, is approximately constant for mantle silicate within the pressure range ($\lesssim$ 1000 GPa) in the mantle of the studied planets in this thesis [Stamenković et al., 2011]. The thermal conductivities of both mantle silicate and iron have been shown to increase with growing pressure [Stamenković et al., 2011]. In this work, we assume average Earth mantle and core values, which are summarized in table 2.3. We offer a discussion on how different thermal conductivities for

mantle silicate and iron could affect the lifetime of the dynamo in the liquid core in Chapter 4. The isothermal bulk modulus, K_T, and the thermal expansion coefficient, α, are calculated using the expression in eqn 2.12, where c_V is

$$c_V = \frac{c_P}{1 + \gamma \alpha T}. \tag{2.21}$$

Material	k($\mathrm{Wm^{-1}K^{-1}}$)	c_P ($\mathrm{JK^{-1}kg^{-1}}$)	Ref.
Enstatite	4	1250	1
Bridgmanite	10	1260	1
Post-perovskite	10	1260	1
Molten silicate	4	N/A	2
Fe	$40^{(3)}$	$840^{(1)}$	1, 3

Table 2.3: Parameters used for the thermal correction according to Mie–Grüneisen–Debye. References: (1) Yukutake [2000]; (2) Bower et al. [2018]; (3) Konôpková et al. [2016]

2.4 Core cooling

The temperature distribution in the liquid iron core is assumed to be adiabatic, and the adiabatic temperature gradient is given as

$$\left(\frac{\partial T}{\partial P}\right)_S = \frac{\alpha T}{\rho c_P}, \tag{2.22}$$

where α and c_P denote the thermal expansion coefficient and specific heat per unit mass at constant pressure. The inner core starts solidifying once the adiabat of the liquid iron core intersects with the melting curve of iron. We assume the solid inner core to be conductive and solve the heat conduction equation to calculate its cooling process,

$$\rho c_P \frac{\partial T}{\partial t} = \frac{1}{r^2}\frac{\partial}{\partial r}\left(r^2 k_c \frac{\partial T}{\partial r}\right) + \alpha T \frac{\partial P}{\partial t}, \tag{2.23}$$

where k_c is the thermal conductivity of iron. The second term on the right side of the equation is rate of heating due to adiabatic compression. Pressure changes in the planet are calculated using the Henyey solver.

The cooling process of the liquid core is described by its energy balance equation,

$$\int_{M_{ic}}^{M_c} c_P \dot{T} dm - \int_{M_{ic}}^{M_c} \frac{\alpha T}{\rho} \dot{P} dm = 4\pi R_c^2 k_{LM} \left.\frac{\partial T}{\partial r}\right|_{\mathrm{CMB}} - 4\pi R_{\mathrm{ICB}}^2 k_c \left.\frac{\partial T}{\partial r}\right|_{\mathrm{ICB}} + L_{\mathrm{Fe}} \dot{M}_{ic}, \tag{2.24}$$

where M_{ic} and M_c are masses of the solid inner core and the entire iron core, R_{ICB} and R_c are radii of the solid inner core and the entire core, k_{LM} and k_c are the thermal conductivity of the lower mantle at CMB and iron at the inner core boundary (ICB), and $(\partial T/\partial r)_{\mathrm{CMB}}$ and $(\partial T/\partial r)_{\mathrm{ICB}}$ are temperature gradients at the base of the mantle and the base of the liquid core. The left hand side of the equation is the internal energy change rate of the iron core. The first and second terms on the right hand side of equation 2.24 are the heat loss rate by conduction across the CMB and rate of heat gain across the ICB by conduction. The third term is the latent heat release rate due to inner core solidification.

The thermal history of the liquid core can be described by a potential temperature, T_{Pot}, which is the temperature of the liquid iron core if it were adiabatically decompressed to a fixed pressure reference point, P_{Pot} [Unterborn and Panero, 2019]. For each planet we choose an arbitrary reference point at a pressure level ~ 5 GPa lower than P_{CMB} at the beginning of the evolution. For example, the P_{Pot} for the planet with $1 M_\oplus$ and CMF=0.326 is 120 GPa. The first term on the left side of equation 2.24 is related to T_{Pot} by the following equation

$$\int_{M_{ic}}^{M_c} c_P \dot{T} dm = \int_{M_{ic}}^{M_c} c_P \left.\frac{\partial T}{\partial T_{Pot}}\right|_P \dot{T}_{Pot} dm + \int_{M_{ic}}^{M_c} c_P \left.\frac{\partial T}{\partial P}\right|_{T_{Pot}} \dot{P} dm. \tag{2.25}$$

T_{Pot} is a proxy for entropy, and $(\partial T/\partial P)_{T_{Pot}}$ is the adiabatic temperature gradient, given

by equation 2.22. The second term on the right side of equation 2.25 becomes

$$\int_{M_{ic}}^{M_c} c_P \left.\frac{\partial T}{\partial P}\right|_{T_{Pot}} \dot{P} dm = \int_{M_{ic}}^{M_c} \frac{\alpha T}{\rho} \dot{P} dm. \tag{2.26}$$

We can rewrite equation 2.24 in terms of T_{Pot} using equations 2.25 and 2.26, and the adiabatic compression term (the second term) on the left side of equation 2.24 is cancelled by equation 2.26:

$$\dot{T}_{Pot} \int_{M_{ic}}^{M_c} c_P \left.\frac{\partial T}{\partial T_{Pot}}\right|_P dm = 4\pi R_c^2 k_{LM} \left.\frac{\partial T}{\partial r}\right|_{\text{CMB}} - 4\pi R_{\text{ICB}}^2 k_c \left.\frac{\partial T}{\partial r}\right|_{\text{ICB}} + L_{\text{Fe}} \dot{M}_{ic}. \tag{2.27}$$

This is because heating due to adiabatic compression is accounted for when parameterizing the P-T profile by T_{Pot}.

$\dot{T}_{Pot}$ is expressed in terms of the change in conditions at the CMB by:

$$\dot{T}_{Pot} = \left.\frac{\partial T_{Pot}}{\partial T_{\text{CMB}}}\right|_{P_{\text{CMB}}} \dot{T}_{\text{CMB}} + \left.\frac{\partial T_{Pot}}{\partial P_{\text{CMB}}}\right|_{T_{\text{CMB}}} \dot{P}_{\text{CMB}}. \tag{2.28}$$

The partial derivatives with respect to T_{Pot}, T_{CMB} and P_{CMB} in equations 2.25 and 2.28 are calculated numerically using the pre-calculated table of core adiabats.

The inner core nucleation decelerates the cooling rate of the core by releasing latent heat. Given a potential temperature, we can determine M_{ic}, and the pressure and radius at the boundary of inner and outer cores, P_{ICB} and R_{ICB}, by the intersection of the core adiabat and the melting curve (equation 2.6). Consequently, we can express $\dot{M}_{ic}$ as

$$\dot{M}_{ic} = \begin{cases} 0 & P_{\text{ICB}} > P_{\text{center}} \text{ or } P_{\text{ICB}} < P_{\text{CMB}} \\ \frac{dM_{ic}}{dP_{\text{ICB}}} \frac{dP_{\text{ICB}}}{dT_{Pot}} \dot{T}_{Pot} & P_{\text{CMB}} < P_{\text{ICB}} < P_{\text{center}}. \end{cases} \tag{2.29}$$

dP_{ICB}/dT_{Pot} is evaluated numerically and dM_{ic}/dP_{ICB} is obtained from equation 2.2,

$$\frac{dM_{ic}}{dP_{\rm ICB}} = -\frac{4\pi R_{\rm ICB}^4}{GM_{ic}}. \tag{2.30}$$

Combining equations 2.24 to 2.29, we obtain the energy balance equation of the core as a function of a single temperature, $T_{\rm CMB}$.

2.5 Mantle heat transport

The basic equation for calculating the energy transport in the mantle is provided by Sasaki and Nakazawa [1986a]. Here, we express the energy transport equation in terms of entropy instead of temperature,

$$\rho T \frac{\partial s}{\partial t} = -\frac{1}{r^2}\frac{\partial}{\partial r}\left(r^2 F\right) + \rho H, \tag{2.31}$$

where s is specific entropy per unit mass, H is energy generation rate per unit mass, and F is the sum of conductive and convective flux. We write equation 2.31 in terms of entropy because it is a natural coordinate for convecting systems of both pure solid/liquid and partially molten aggregates.

Thermal conduction is given by Fourier's law, which is split into an adiabatic and a super/sub-adiabatic part [Bower et al., 2018],

$$F_{cond} = -\rho c_P \kappa \left.\frac{\partial T}{\partial r}\right|_s - \rho T \kappa \frac{\partial s}{\partial r}, \tag{2.32}$$

where κ is the thermal diffusivity, and $\left(\partial T/\partial r\right)_s$ is the adiabatic temperature gradient, given by $\left(\partial T/\partial r\right)_s = \rho g \left(\partial T/\partial P\right)_s$.

Thermal convection occurs when the entropy gradient, $\partial s/\partial r$, is negative. We use the modified mixing length theory [Sasaki and Nakazawa, 1986a, Abe, 1995, Senshu et al., 2002] to evaluate the convective heat flow, which considers the energy transport by the vertical motion by fluid parcels. This method allows us to use local values of physical quantities to

evaluate heat transport within each zone. $F_{\rm conv}$, the convective heat flux, is given as

$$F_{\rm conv} = -\rho T \kappa_h \frac{\partial s}{\partial r}, \tag{2.33}$$

where κ_h is eddy diffusivity.

In a fully solid/liquid case, convection is driven by the temperature gradient, and κ_h is

$$\kappa_h = \begin{cases} \sqrt{-\dfrac{\alpha g T l^4}{16 c_P} \dfrac{\partial s}{\partial r}} & \text{for } -\dfrac{\alpha g T l^4}{18 c_P \nu^2} \dfrac{\partial s}{\partial r} \geq \dfrac{9}{8} \quad (2.34a) \\ -\dfrac{\alpha g T l^4}{18 c_P \nu} \dfrac{\partial s}{\partial r} & \text{for } 0 < -\dfrac{\alpha g T l^4}{18 c_P \nu^2} \dfrac{\partial s}{\partial r} < \dfrac{9}{8}, \quad (2.34b) \end{cases}$$

where g gravitational acceleration, l mixing length, and ν kinematic viscosity. The eddy diffusivity for inviscid fluid (equation 2.34a) is derived in Vitense [1953] and for viscous fluid (equation 2.34b) is adapted from Sasaki and Nakazawa [1986a]. Both equations in the original papers are expressed in terms of the temperature gradient, and the ones in terms of the entropy gradient are provided in [Bower et al., 2018]. A detailed derivation is given in Appendix 2.A. The transition between the inviscid and viscous regimes is determined by the velocity of fluid parcels. In equation 2.34a, the velocity is estimated based on the exchange between the kinetic and gravitational potential energy of parcels; in equation 2.34b, the velocity is estimated by the Stokes velocity, which considers the force balance between buoyancy force and viscous drag force exerted on fluid parcels.

In the case of a solid and liquid mixture, ρ is determined from the densities of pure solid, ρ_s, and pure liquid, ρ_m, at $T_{si,m}$ at a specified pressure by the additive volume mixing rule. The temperature profile is fixed on the melting curve of mantle silicate for the idealized cases of a single pure compound, and convection is then driven by the melt fraction gradient rather than the temperature gradient. We derived κ_h in such a case (see Appendix 2.B for details),

$$\kappa_h = \begin{cases} \sqrt{-\dfrac{\alpha_x g T_{si,m} l^4}{16L}\dfrac{\partial s}{\partial r}} & \text{for } -\dfrac{\alpha_x g T_{si,m} l^4}{18L\nu^2}\dfrac{\partial s}{\partial r} \geq \dfrac{9}{8} \quad (2.35a) \\ -\dfrac{\alpha_x g T_{si,m} l^4}{18L\nu}\dfrac{\partial s}{\partial r} & \text{for } 0 < -\dfrac{\alpha_x g T_{si,m} l^4}{18L\nu^2}\dfrac{\partial s}{\partial r} < \dfrac{9}{8}, \quad (2.35b) \end{cases}$$

where α_x is the expansion coefficient due to changes in melt fraction, and defined as

$$\alpha_x \equiv -\frac{1}{\rho}\left.\frac{\partial \rho}{\partial x}\right|_P = \rho\left(\frac{1}{\rho_m} - \frac{1}{\rho_s}\right). \quad (2.36)$$

The melt fraction x is related to the entropy by

$$x(s,P) = \begin{cases} 0 & \text{for } s \leq s_s(P) \quad (2.37a) \\ \dfrac{s - s_s(P)}{s_m(P) - s_s(P)} & \text{for } s_s(P) < s < s_m(P) \quad (2.37b) \\ 1 & \text{for } s \geq s_m(P), \quad (2.37c) \end{cases}$$

where s_m and s_s are the specific entropies of pure liquid and pure solid at $T_{si,m}(P)$. Similarly to the single phase case, the transition between formula 2.35a and 2.35b is determined by the velocity of the convecting parcels.

To improve the numerical stability of the code, we employ a transition function, $z(y)$, to ensure that κ_h varies smoothly and continuously when the mantle silicate goes through phase transitions from pure liquid phase to a liquid and solid mixture, and from the mixture to pure solid phase. κ_h is then

$$\kappa_h = \begin{cases} z(y_m)\kappa_{h,2.34a} + (1 - z(y_m))\kappa_{h,2.35a} & \text{for inviscid fluid} \quad (2.38a) \\ (1 - z(y_s))\kappa_{h,2.34b} + z(y_s)\kappa_{h,2.35b} & \text{for viscous fluid ,} \quad (2.38b) \end{cases}$$

where $\kappa_{h,2.34a}$,$\kappa_{h,2.34b}$,$\kappa_{h,2.35a}$ and $\kappa_{h,2.35b}$ are given by corresponding formula for κ_h. The transition function, $z(y)$, approaches 0 as $y \to -\infty$, and 1 as $y \to \infty$, and is given as,

$$z(y) = \frac{1}{2} + \frac{1}{2}\tanh(y), \tag{2.39}$$

where y is

$$\begin{aligned} y_m &= \frac{s - s_m}{s_w} \qquad \text{for inviscid fluid} \\ y_s &= \frac{s - s_s}{s_w} \qquad \text{for viscous fluid.} \end{aligned} \tag{2.40}$$

with s_w being the transition width. We choose s_w to be $s_w = 0.02 \times (s_m - s_s)$, which corresponds to 0.02 in melt fraction. y_m and y_s appear in equations 2.38a and 2.38b separately because the transition from fully liquid to the 2-phase mixture happens in the inviscid regime while the transition from the 2-phase mixture to fully solid happens in the viscid regime.

The mixing length, l, describes the characteristic length that a fluid parcel can travel due to the thermal buoyancy force before it merges with the surroundings. Abe [1995] set l to be the distance from the nearest boundary of convection (D). Several groups [e.g. Tachinami et al., 2011, Wagner et al., 2019] calibrated the 1-D mixing length theory against boundary layer theory and 3-D convection models for rocky planets, and came up with different prescriptions for l. Tachinami et al. [2011] compared the evolution result of the Earth using mixing length theory to calculations using the boundary layer theory and found $l = 0.82D$ to be the best choice, which we use for all simulations in this study. Such a prescription results in a small mixing length and thus a low convective heat flow near convection boundaries, and heat transport is dominated by thermal conduction. Calculations with other prescriptions for l are left for future investigation.

In this thesis, we consider whole mantle convection where the only convection boundaries are the planet surface and the CMB. However, the mixing length formulation employed in our model can be easily applied to mantle convection with additional barriers, as Tachinami et al. [2011] pointed out. Several groups suggest that phase boundaries in the mantle may serve as barriers to mantle convection, such as the solid/melt boundary [Labrosse et al.,

2007] or the upper/lower mantle phase boundary [Honda et al., 1993].

To save computation time while solving equation 2.31, we pre-tabulate thermophysical quantities, including T, ρ, α, and $c_{P,m}$ (specific heat of silicate per unit mass in liquid phase), as a function of s and P using the EoSs described in section 2.3. Values of these quantities are obtained using a 2D interpolation routine (RectBivariateSpline) in SciPy during each thermal timestep in the evolution calculation.

Viscosity, η, and radiogenic heating, H, are two other important components of mantle dynamics, which we discuss in sections 2.6 and 2.7.

2.6 Viscosity of mantle silicate

The dynamic viscosity of mantle silicate, $\eta = \nu\rho$, is one of the most important quantities in the thermal evolution calculation of rocky planets, especially during the later stage when the entire mantle has solidified. The level of viscosity determines the cooling rate of the mantle, which then controls how fast the iron-dominated core can cool. For silicate in the liquid phase, we take $\eta_m = 100$Pa s [Abe, 1997]. For enstatite and bridgmanite, we follow Tachinami et al. [2011], Zhang and Rogers [2022] and adopt we adopt an Arrhenius formulation for temperature- and pressure-dependent viscosity [Ranalli, 2001],

$$\eta_s = \frac{1}{2}\left[\frac{1}{B^{1/n_c}}\exp\left(\frac{E^* + PV^*}{nR_gT}\right)\right]\dot{\epsilon}^{(1-n_c)/n_c}, \tag{2.41}$$

where B, R_g, n_c, E^*, V^* and $\dot{\epsilon}$ are the Barger coefficient, molar gas constant, creep index, activation energy, activation volume and strain rate, respectively. Values of these parameters for enstatite and bridgmanite are listed in table 2.4.

Ammann et al. [2010] and Tackley et al. [2013] applied the density function theory calculations to explore the viscosity of post-perovskite. They found that the diffusion rates of Mg^{2+} and Si^{4+} in post-perovskite is anisotropic, depending on the lattice orientation. The

Material	B($\mathrm{Pa^{-n_c}s^{-1}}$)	n_c	E*(10^3J mol^{-1})	V*(10^{-6}m^{2}mol^{-1})	$\dot{\epsilon}$($\mathrm{s^{-1}}$)
Enstatite	3.5×10^{-15}	3.0	430	10	10^{-15}
Bridgmanite	7.4×10^{-17}	3.5	500	10	10^{-15}

Table 2.4: Parameters of viscosity for enstatite and bridgmanite [Ranalli, 2001]

fastest and the slowest diffusion rates of magnesium and silicon result in the lower-bound and upper-bound rheology for post-perovskite. The viscosity of post-perovskite with two rheologies is given as

$$\eta(T,p) = \eta_0 \exp\left[\frac{H(p)}{RT} - \frac{H(0)}{RT_0}\right], \tag{2.42}$$

where η_0 is the reference viscosity obtained at zero pressure and reference temperature $T_0 = 1600$ K, and $H(p)$ is the migration enthalpy. $H(p)$ is calculated based on the following equation,

$$H(p) = E^* + pV^* \exp\left(-p/p_{\mathrm{decay}}\right). \tag{2.43}$$

Parameters in equations 2.42 and 2.43 are summarized in table 2.5.

Rheology	E*(10^3J mol^{-1})	V*(10^{-6}m^{2}mol^{-1})	p_{decay} (GPa)	η_0(Pa · s)
Lower-bound	162	1.4	1610	1.9×10^{21}
Upper-bound	780	1.7	1100	1.05×10^{34}

Table 2.5: Parameters of viscosity for post-perovskite [Tackley et al., 2013]

As Ammann et al. [2010] argues, the lower-bound rheology might be relevant to the weak D" layer in the lowermost mantle of Earth. We therefore choose the lower-bound rheology as the fiducial choice in the calculation of the viscosity of post-perovskite. We also perform calculations with the upper-bound rheology for post-perovskite to explore the effect of viscosity of the thermal and magnetic history of rocky super-Earths.

The viscosity of partially molten material should capture an abrupt change at the critical melt fraction $x_{crit} = 0.4$ as the molten aggregate shifts between liquid-like and solid-like. We adopt a similar formulation to Bower et al. [2018], and model η as

$$log_{10}\eta = z log_{10}\eta_m + (1-z) log_{10}\eta_s, \tag{2.44}$$

where η_m and η_s are dynamic viscosity for liquid and solid phase silicate. z is the same transition function as equation 2.39 with y defined as $y = (x - x_{crit})/0.15$.

In addition to the above formulation for viscosity, our code can readily take a wide range of other viscosity parameterizations, including those adopted by Abe [1995], Stamenković et al. [2012], and Driscoll and Bercovici [2014]. In this thesis, we consider a single choice to demonstrate the workings of code and to explore the influence of a temperature- and pressure-dependent viscosity on the planet evolution.

2.7 Internal heat production

Internal heat production, H, is important for rocky planet evolution on geological timescales. For Earth, the heat production is generated by the decay of ^{40}K, ^{232}Th, ^{235}U and ^{238}U. The estimated amount of these elements in Earth's mantle and their half life time are compiled in table 2.6. The total mantle radiogenic heat production is the sum over 4 isotopes,

$$H = \sum_i q_{0,i} \exp\left(\ln 2 \left(t_\oplus - t\right)/\tau_i\right), \tag{2.45}$$

where $t_\oplus$ is the current age of Earth, $q_{0,i}$ is the current radiogenic heat production rate per unit mass in Earth's mantle and τ_i is the radioactive decay time of four major isotopes. Previous works have studied the effect of different concentrations of radionuclides [e.g. Nimmo et al., 2020]. However, for this study, we assume the same abundance of radioactive elements in the mantle as those in Earth's mantle and model the elements as uniformly distributed with mass in the mantle through convection.

Element	$q_0(\mathrm{W\,kg^{-1}})$	$\tau(\mathrm{Gyr})$
^{40}K	8.69×10^{-13}	1.25
^{232}Th	2.24×10^{-12}	14
^{235}U	8.48×10^{-14}	0.704
^{238}U	1.97×10^{-12}	4.47

Table 2.6: Parameters of radiogenic elements [McDonough and Sun, 1995]

2.8 Initial conditions

We assume the initial temperature profile to be adiabatic in both the iron-dominated core and the silicate mantle. We integrate the adiabatic temperature gradient from the planet center to the surface with a surface pressure of 1 bar and initial central temperature, T_c, which is tied to the initial thermal energy of the planet. The adiabatic temperature gradient is

$$\left(\frac{\partial T}{\partial P}\right)_S = \frac{\alpha T}{\rho c_P}. \tag{2.46}$$

The initial thermal energy of the planet is determined by its gravitational potential energy. During the formation of the planet, the gravitational potential energy released by the accretion of cold planetestimals and embryos partially converts to thermal energy heating the planet. A significant fraction of the thermal energy is lost to radiation during the formation process and only a fraction h is retained by the planet in the form of thermal energy. Since we do not model the planet formation, we choose $h \sim 0.15$ as the default value. The effect of the choice of h —or more generally the initial post-formation temperature profile— on the predicted dynamo lifetime in the liquid core will be explored in the future.

The initial thermal energy of the planet is

$$E_0 = h\int_0^{R_{\rm pl}} \frac{[4\pi r^2\rho(r)][\frac{4}{3}\pi r^3\rho(r)]}{r}dr = \int_0^{M_{\rm pl}} c_{\rm P}\Delta T dm, \tag{2.47}$$

where M_{pl} and R_{pl} are planetary mass and radius, G is the gravitational constant and ΔT

is the temperature rise from surroundings ($\sim$ 255 K for Earth-level stellar irradiation) to the initial local temperature in individual cells in the planet. We iterate the integration of equation 2.46 to search for an appropriate T_c that corresponds to an h of 0.15 in equation 2.47 within a relative tolerance of 10^{-4}.

2.9 Boundary conditions

In this study, we explore a simplified scenario where planets cool down through radiation at the planet surface. The surface heat flow is thus chosen as a gray-body radiation,

$$F_{\text{surf}} = -k_{\text{UM}} \left.\frac{\partial T}{\partial r}\right|_{\text{surf}} = \sigma \left(T_{\text{surf}}^4 - T_{eq}^4\right), \tag{2.48}$$

where F_{surf} is the net outgoing surface heat flux, k_{UM} is the thermal conductivity of the upper mantle, σ the Stefan-Boltzmann constant, T_{surf} surface temperature and T_{eq} the equilibrium temperature, which corresponds to the radiation from the host star.

Our model does not explicitly differentiate between stagnant-lid and mobile-lid convection and impose the thickness of conductive thermal boundary layers. Instead, a boundary layer where thermal conduction dominates is automatically captured by the mixing length, l. When approaching a convection barrier (the surface or CMB), κ_h decreases rapidly in proportion to l^4. Our choice of the mixing length, as described in section 2.5, represents an Earth-like scenario with mobile-lid convection. Wagner et al. [2019] calibrated the mixing length theory against a 3-D mantle convection simulation. They presented various parametrizations of the mixing length for stagnant-lid, sluggish-lid, and mobile-lid convection, which we plan to explore using our model in future studies.

The surface temperature and pressure is typically determined by the atmosphere for a real planet. Abe [1997] discussed the thermal blanketing effect of a steam or H_2/He atmosphere, which may sustain a shallow surface magma ocean. Elkins-Tanton [2008] explored Earth's

and Mars' atmosphere growth due to magma ocean solidification, and found that the final atmospheric pressure could reach several thousand bar. However, exploring the influence of an atmosphere on the thermal evolution of rocky planets is beyond the scope of this thesis. Additionally, Bower et al. [2019] points out that the silicate mantle may not experience an appreciable amount of compression due to an outgassed atmosphere, as the bulk modulus of molten and solid silicate is around 100 GPa. In this thesis, the surface temperature is determined by solving the energy transport equation (equation 2.31) at the planet surface and the surface pressure is set to be 1 bar. At the bottom surface of the mantle, namely the CMB, the heat flux is evaluated based on heat conduction through the CMB layer, the first term on the right hand side of equation 2.24,

$$F_{\mathrm{CMB}} = -k_{\mathrm{LM}} \left.\frac{\partial T}{\partial r}\right|_{\mathrm{CMB}}, \tag{2.49}$$

where k_{LM} is the thermal conductivity of lower mantle.

The partial derivatives in equations 2.48 and 2.49 indicate the slopes of the radial temperature profile in the upper and lower thermal boundary layers in the mantle. Together with the thermal conductivities in the thermal boundary layers, the partial derivatives determine how much heat can be conducted into and out of the mantle. For the major portion of the planet evolution, we use the finite-difference method and the temperatures at the faces of the bottom and the top cells to approximate the partial derivatives. During the magma ocean stage, however, the thickness of the conductive boundary at the planet surface and the core mantle boundary (CMB) is ultra-thin due to the low viscosity of molten silicate, on the order of a few centimeters to a few meters. The thickness of the boundary layers is below the spatial resolution in the code (a few kilometers). To eliminate artifacts due to spatial resolution in individual layers, we calculate the thickness of the conductive boundary layers using local conditions at the planet surface and the CMB during the magma ocean stage. We briefly describe the calculation in the rest of this section.

In the thermal boundary layers, the Rayleigh number, $\mathrm{Ra_{BL}}$ is calculated as

$$\mathrm{Ra_{BL}} = \frac{\rho^2 c_P \alpha g \Delta T_{\mathrm{BL}} \delta_{\mathrm{BL}}^3}{k\eta}, \tag{2.50}$$

where δ_{BL} is the thickness of the boundary layer, and ΔT_{BL} is the temperature jump across the thermal boundary layers. Setting $\mathrm{Ra_{BL}} = \mathrm{Ra_c}$, we can calculate the thickness of the conductive thermal boundary layers,

$$\delta_{\mathrm{BL}} = \left(\frac{\mathrm{Ra_c} k\eta}{\rho^2 c_P \alpha g \Delta T_{\mathrm{BL}}} \right)^{1/3}. \tag{2.51}$$

Thermophysical properties, including ρ, α, g and η, are evaluated based on the temperature and the pressure at the center of the thermal boundary layers at the preview timestep. ΔT_{BL} is $T_{\mathrm{CMB}} - T_{\mathrm{LM}}$ and $T_{\mathrm{UM}} - T_{\mathrm{surf}}$ for the lower and the upper thermal boundary layers, with T_{LM} and T_{UM} being the temperature at the top and the base of the lower and the upper thermal boundary layers.When δ_{BL} is smaller than the spatial resolution at the planet surface and/or the CMB, the top and/or the bottom cells in the mantle are split into two sub-cells, with one sub-cell being the conductive boundary layer and the other one merged into the convection zone below/above.

2.10 Criterion to drive a dynamo in rocky planets

A dynamo action within the planet requires a magnetic Reynolds number that exceeds a critical value,

$$Re_m = \mu_0 v L_c \sigma > Re_{m,crit}, \tag{2.52}$$

where μ_0 is the magnetic permeability in vacuum, v is the flow velocity, L_c is the thickness of the magma ocean/liquid iron core, and σ is the electrical conductivity of the convective fluid. As Christensen and Aubert [2006] suggest, a self-sustained dynamo action requires a

critical value, $Re_{m,crit}$, of order 50, which we adopt for both the iron core and the magma ocean in our model. We note, however, that the study in Christensen and Aubert [2006] is configured to represent modern Earth's core and we advocate for dynamo studies focusing on the magma ocean.

Several groups have attempted to measure the electrical conductivity of molten silicate using dynamic and *ab initio* calculations [Soubiran and Militzer, 2018, Stixrude et al., 2020]. They have shown that molten silicate is semi-metallic and estimated its electrical conductivity to be of the order of 10^4 $\mathrm{S\,m^{-1}}$. Given the level of electrical conductivity and using an illustrative value for the thickness of the convective layer, $\sim 10^6$ m, a minimal flow velocity of the order of $1\mathrm{mm\,s^{-1}}$ is required so that Re_m can exceed the critical value in a magma ocean.

We evaluate Re_m in each cell to determine whether and where a dynamo action can occur in the magma ocean. The flow velocity is estimated with the modified mixing length theory, $v \sim \kappa_h/l$. We use the equation provided in Stixrude et al. [2020] to calculate the electrical conductivity of molten silicate, which includes ionic and spin-polarized electric contributions,

$$\sigma = \sigma_0 T^{-1} \exp\left(-\frac{E_\sigma + PV_\sigma}{R_g T}\right). \tag{2.53}$$

Values of σ_0, E_σ, and V_σ for ionic and spin-polarized electric contributions are summarized in table 2.7. The electrical conductivity of partial melts is weighted by the melt fraction.

Contribution	$\sigma_0(\mathrm{Sm^{-1}})$	$\mathrm{E^*}(10^3\ \mathrm{J\,mol^{-1}})$	$V^*(10^{-6}\ \mathrm{m^2\,mol^{-1}})$
Spin-polarized electronic contribution	1.754×10^9	108.6	0.0611
Ionic contribution	1.0811×10^9	131	0.437

Table 2.7: Parameters for electrical conductivity of molten silicate [Stixrude et al., 2020]

We compute Re_m for the entire liquid iron core to determine whether the dynamo can operate within the liquid core and its lifetime. To translate the core convective flux to the

flow velocity, we employ a mixing length scaling law [Christensen, 2010],

$$v = \left(\frac{L_{\rm c} F_{\rm c}}{\rho H_T} \right)^{1/3}, \tag{2.54}$$

where $H_T = c_P/(\alpha g)$ is the temperature scale height, $F_{\rm c}$ is the effective core convective flux and L_c is the thickness of the convecting liquid core. In the case where the core dynamo is solely driven by thermal convection, $F_{\rm c}$ is the same as the core convective heat flux, $F_{\rm conv}$, which is calculated as the difference between the total heat flux coming out of the core ($F_{\rm CMB}$) and the conductive heat flux along the core adiabat ($F_{\rm cond}$), given as

$$F_{\rm cond} = k_c \left(\frac{\alpha g T}{c_P} \right)_{\rm s,CMB}. \tag{2.55}$$

The liquid iron core is no longer convecting if $F_{\rm CMB} < F_{\rm cond}$, and $F_{\rm conv}$ is taken to be 0. In the case where the core dynamo is driven by both thermal and composition convection, $F_{\rm c}$ is obtained from the sum of thermal and chemical buoyancy flux [Christensen et al., 2009]. The thermal and chemical buoyancy flux, $F_{\rm th}$ and F_χ, are given by [Driscoll and Bercovici, 2014],

$$F_{\rm th} = \frac{\alpha_{\rm c} g_{\rm c}}{\rho_{\rm c} c_{\rm P,c}} F_{\rm conv} \tag{2.56}$$

$$F_\chi = g_{\rm ic} \frac{\Delta\rho_\chi}{\rho_{\rm ic}} \left(\frac{R_{\rm ic}}{R_{\rm c}} \right)^2 \frac{dR_{\rm ic}}{dt}, \tag{2.57}$$

where subscripts c and ic refers to values taken at the CMB and the ICB, and $\Delta\rho_\chi$ is the density contrast between the inner and the outer core at the ICB. We can then translate F_χ to an equivalent thermal flux by $(\rho_{\rm c} c_{\rm P,c})/(\alpha_{\rm c} g_{\rm c}) F_\chi$. The effective core convective flux, F_c, in this case is

$$F_c = F_{\rm conv} + \frac{c_{\rm P,c}}{\alpha_{\rm c}} \Delta\rho_\chi \left(\frac{R_{\rm ic}}{R_{\rm c}} \right)^2 \frac{dR_{\rm ic}}{dt}. \tag{2.58}$$

The convection in the liquid core is shut off if F_c reaches 0.

We use the Wiedemann-Franz law to calculate the electrical conductivity of liquid iron,

$$\sigma = \frac{k_c}{L_0 T}, \tag{2.59}$$

where k_c is the thermal conductivity of liquid iron and L_0 is the Lorenz number. We use 80 $\mathrm{Wm^{-1}K^{-1}}$ as the default value for k_c . However, a range of k_c under the core conditions (18 to 150$\mathrm{Wm^{-1}K^{-1}}$) have been reported [e.g. Monteux et al., 2011, Pozzo et al., 2012, 2014, Konôpková et al., 2016, Ohta et al., 2016, Zhang et al., 2020, 2022, Pourovskii et al., 2020, Inoue et al., 2020], and we discuss the effect of different levels of k_c on the lifetime of the dynamo in the liquid core in section 4.2. Values of ρ, α, g, and σ used in the calculation of Re_m are mass-weighted average for the liquid iron core.

In general, unless the outer liquid iron core is very thin, so long as the liquid iron core exists and is convective, it could support a dynamo with $Re_m > Re_{m,crit}$. Using illustrative values for Earth-like and super-Earth planets for quantities in equations 2.52 and 2.54, $\sigma \sim 10^6\,\mathrm{S\,m^{-1}}$, $L_c \sim 10^6$ m, $\rho \sim 10^4\,\mathrm{kg\,m^{-3}}$, $c_P = 840\,\mathrm{kg\,J^{-1}\,K^{-1}}$, $g \sim 10\ \mathrm{m\,s^{-2}}$ and $\alpha \sim 10^{-5}\mathrm{K^{-1}}$, the required F_c to sustain a dynamo in the liquid iron core is very low $\sim 10^{-10}\mathrm{W\,m^{-2}}$. Since $F_\mathrm{cond} >> 10^{-10}\mathrm{W\,m^{-2}}$, Re_m of the liquid iron core will exceed $Re_{m,crit}$ as long as it is convecting. However, in cases where the liquid iron core is thin (i.e., as the core approaches complete solidification), Re_m may drop below the critical value and the dynamo might cease even while convection continues. For example, if L_c decreases to 10km, the required F_c to sustain a dynamo increases to $\sim 0.1\mathrm{W\,m^{-2}}$, which is non-negligible compared to F_cond (typically $\sim 0.1\mathrm{W\,m^{-2}}$ for $k_c = 80\mathrm{Wm^{-1}K^{-1}}$).

APPENDICES

We give a brief overview on the modified mixing length formulation, which is used to estimate the convective heat flow within the planetary interior. The original formulation [Abe, 1995] was derived for thermal convection driven by thermal profiles with super-adiabatic temperature gradients. The formula for $F_{\rm conv}$ for viscous fluid and inviscid fluid are given by Sasaki and Nakazawa [1986b] and Vitense [1953]. Here, we derive the same formula in terms of the entropy gradient, since entropy is a natural coordinate for convecting systems of both pure solid/liquid and partially molten aggregates. We further develop similar formulae for convection driven by super-adiabatic melt fraction gradients.

2.A Fundamentals of the modified mixing length formulation

The general idea of the mixing length theory is that a thermal fluid parcel in the planetary interior can move in between regions with high and low heat content due to a buoyancy force. The thermal parcel can move for a characteristic distance of l before it merges with the surroundings. For thermal convection, the buoyancy force is generated by a temperature difference between the fluid parcel and the surroundings, and the heat flux can be written as

$$F_{\rm conv} = \frac{1}{2}\rho c_P v \Delta T, \tag{2.60}$$

where ρ is the density, c_P is the specific heat capacity per unit mass, v is the fluid velocity. ΔT is the temperature difference between the fluid parcel and the surroundings, which is generated as the fluid parcel moves for l, and is estimated as $\Delta T = l[(\partial T/\partial r)_s - \partial T/\partial r]$, where $(\partial T/\partial r)_s$ is the adiabatic temperature gradient. The numerical factor $1/2$ comes from the fact that about half of the matter rises and the other half descends at any location with convective instability.

In cases where the viscous drag force is significant, the fluid velocity is constrained by

the Stokes flow, and is given by the Stokes velocity,

$$v = \frac{2\Delta\rho l^2 g}{9\rho\nu}, \tag{2.61}$$

where g is the local gravitational acceleration, ν is the kinematic viscosity, and $\Delta\rho$ is the density difference between the surrounding fluid and the fluid parcel, and approximated as $\Delta\rho = \rho\alpha\Delta T$. Convective instability occurs when $\Delta\rho$ is positive. Plugging equation 2.61 into equation 2.60, and adding an additional numerical factor of $1/2$ to match the original formulae provided in Sasaki and Nakazawa [1986b] and Abe [1995], we obtain

$$F_{\text{conv}} = \frac{\rho c_P \alpha g l^4}{18\nu} \left(\left.\frac{\partial T}{\partial r}\right|_s - \frac{\partial T}{\partial r} \right)^2. \tag{2.62}$$

We note that the numerical factor of $1/2$ is inconsequential as equation 2.62 is calibrated against a 1-D boundary layer theory model for rocky planets to obtain the proper mixing length [Tachinami et al., 2011] (but nonetheless should be included to ensure proper calibration). The effective eddy diffusivity, $\kappa_h \sim vl$, is obtained from equation 2.33 as

$$\kappa_h = \frac{\alpha g l^4}{18\nu} \left(\left.\frac{\partial T}{\partial r}\right|_s - \frac{\partial T}{\partial r} \right). \tag{2.63}$$

Both temperature gradients are defined to be negative. Convective instability does not occur when $(\partial T/\partial r)_s \leq \partial T/\partial r$, in which case F_{conv} and κ_h are both 0.

Now we want to express the temperature gradients in terms of the entropy gradient, $\partial s/\partial r$. $\partial T/\partial r$ can be expressed as

$$\begin{aligned} \frac{\partial T}{\partial r} &= \left.\frac{\partial T}{\partial P}\right|_s \frac{\partial P}{\partial r} + \left.\frac{\partial T}{\partial s}\right|_P \frac{\partial s}{\partial r} \\ &= \left.\frac{\partial T}{\partial r}\right|_s + \frac{T}{c_P}\frac{\partial s}{\partial r}. \end{aligned} \tag{2.64}$$

Now we can rewrite $\Delta\rho$, ΔT, F_{conv} and κ_h in terms of the entropy gradient,

$$\Delta T = -l\frac{T}{c_P}\frac{\partial s}{\partial r}, \tag{2.65}$$

$$\Delta \rho = -\rho\alpha l\frac{T}{c_P}\frac{\partial s}{\partial r}, \tag{2.66}$$

$$F_{\text{conv}} = \frac{\rho\alpha g T^2 l^4}{18\nu c_P}\left(\frac{\partial s}{\partial r}\right)^2, \tag{2.67}$$

$$\kappa_h = -\frac{\alpha g T l^4}{18 c_P \nu}\frac{\partial s}{\partial r}. \tag{2.68}$$

Convection occurs when the entropy gradient is negative, and F_{conv} and κ_h are calculated using equations 2.67 and 2.68. Otherwise, both F_{conv} and κ_h are 0.

In cases where viscosity is low and viscous drag force is insignificant, then the flow velocity is the free fall velocity estimated based on the energy exchange between the gravitational potential energy and kinematic energy of the fluid parcel. The sum of the buoyancy force and gravity on the fluid parcel per unit volume is $f = g\Delta\rho$. The fluid parcel can rise (i.e. convective instability occurs) when f is positive. The work done on the fluid parcel per unit volume to move it through a distance l is

$$W(l) = \int_0^l g\Delta\rho dl' = g\int_0^l \Delta\rho dl' = \frac{1}{2}g\Delta\rho l. \tag{2.69}$$

Assuming $W(l)$ could all be transformed into kinetic energy of the parcel, $E_k = \rho v^2/2$, then the fluid velocity is

$$v = \left(\frac{g\Delta\rho l}{\rho}\right)^{0.5}, \tag{2.70}$$

and $\Delta\rho$ is the same density difference between the fluid parcel and the surrounding fluid as in equation 2.61. Plugging this velocity into equation 2.60 and including the numerical factor of $1/2$ to match the formula in Vitense [1953] and Abe [1995], we have

$$F_{\text{conv}} = \rho c_P \sqrt{\frac{\alpha g l^4}{16} \left(\left.\frac{\partial T}{\partial r}\right|_s - \frac{\partial T}{\partial r} \right)^3}, \tag{2.71}$$

and

$$\kappa_h = \sqrt{\frac{\alpha g l^4}{16} \left(\left.\frac{\partial T}{\partial r}\right|_s - \frac{\partial T}{\partial r} \right)}. \tag{2.72}$$

We now use equation 2.64 to rewrite equations 2.71 and 2.72 in terms of the entropy gradient instead of the temperature gradient, we have

$$F_{\text{conv}} = \rho T \sqrt{-\frac{\alpha g T l^4}{16 c_P} \left(\frac{\partial s}{\partial r} \right)^3}, \tag{2.73}$$

and

$$\kappa_h = \sqrt{-\frac{\alpha g T l^4}{16 c_P} \frac{\partial s}{\partial r}}. \tag{2.74}$$

The convection criterion for inviscid fluid remains the same as that for viscous fluid.

The transition criterion between the low and high viscosity regimes is determined based on Stokes velocity and the free fall velocity of the fluid parcel. The convective heat flux and κ_h are limited by the either one of the slower velocity. We determine the transition by equating equations 2.61 and 2.70,

$$\frac{\Delta \rho g l^3}{18 \rho \nu^2} = \frac{9}{8}. \tag{2.75}$$

Plugging equation 2.66 into equation 2.75, we obtain the transition criterion

$$-\frac{\alpha g T l^4}{18 c_P \nu^2} \frac{\partial s}{\partial r} = \frac{9}{8}. \tag{2.76}$$

When the quantity on the left side of equation 2.76 is greater than 9/8, the convective heat flow is then in the low viscosity regime, otherwise the flow is in the high viscosity regime.

2.B Modified mixing length formulation for solid and liquid mixtures

In this section, we aim to extend the modified mixing length formulation described in appendix 2.A and develop a formula to estimate the convective heat flow within a mixture of solid and liquid phases. Herein, we consider the case where the two phases are well mixed and do not separate (no rain-out); the solid condensate (fluid melt) is completely entrained with the fluid (solid). For a pure substance, the temperature of a solid-liquid mixture is fixed on the melting curve. The density of the solid and liquid mixture is

$$\rho = \left(\frac{x}{\rho_m} + \frac{1-x}{\rho_s} \right)^{-1}, \tag{2.77}$$

where ρ_m and ρ_s are the densities of the liquid and solid phases on the melting curve.

The buoyancy force that drives the convection is generated by a difference in the melt fraction between the adiabatically displaced fluid parcel and the surroundings. The fluid parcel carries latent heat with it as it moves up and down due to the convection, and the convective heat flux is

$$F_{\text{conv}} = \frac{1}{2} \rho L v \Delta x, \tag{2.78}$$

where L is the latent heat of fusion and Δx is the difference in melt fraction between the fluid parcel and the surrounding fluid. Similar to ΔT in thermal convection, Δx can be approximated as $\Delta x = l \left[(\partial x / \partial r)_s - \partial x / \partial r \right]$, with $(\partial x / \partial r)_s$ being the adiabatic melt fraction gradient.

In the case where viscous drag force is significant, the flow velocity is given by equation 2.61. Including the factor of $1/2$ the same way as equation 2.62, the convective heat flux is

$$F_{\text{conv}} = \frac{L\Delta\rho l^3 g}{18\nu}\left(\left.\frac{\partial x}{\partial r}\right|_s - \frac{\partial x}{\partial r}\right), \tag{2.79}$$

where $\Delta\rho$ is the density difference between the surrounding material and the fluid parcel. In analogy to the thermal expansion coefficient, we define an expansion coefficient due to changes in melt fraction, α_x,

$$\alpha_x \equiv -\frac{1}{\rho}\left.\frac{\partial \rho}{\partial x}\right|_P = \rho\left(\frac{1}{\rho_m} - \frac{1}{\rho_s}\right), \tag{2.80}$$

so that $\Delta\rho = \rho\alpha_x\Delta x$. Substituting this expression back into equation 2.79, we have

$$F_{\text{conv}} = \frac{\rho\alpha_x L g l^4}{18\nu}\left(\left.\frac{\partial x}{\partial r}\right|_s - \frac{\partial x}{\partial r}\right)^2, \tag{2.81}$$

and κ_h is obtained using equation 2.33

$$\kappa_h = \frac{\alpha_x g l^4}{18\nu}\left(\left.\frac{\partial x}{\partial r}\right|_s - \frac{\partial x}{\partial r}\right). \tag{2.82}$$

The next goal is to rewrite the melt fraction gradient in terms of the entropy gradient. The specific entropy of a solid and liquid mixture is

$$s = x s_m + (1-x)s_s, \tag{2.83}$$

where s_m and s_s are the specific entropy of the liquid and solid components on the melting curve. We expand $\partial s/\partial r$ and express it as

$$\frac{\partial s}{\partial r} = \left[x\left(\frac{\mathrm{d}s_m}{\mathrm{d}P} - \frac{\mathrm{d}s_s}{\mathrm{d}P}\right) + \frac{\mathrm{d}s_s}{\mathrm{d}P}\right]\frac{\partial P}{\partial r} + (s_m - s_s)\frac{\partial x}{\partial r}. \tag{2.84}$$

Rearranging the equation, we obtain

$$\frac{\partial x}{\partial r} = -\frac{1}{s_m - s_s}\left[x\left(\frac{\mathrm{d}s_m}{\mathrm{d}P} - \frac{\mathrm{d}s_s}{\mathrm{d}P}\right) + \frac{\mathrm{d}s_s}{\mathrm{d}P}\right]\frac{\partial P}{\partial r} + \frac{1}{s_m - s_s}\frac{\partial s}{\partial r}. \tag{2.85}$$

The first term on the right side of the equation is the adiabatic melt fraction gradient and the second term is the super-adiabatic component. Given that $s_m - s_s = L/T_m$ with T_m being the melting temperature, we have

$$\left.\frac{\partial x}{\partial r}\right|_s - \frac{\partial x}{\partial r} = -\frac{T_m}{L}\frac{\partial s}{\partial r}. \tag{2.86}$$

Putting this into equations 2.81 and 2.82, we have

$$F_{\mathrm{conv}} = \frac{\rho\alpha_x g T_m^2 l^4}{18L\nu}\left(\frac{\partial s}{\partial r}\right)^2, \tag{2.87}$$

and

$$\kappa_h = -\frac{\alpha_x g T_m l^4}{18L\nu}\left(\frac{\partial s}{\partial r}\right). \tag{2.88}$$

The convective instability can occur when the entropy gradient is negative.

In the case where the viscous drag force is insignificant, the convective heat flow is limited by the free fall velocity (equation 2.70). Again, with the numerical factor $1/2$, the convective heat flow and κ_h are

$$F_{\mathrm{conv}} = \rho T_m\sqrt{-\frac{\alpha_x g T_m l^4}{16L}\left(\frac{\partial s}{\partial r}\right)^3}, \tag{2.89}$$

and

$$\kappa_h = \sqrt{-\frac{\alpha_x g T_m l^4}{16L}\frac{\partial s}{\partial r}}. \tag{2.90}$$

The transition criterion between the low and high viscosity regimes for convection driven by a super-adiabatic melt fraction gradient is still given by equation 2.75. Substituting the

expression for $\Delta\rho$ due to melt fraction differences between the parcel and surroundings into equation 2.75, we have

$$-\frac{\alpha_x g T_m l^4}{18 L \nu^2}\frac{\partial s}{\partial r} = \frac{9}{8}. \tag{2.91}$$

When the quantity on the left side of equation 2.91 is greater than $9/8$, the convective heat flow is then in the low viscosity regime, otherwise the flow is in the high viscosity regime.

CHAPTER 3

THERMAL AND MAGNETIC HISTORY OF AN EARTH-LIKE CASE

3.1 Introduction

In this chapter, we present our simulations of magma ocean solidification and late-time evolution after the mantle fully solidifies for an $1M_{\oplus}$ planet with CMF=0.33 and $T_{eq} = 255K$. We compare our results to previous work [Lebrun et al., 2013, Solomatov, 2015, Tachinami et al., 2011] as well as observations of current-day Earth [Dziewonski and Anderson, 1981, Davies and Davies, 2010] to validate our model approach. Additionally, we aim to assess the possibility of the liquid core and the magma ocean of hosting a dynamo source region, and the lifetime of the dynamo sources within.

3.2 Evolution of an Earth-like case

3.2.1 Thermal history of an Earth-like case

Here we present the thermal evolution and magnetic history of a representative case: an Earth-like planet with $M_{\rm pl} = 1M_{\oplus}$ and CMF= 0.33. The core is made of iron and 10% Si (a proxy for light elements) by mass, and the mantle is made of $MgSiO_3$ in various phases (liquid, post-perovskite, bridgmanite, and enstatite). We assume no atmosphere at the planet surface. We consider the lower-bound rheology [Tackley et al., 2013] for ppv when calculating its viscosity and a core radioactivity of 1 TW at present day (∼140 ppm potassium). Figure 3.2.1(a) shows the evolution of the temperature profile ($T(P)$) throughout the entire planet and Figure 3.2.1(b) shows the evolution of the heat flux at the CMB ($F_{\rm CMB}$), which is indicative of the cooling rate of the core.

The cooling history of the planet is split into 3 stages: (i) from $t = 0$ to $t \sim 1$ kyr (ii) from $t \sim 1$ kyr to $t \sim 10$ Myr and (iii) after $t \sim 10$ Myr. During stage (i), the cooling rate of the mantle is extremely rapid due to the low viscosity of molten and partially molten silicate. As figure 3.2.1(b) shows, the temperature at the base of the mantle decreases from ~ 5500 K to ~ 4600 K during this time. $\delta_{\rm LBL}$, the lower conductive boundary layer at the

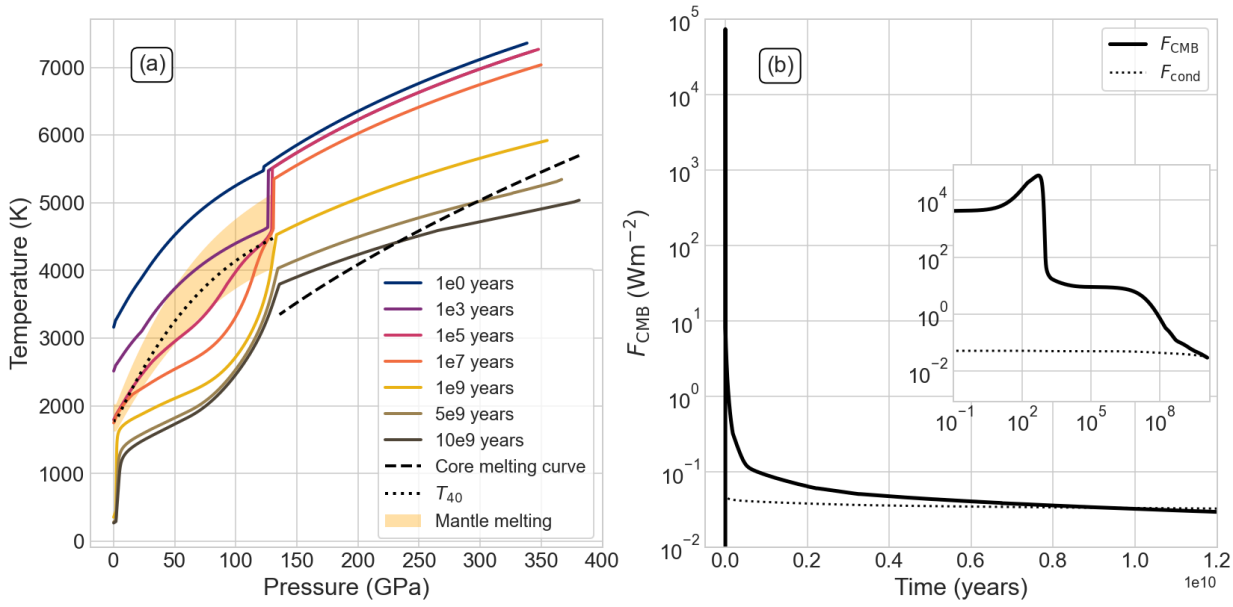

Figure 3.2.1: Evolution of (a) the temperature profile for the entire planet and (b) the heat flux at the CMB for a $1M_{\oplus}$ planet with a CMF of 0.3 and a iron-dominated core and $MgSiO_3$ mantle composition. The orange shaded area in (a) is for the silicate melting interval (solidus-liquidus) and the dotted curve in (a) is the temperature corresponding to 40% melt fraction (T_{40}). The dashed curve in (a) is the melting curve of the iron-dominated core. The embedded plot in (b) is the evolution of $F_{\rm CMB}$ in log-log space to highlight the behavior in the first 0.1 Gyr. The dotted curve in (b) shows the conductive flux along the adiabat of the core with k_c =40 $\rm Wm^{-1}K^{-1}$. $F_{\rm CMB}$ has to exceed the conductive flux in order to have a positive thermal buoyancy flux.

base of the mantle is ultrathin (∼0.1 m) due to its low viscosity, resulting in a high level of F_{CMB} on the order of $10^4 \mathrm{Wm}^{-2}$. With the rapid cooling in the mantle in the first 1 kyr, the temperature difference across the lower boundary layer builds up, leading to an increase in F_{CMB}. At the end of stage (i), F_{CMB} peaks at $\sim 8 \times 10^4$ Wm^{-2} with $\delta_{\mathrm{LBL}} \sim 0.08$ m, ΔT_{LBL} ∼700 K and $k = 10 \mathrm{Wm}^{-1}\mathrm{K}^{-1}$.

During stage (ii), the mantle continues to solidify, and the temperature profile in the mantle first reaches T_{40} from its base. Upon reaching a temperature of T_{40}, the partially molten silicate experiences a rheology transition where its viscosity changes from liquid-like to solid-like. For example, the viscosity at the base of the mantle increases from $\sim 100 \mathrm{Pa} \cdot \mathrm{s}$ to $\sim 10^{16} \mathrm{Pa} \cdot \mathrm{s}$ from the beginning to the end of stage (ii). The rheology transition front progresses toward the planet surface and reaches the surface at the end of stage (ii). The total mass fraction of solid in the mantle reaches over 95% at the end of stage (ii) and mantle heat transport becomes dominated by solid-state convection.

The start of stage (ii) is marked by an abrupt drop in F_{CMB} from $\sim 8 \times 10^4$ Wm^{-2} to ∼10 Wm^{-2}, following which F_{CMB} stays fairly constant for the remainder of stage (ii). The sudden decrease in the core cooling rate is triggered by a thickening of the lower boundary layer in the mantle. δ_{LBL} increases from $\sim$ 0.1 m to over 1 km in stage (ii) due to the increase in viscosity at the base of the mantle. As the mantle solidifies, it compresses the iron-dominated core and P_{CMB} increases from ∼126 GPa to ∼132 GPa. The core experiences heating due to adiabatic compression, which is comparable to the core cooling rate during this stage. Consequently, the core temperature only experiences a minor decrease in the 10 Myr time period (∼60 K).

In the last stage (iii), the mantle heat transport is dominated by solid state convection. As the mantle continues to cool over the remainder of the evolution, its viscosity increases and reduces the convective heat flux in the mantle. As indicated by the temperature profiles in Figure 3.2.1(a), the temperature in the mantle decreases at a progressively slower rate.

Meanwhile, the core continues to lose heat to the mantle and the temperature difference across the lower boundary layer in the mantle decreases over time, which lowers F_{CMB} (Figure 3.2.1b) and slows the cooling rate of the core. With $k_c = 40 \mathrm{Wm^{-1}K^{-1}}$, F_{CMB} stays above F_{cond} for the entire simulation of 12 Gyr, indicating that thermal convection in the liquid outer core can operate for at least 12 Gyr. If k_c increases to 80 $\mathrm{Wm^{-1}K^{-1}}$, thermal convection shuts off at ∼9 Gyr.

Our thermal evolution result for the Earth-like case is in decent agreement with previous models and observations of Earth. We predict the surface heat flow to be ∼0.072 $\mathrm{Wm^{-2}}$ at ∼4.5 Gyr, which agrees well with the value predicted by Tachinami et al. [2011], ∼0.08 $\mathrm{Wm^{-2}}$. The result is also in decent agreement with the current observed surface heat flow of Earth, ∼ 0.09 $\mathrm{Wm^{-2}}$ [Davies and Davies, 2010]. The onset of inner core solidification happens around 3.3 Gyrs. This puts the ∼1 Gyr age of the solid inner core predicted by our model within the 0.5-2 Gyrs range indicated by many previous thermal models of Earth [e.g., Tachinami et al., 2011, Driscoll and Bercovici, 2014, Labrosse, 2015, Zhang et al., 2020]. The solid inner core grows to ∼ 1300 km at 4.5 Gyrs, which is comparable to the results of Tachinami et al. [2011] and Driscoll and Bercovici [2014] and the observed value of current day Earth, ∼1221 km [Dziewonski and Anderson, 1981].

Our model obtains an interior structure comparable to that of present-day Earth using the Henyey code. Figure 3.2.2 shows the radial density profile of the planet at 4.5 Gyrs with comparison to results of Preliminary Reference Earth Model [PREM, Dziewonski and Anderson, 1981]. The comparison shows decent agreement and the mismatch in the planetary radius is less than 0.1%, which further validates our modeling approach. The discrepancy in the inner core density between PREM and the result shown in Figure 3.2.2 (b) is due to the presence of elements lighter than iron in Earth's inner core and our choice to keep all light impurities in the liquid outer core in this case.

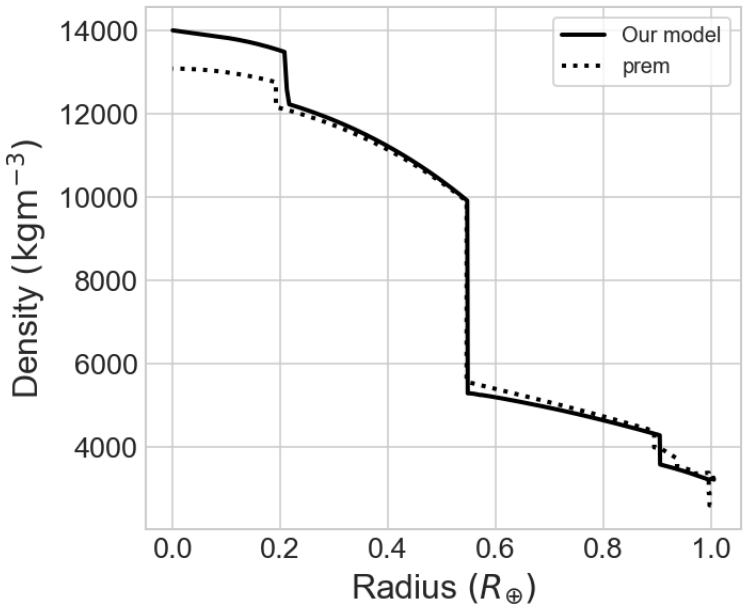

Figure 3.2.2: Model predicted radial density profile at 4.5 Gyrs and comparison to the result from Preliminary Reference Earth Model [PREM, Dziewonski and Anderson, 1981]. Our model predicted a higher density in the solid inner core due to the lack of light impurities. The model predicted planetary radius is in excellent agreement with the PREM result.

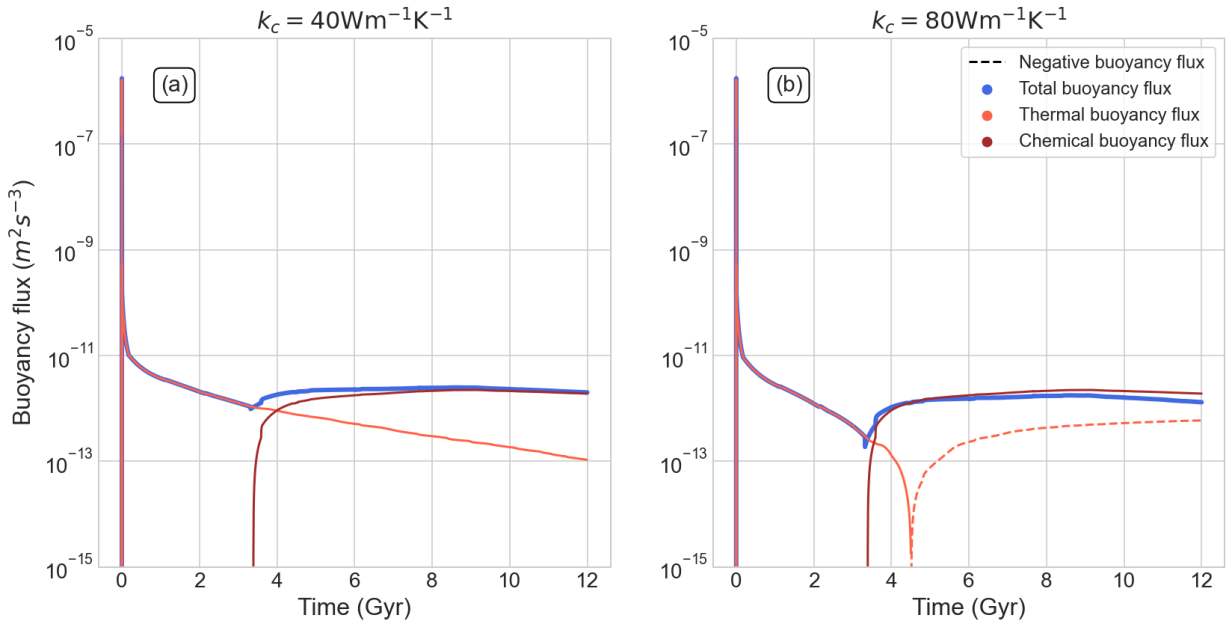

Figure 3.2.3: Evolution of buoyancy fluxes in the liquid core of a $1M_\oplus$ planet with CMF=0.33 and (a) $k_c = 40\mathrm{Wm}^{-1}\mathrm{K}^{-1}$, (b) $k_c = 80\mathrm{Wm}^{-1}\mathrm{K}^{-1}$. In both panels, red, brown and blue curves indicate thermal (F_T), chemical (F_x) and total buoyancy fluxes. Dashed curves represent a negative thermal buoyancy flux, which is the amount the chemical buoyancy flux has to overcome to keep the liquid core unstable to convection. Positive total/thermal buoyancy flux indicates an active dynamo in the liquid iron core with/without the contribution of chemical buoyancy flux.

3.2.2 Magnetic history of an Earth-like case

In this section, we discuss the lifetime of the dynamo in the liquid core of the representative Earth-like planet ($M_{\mathrm{pl}} = 1M_\oplus$ and CMF=0.33) when sustained by only thermal convection or by both thermal and compositional convection. In cases where the dynamo is driven solely by thermal convection, we assume the partitioning of light elements is comparable between the solid and liquid phases of iron and thus that there is no exsolution of light elements into the liquid core as the solid inner core forms. A positive F_T is required to maintain an active dynamo for these cases. In cases where the dynamo is driven by both thermal and compositional convection, we take the other extreme and assume that all light elements partition into the liquid outer core as the inner core crystallizes. For these cases, the sum

of F_T and F_x needs to be positive to maintain an active dynamo. Figure 3.2.3 shows the evolution of F_T and F_x, as well as the total buoyancy fluxes for two choices of k_c (40 and 80 $\mathrm{Wm^{-1}K^{-1}}$).

The thermal buoyancy flux can reach as high as $\sim 10^{-6}\mathrm{m^2s^{-3}}$ at the beginning of the evolution (stage i) due to the high level of F_{CMB} ($\sim 10^4\mathrm{Wm^{-2}}$). As the cooling rate of the liquid core slowly decreases in stage (iii) (figure 3.2.1(b)), F_T gradually decreases as well. In the absence of chemical buoyancy flux, the dynamo can operate for the entirety of the simulation (12 Gyr) with $k_c = 40\mathrm{Wm^{-1}K^{-1}}$ and for ∼4.5 Gyr with $k_c = 80\mathrm{Wm^{-1}K^{-1}}$.

Chemical buoyancy may contribute to sustaining the dynamo in the liquid core if light elements are expelled from the inner to the outer core during inner core crystallization. We calculate the chemical buoyancy flux of this planet under the assumption that all light elements are partitioned into the liquid outer core. As indicated by the brown curves in both panels of Figure 3.2.3, the inner core starts crystallizing and F_x becomes positive at ∼3 Gyr. In the case where $k_c = 40\mathrm{Wm^{-1}K^{-1}}$, the dynamo is always generated in part by thermal convection, as F_T remains positive for the entire simulation. The outer core buoyancy flux experiences a boost due to the inner core crystallization at ∼3 Gyr. When k_c is $80\mathrm{Wm^{-1}K^{-1}}$, the dynamo lifetime could increase from ∼4.5 Gyr to over 12 Gyr with the contribution of chemical buoyancy.

3.3 Magma ocean as an alternative dynamo source

3.3.1 Magma ocean solidification

We first validate our models by comparing the magma ocean's solidification timescale with previous work [Lebrun et al., 2013, Solomatov, 2015]. We simulate the magma ocean solidification of an $1M_\oplus$ planet with an Earth-like composition — an iron-dominated core and silicate mantle with a core mass fraction of 0.33 — following the procedure described in

chapter 2.

To facilitate the comparison, we run simulations both with and without a degassed atmosphere. In the case that considers a degassed atmosphere, we use the same initial water (4.3×10^{-2}wt%) and CO_2 (1.4×10^{-2}wt%) content as Lebrun et al. [2013]. The atmosphere is treated as a gray emitter and the surface heat flux is calculated using equations 7-9 in Elkins-Tanton [2008]. The surface heat flux is modified by the emissivity of the atmosphere, which is a function of the mass of the atmosphere. The evolution of surface heat flux (F_{surf}) and fraction of total mantle mass in the liquid phase ($x_m = \int_{\text{CMB}}^{\text{surf}} x dm / M_{\text{mantle}}$) with and without an overlying steam atmosphere are shown in figure 3.3.1.

Following Lebrun et al. [2013], we divide the solidification of magma ocean into three stages: (i) totally molten stage, (ii) partially molten stage, where the magma ocean starts solidifying from the CMB to the planet surface, and (iii) mush stage, where a cold thermal boundary layer starts developing at the surface and the surface temperature approaches the planet equilibrium temperature (T_{eq}). The totally and partially molten stage corresponds to stage (i) and the mush stage corresponds to stage (ii) in section 3.2.1.

As shown in figure 3.3.1 (a), stages (i) and (ii) are fairly short ($\sim$1 kyrs), when there is no insulating atmosphere at the planet surface. During these stages, the convection is extremely vigorous due to the low viscosity of molten silicate, and the surface heat flow can reach as high as $5\times \sim 10^5$ Wm^{-2}. As the mantle cools down rapidly, the magma ocean starts solidifying from the bottom and becomes partially molten near the CMB at $\sim$ 100 years. This partially molten zone quickly expands from the CMB to the surface in the next $\sim$1 kyrs and x_m drops to around 25% in this time period. After the surface starts solidifying, the thermal boundary layer at the planet surface starts thickening due to an increasing local viscosity and the mush stage begins. The solidification of the magma ocean slows significantly during the mush stage in comparison to the molten and partially molten stages due to the decreasing F_{surf}. The mantle fully solidifies at $\sim$500 Myr.

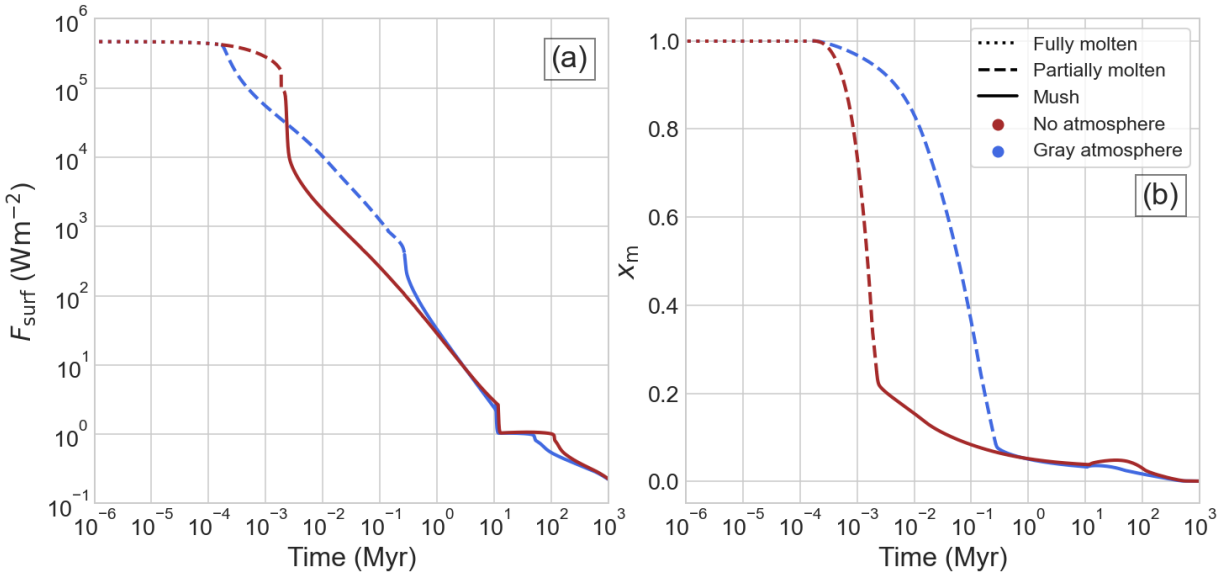

Figure 3.3.1: Evolution of (a) surface heat flow (F_{surf}) and (b) fraction of total mantle mass in the liquid phase (x_m) for a 1 $M_\oplus$ planet with CMF=0.326 and T_{eq}=255K. Brown curves are for the case with no atmosphere and blue curves are for the case with a degassed gray atmosphere with initial water content of 4.3×10^{-2}wt% and CO_2 content of 1.4×10^{-2}wt%. Dotted, dashed and solid curves represent the fully molten stage, the partially molten stage and the mush stage. Discontinuities at ∼10 Myr are numerical artifacts that appear when the thermal boundary at the planet surface reaches the thickness of the top cell in the planet and stops growing.

Even though we use a different prescription of surface heat flux (equation 2.48) from the parameterized surface flux used by Lebrun et al. [2013], the lifetimes of totally and partially molten stages are comparable, ∼1 kyrs. Our result also agrees qualitatively with the magma ocean crystallization timescale predicted by the scaling law by Solomatov [2015] within an order of magnitude (∼ 400 years). In addition, our model predicts a similar level of F_{surf} during all three stages of magma ocean solidification as compared to Lebrun et al. [2013], from $\sim 10^6$ Wm^{-2} during the totally molten stage to less than 10 Wm^{-2} during the mush stage. However, we predict F_{surf} to decrease gradually upon entering the mush stage (see Figure 3.3.1(a)), whereas it has a sudden decrease to $\sim$10Wm^{-2} when approaching the mush stage (see Figure 3(d) in Lebrun et al. [2013]). This is caused by different viscosity models for partially molten silicate. Lebrun et al. [2013] considers a drastic increase in the viscosity of the partial melts as the melt fraction decreases to the $x_{crit} = 0.4$, whereas we include a transition function to smooth the abrupt change in the viscosity. As a result, the thermal boundary layer at the planet surface has an abrupt growth before the start of the mush stage in Lebrun et al. [2013], whereas it grows gradually for the entirety of the mush stage.

Including a degassed atmosphere during the magma ocean solidification results in a slower cooling process than when no atmosphere is present. This increases the duration of the totally and partially molten stage to ∼0.3 Myrs and thus delays the mush stage. This result differs from that predicted by Lebrun et al. [2013] (∼0.2 Myrs when the atmosphere is treated as a gray emitter) by 50%. We attribute the difference mainly to the different partition coefficients of volatiles in mantle silicate, as we assume all volatiles are degassed into the atmosphere while Lebrun et al. [2013] considers non-zero partition coefficients. These illustrative simulations highlight the sensitivity of the magma ocean evolution to the choice of atmospheric boundary condition. Results presented in this section are qualitatively comparable to those of Lebrun et al. [2013] and Solomatov [2015]. This gives our model the credibility to simulate magma ocean solidification on rocky planets.

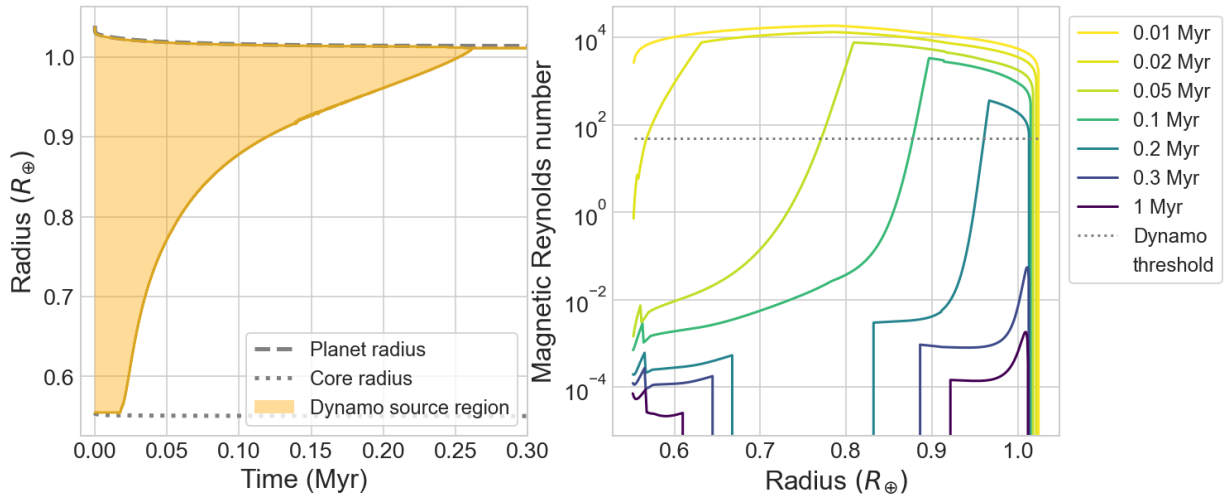

Figure 3.3.2: Time evolution of (a) dynamo source region and (b) magnetic Reynolds number profiles of the magma ocean for $1M_\oplus$ planet with CMF=0.326 and a degassed gray atmosphere with initial water content of 4.3×10^{-2}wt% and CO_2 content of 1.4×10^{-2}wt%. The dotted line in (b) indicates the threshold above which the region can potentially support a dynamo.

3.3.2 Dynamo source region in the magma ocean

As explained in section 2.10, a dynamo may be sustained in the magma ocean where Re_m exceeds the critical value of 50. Figure 3.3.2(a) shows the evolution of the dynamo source region in the magma ocean and figure 3.3.2(b) shows the evolution of the magnetic Reynolds number profile of a Earth-like case with a degassed gray atmosphere with an initial water and CO_2 content of 4.3×10^{-2} and 1.4×10^{-2}wt% of mass of Earth's mantle respectively. At the very beginning of our simulation, the entire liquid mantle could potentially generate a magnetic field, with a low viscosity (100 Pa s) and a magnetic Reynolds number ($\gtrsim$ 10000) well above the dynamo threshold ($\sim$ 50) throughout the entire mantle. As the mantle becomes partially molten, the melt fraction descends below x_{crit} starting from the CMB and moving upward in ~0.25 Myr. In the region with $x < x_{crit}$, the magnetic Reynolds number, which depends on the convective velocity, is limited by the viscous drag force (with a ~10 orders of magnitude increase in the viscosity level compared to $x > x_{crit}$, equation 2.61) and

declines below the dynamo threshold. The thickness of the dynamo source region decreases from over 3000 km to 0 in this time period. Even though the magma ocean does not fully solidify until ∼500 Myr, the dynamo source in the magma ocean is only viable where the melt fraction is high enough to allow liquid-like convection. Hence, the dynamo source in the magma ocean shuts off around the time the solidification front reaches the planet surface at ∼0.25 Myr.

3.4 Discussion and conclusion

In this chapter, we apply our 1D thermal evolution model coupled with a Henyey solver to explore the thermal and magnetic history of an Earth-like planet ($M_{\rm pl} = 1M_{\oplus}$ and CMF=0.33). In particular, we consider a planet with an $MgSiO_3$ mantle (liquid, enstatite, bridgmanite and post-perovskite phase) and a iron-dominated core with 10wt% of Si as a proxy for light elements. The results shown in this chapter serve to validate our modeling approach and to illustrate the capabilities of our code. In addition, we discuss the possibility of the liquid core and the magma ocean being a dynamo source region in the interior of the planet. We summarize the thermal evolution and dynamo source region results here.

Thermal history of the Earth-like case with a low k_c predicts a long lasting dynamo driven by thermal convection alone (∼9 Gyr with $k_c = 40 \mathrm{Wm^{-1}K^{-1}}$). However, an increasing number of studies suggest that k_c under core conditions is larger, between 70-200 $\mathrm{Wm^{-1}K^{-1}}$[e.g. de Koker et al., 2012, Inoue et al., 2020, Pozzo et al., 2012, Zhang et al., 2020]. Increasing k_c to 80 $\mathrm{Wm^{-1}K^{-1}}$, we find that thermal convection shuts off after ∼4.5 Gyr, and the dynamo could only operate if there is compositional buoyancy provided by the inner core solidification. If k_c in Earth's core is larger than 80 $\mathrm{Wm^{-1}K^{-1}}$, thermal convection could shut off before the onset of inner core solidification. As a result, the liquid core could become thermally stratified and the dynamo could not operate. This is not supported by paleomagnetic evidence that suggests an ancient geodynamo going back 3-4 Gyr [e.g., Bono et al., 2019].

A systemic study, such as Driscoll and Davies [2023], that explores of uncertainties in core thermal conductivity, core radiogenic heat production rate, melting curve of the core, lower mantle viscosity and initial CMB temperature may shed a light on this.

The dynamo source region in the magma ocean is confined to the region where the melt fraction is above the x_{crit}. The liquid/solid assemblages in such regions behave like a liquid and therefore could have a convective velocity great enough to support a dynamo. In comparison, partially molten silicate with low melt fraction is solid-like. The viscous drag force dramatically suppresses the convective velocity and the dynamo shuts off. Melt fraction greater than x_{crit} is a necessary but not sufficient criterion for $Re_m \geq 50$ in the magma ocean.

The magma ocean is unlikely to host a long-term dynamo in an Earth-like exoplanet. The dynamo could last only $\sim$0.3 Myr in the Earth-like case with a degassed atmosphere, which is a negligible fraction of the lifetime of a rocky planet. In addition, our predicted lifetime of the dynamo in the magma ocean is likely to be an upper limit, as we ignore the gravitational separation between melt and solid as the magma ocean solidifies. As shown in Bower et al. [2018], gravitational separation could contribute a positive heat flux in the partially melt region, which could speed up the solidification of the magma ocean. We will update our model to properly treat the mass and heat flux associated with gravitational separation between melt and solid in the future.

The magma ocean could potentially host a long-term dynamo in rocky planets with a high equilibrium temperature or a sub-Neptune-typed exoplanet. As shown in Zhang and Rogers [2022], a permanent magma ocean could persist at the surface of a rocky planet, if its equilibrium temperature is greater than the melting temperature of silicate at the planet surface. However, planets with such high $T_{\rm eq}$ are likely to be tidally locked and a magma pond could form on the star-facing side of highly-irradiated tidally locked planets instead of a global magma ocean [Gelman et al., 2011]. A 1D model like ours is not appropriate in this

case, as differences and heat transport between the sub- and anti-stellar hemispheres need to be accounted for to properly simulate their evolution. For sub-Neptune-type exoplanets, if the H/He envelope is significant enough, the temperature and pressure levels at the surface of the rocky interior could allow a permanent magma ocean to persist. Our thermal model for the rocky interior of a sub-Neptune-typed exoplanet needs to be coupled with a thermal model for the H/He envelope to properly simulate such cases.

CHAPTER 4

MAPS OF THE LIFETIME OF THE DYNAMO IN THE LIQUID CORE

4.1 Introduction

As stated previously in this thesis, magnetic fields or the lack of one may offer unique windows into the interior structure and dynamics of exoplanets. Many groups have looked into whether super-Earths are likely to host a dynamo-generated magnetic field or not.

Previous studies have suggested that it is unlikely for super-Earths to host a dynamo for various reasons. For example, Valencia et al. [2006] calculated the interior structure of super-Earths up to $10M_{\oplus}$ using scaling relations based on the thermal structure of current-day Earth. They concluded that the cores of super-Earths are likely to be fully solid owing to the great pressure. Thus super-Earths could not host a dynamo in their cores. Tachinami et al. [2011], on the other hand, ran a 1D thermal evolution simulation to explore the magnetic history of super-Earths. However, their model did not include post-perovskite, which has a lower viscosity compared to bridgmanite, and thus overestimated the viscosity of the lower mantles of super-Earths. Owing to an overestimated viscosity level in the lower mantles of super-Earths, Tachinami et al. [2011] predicted elevated temperatures in the lower mantles and small core-mantle temperature contrasts. As a result, they concluded that the liquid cores of super-Earths are thermally stratified and cannot host a dynamo.

More recent studies, however, predict that super-Earths are likely to host a dynamo in their liquid cores. Blaske and O'Rourke [2021] and Boujibar et al. [2020] calculated thermal structures of super-Earths at a single time in the evolution (a snapshot model), and determined that the cores of super-Earths have a higher heat loss rate, and thus could host a dynamo. Groups including Bonati et al. [2021] and Zuluaga et al. [2013] ran parameterized models (a 0-D approach) to simulate thermal evolution of super-Earths and reached the same conclusion. However, these studies either focus on super-Earths with $M_{\rm pl} < 5M_{\oplus}$ or planets with the same CMF as Earth.

In this chapter, we apply our 1D thermal evolution model coupled with a Henyey solver to a wide range of rocky planets with $M_{\rm pl}$ between 1 and $8M_{\oplus}$ and CMFs between 0.1 and

0.8. The main goal is to isolate the effect of $M_{\rm pl}$ and CMF on the thermal and magnetic history of rocky planets, and determine what combinations of $M_{\rm pl}$ and CMF could result in the greatest predicted lifetime for the core dynamo.

4.2 Results for the fiducial case

In this section, we discuss the lifetime of the dynamo in the liquid cores of planets with various planet masses (between 1 and 8 $M_\oplus$) and core mass fractions (between 0.1 and 0.8). We consider two scenarios: one where the dynamo is sustained by thermal convection alone, and where both thermal and compositional convection contribute. We consider 4 choices of k_c to calculate F_T and evaluate its effect over the dynamo lifetime, 40, 80, 120 and 160 $Wm^{-1}K^{-1}$. For the fiducial case, we consider the same model for the viscosity of $MgSiO_3$ and the same amount of radiogenic heating per unit mass as the representative case in section 3.2. We discuss the impact of different models of mantle viscosity and amount of radiogenic heating in the core in sections 4.3 and 4.4. Results for the lifetime of the dynamo driven by thermal convection alone and by both thermal and compositional convection are summarized in figures 4.2.1 and 4.2.7.

4.2.1 The lifetime of the dynamo driven by thermal convection

The lifetime of the possible dynamo source in the liquid core is closely related to the lifetime of thermal convection therein, i.e. the time period for which the liquid iron core exists and stays convective. In cases where the liquid iron core does not fully solidify, so long as the liquid iron core is convecting, its magnetic Reynolds number will exceed $Re_{m,crit}$. This was argued based on order-of-magnitude reasoning in section 2.10 and is born out in our simulations (Figure 4.2.1). On the other hand, in cases where the entire core solidifies before thermal convection stops (i.e., $F_T > 0$ at the time of complete solidification), the dynamo may shut off shortly before the solidification of the convective liquid core as L_c decreases

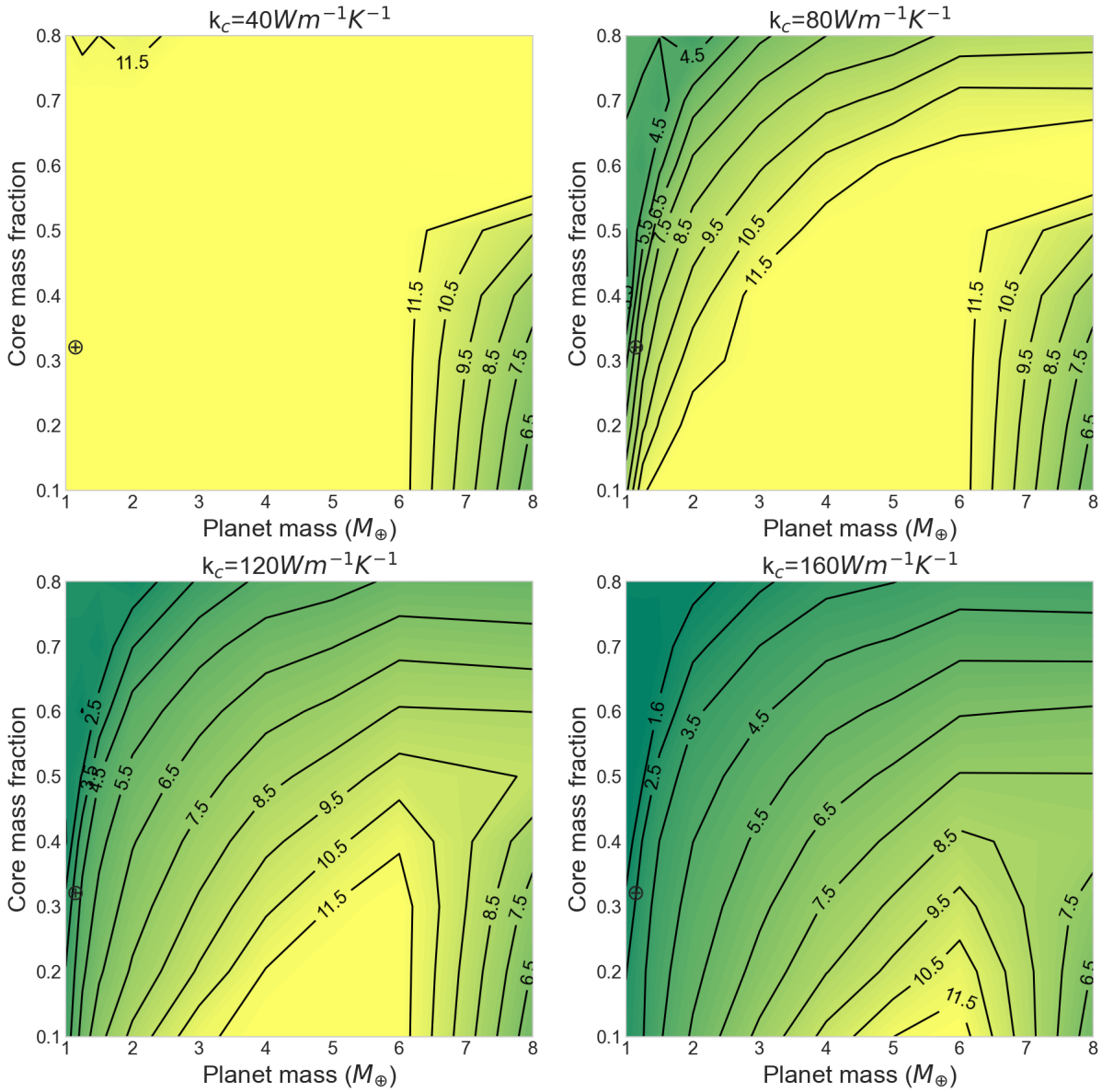

Figure 4.2.1: Maps of lifetime of dynamo in the liquid cores of planets with various $M_{\rm pl}$ and CMFs in Gyr. We assume thermal convection as the only driver to maintain dynamo in the liquid core. Each sub-panel shows dynamo lifetime calculated with various k_c (40, 80, 120, and 160 $\mathrm{Wm^{-1}K^{-1}}$). Contour lines indicate dynamo lifetime in Gyr. Earth-like cases are represented by $\oplus$. The predicted dynamo lifetimes for an Earth-like case are over 12 Gyr, $\sim$5 Gyr, $\sim$3 Gyr and $\sim$1.6 Gyr, with k_c =40, 80, 120 and 160 $\mathrm{Wm^{-1}K^{-1}}$, respectively.

and reduces Re_m. The difference between the lifetimes of the dynamo and of the thermal convection in the liquid core is small. For example, for a $8M_\oplus$ planet with a CMF of 0.3, the lifetime of the dynamo is 6.97 Gyr for all k_c considered in our model, while the liquid convecting core lasts for 7.00 Gyr, a 0.4% difference.

The lifetime of the dynamo increases as $M_{\rm pl}$ increases and CMF decreases, and starts decreasing after $M_{\rm pl}$ reaches $\sim 6M_\oplus$ and CMF reaches ~ 0.5, as shown in figure 4.2.1. The planet with $M_{\rm pl} = 6M_\oplus$ and CMF=0.1 has the longest dynamo lifetime out of all simulated planets, over 12 Gyr for all 4 choices of k_c. This trend is due to how three quantities vary as a function of $M_{\rm pl}$ and CMF: the core heat loss rate ($F_{\rm CMB}$), the conductive heat flux along the core adiabat ($F_{\rm cond}$) and the lifetime of the liquid core.

The core heat loss rate is greater for more massive planets with the same CMF, as shown in Figure 4.2.2. $F_{\rm CMB}$ at 12 Gyr, $F_{\rm CMB,12Gyr}$, increases from $\sim 0.032{\rm Wm}^{-2}$ for a $1M_\oplus$ planet with CMF=0.3 to $\sim 0.14{\rm Wm}^{-2}$ for a $6M_\oplus$ planet with the same CMF. For this choice of CMF, $F_{\rm CMB,12Gyr}$ can be described by a power-law scaling relation,

$$F_{\rm CMB,12Gyr}(M_{pl}) = F_{\rm CMB,12Gyr}(M_\oplus)\left(\frac{M_{pl}}{M_\oplus}\right)^{0.75}. \tag{4.1}$$

Similarly, $F_{\rm cond}$ at 12 Gyr, $F_{\rm cond,12Gyr}$, can be described by the same scaling relation with a power-law exponent of 0.23. The power-law exponent for $F_{\rm CMB}$ is over three times as large as that for $F_{\rm cond}$, indicating that more massive planets are likely to have longer lasting dynamos sustained by thermal convection in the liquid core, so long as the core does not fully solidify when thermal convection shuts off. As Figure 4.2.2(b) shows, with $k_c = 80{\rm Wm}^{-1}{\rm K}^{-1}$, the core dynamo sustained solely by thermal convection is still operating for planets with $M_{pl} = 3 - 6M_\oplus$ and CMF=0.3 at t=12 Gyr, while the dynamo in the core no longer exists for 1 and $2M_\oplus$ planets with the same CMF.

The varying level of $F_{\rm CMB}$ is a consequence of the thermal blanketing effect of the mantle, namely how much heat can be transported through the lower thermal boundary layer in the

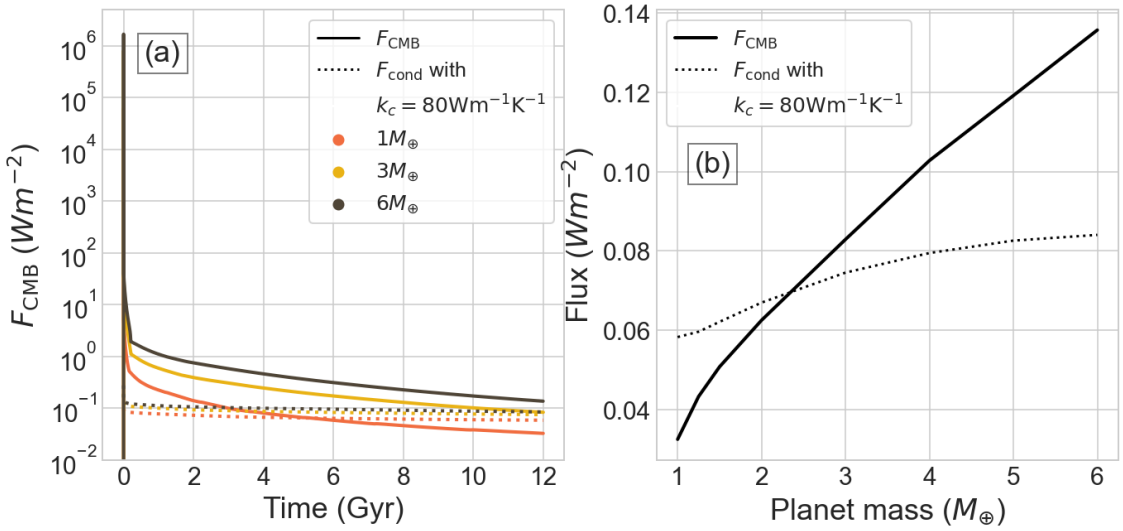

Figure 4.2.2: Left: time evolution of heat flux at CMB, $F_{\rm CMB}$, for planets with $M_{\rm pl} = 1M_\oplus$ (orange), $3M_\oplus$ (light brown) and $6M_\oplus$ (dark brown), and CMF=0.3. Dashed curves are the conductive heat flux along the core adiabat calculated with $k_c = 80 {\rm Wm}^{-1}{\rm K}^{-1}$, which is the threshold flux for the liquid core to be convecting. Right: $F_{\rm CMB}$ (solid curve) and $F_{\rm cond}$ (dotted curve) at 12 Gyr for planets with various masses and CMF of 0.3.

mantle. Using equation 2.51, we can rewrite $F_{\rm CMB}$ as

$$F_{\rm CMB} = -k \left.\frac{dT}{dr}\right|_{LM} \sim \Delta T_{\rm BL}^{\frac{4}{3}} (k\rho)^{\frac{2}{3}} (c_P \alpha g)^{\frac{1}{3}} ({\rm Ra_c}\eta)^{-\frac{1}{3}}, \tag{4.2}$$

where k, ρ, c_P, α, g and η are the thermal conductivity, density, specific heat, thermal expansion coefficient, gravitational acceleration and viscosity in the thermal boundary in the lower mantle, $\Delta T_{\rm BL}$ and ${\rm Ra_c} = 660$ is the critical Rayleigh number. We use a modified mixing length theory to model mantle convection, which does not explicitly calculate the thickness of the thermal boundary layer. Instead, our model computes radial profiles of conductive and convective heat flow in the mantle. We define the thermal boundary layer in the lower mantle as the region above the CMB where heat transport is dominated by conductive heat flow. $\Delta T_{\rm BL}$ is the temperature decrease across the thermal boundary layer in the lower mantle. ρ, α, g and η are mass averaged values in the thermal boundary layer

in the lower mantle. We consider a constant k and c_P for the lower mantle, 10 $\mathrm{Wm^{-1}K^{-1}}$ and 1265 $\mathrm{JK^{-1}kg^{-1}}$ respectively. Following the analysis in Blaske and O'Rourke [2021], we assume the dependence of ρ, α, g, η and ΔT_{BL} on planet mass obeys the power-law with a form $X_i(M_{pl})/X_i(M_\oplus) = (M_{pl}/M_\oplus)^{x_i}$, where x_i is the power-law exponent for the quantity X_i. Combining all power-law exponents, we have

$$F_{\mathrm{CMB}}(M_{pl}) \propto \left(\frac{M_{pl}}{M_\oplus}\right)^{\frac{4}{3}x_{\Delta \mathrm{T_{BL}}}+\frac{2}{3}x_\rho+\frac{1}{3}(x_\alpha+x_g-x_\eta)} \tag{4.3}$$

We fit the power-law relation to quantities for 1-6$M_\oplus$ planets with a CMF=0.3 at 12 Gyr. The results are summarized in figure 4.2.3. We remind that we exclude 7 and 8$M_\oplus$ planets in this analysis, as the cores of these planets fully solidify at ∼8.8 Gyr and ∼7.0 Gyr. Summing all power-law exponents in equation 4.3, we recover the power-law exponent for $\mathrm{F_{CMB,12Gyr}}$ in equation 4.1, 0.75. In particular, $\Delta \mathrm{T_{BL}}$ with a power-law exponent of 0.56 contributes the most to the increasing $\mathrm{F_{CMB}}$ as M_{pl} grows. Indeed, the difference between the average mantle and average core temperatures at 12 Gyr increases from ∼2200 K to ∼6300 K as M_{pl} increases from 1 to 6$M_\oplus$.

Given the same planet mass, the core heat loss rate remains comparable for planets with various CMFs. For example, $\mathrm{F_{CMB,12Gyr}}$ are between 0.07$\mathrm{Wm^{-2}}$ and 0.085$\mathrm{Wm^{-2}}$ for 3$M_\oplus$ planets with all CMFs considered in the simulations, as shown in Figure 4.2.4. At the same time, $\mathrm{F_{cond}}$ grows threefold as CMF increases from 0.1 to 0.8. This is caused by the steeper adiabatic temperature gradient at lower $\mathrm{P_{CMB}}$ of planets with smaller CMFs. As the threshold flux for maintaining thermal convection and dynamo in the liquid core increases with increasing CMFs, the lifetime of the dynamo decreases. As indicated by Figure 4.2.4, with $k_c = 80\mathrm{Wm^{-1}K^{-1}}$, the core dynamo driven by thermal convection alone still operates at 12 Gyr for 3$M_\oplus$ planets with CMFs between 0.1 and 0.4, but not for planets with the same mass and CMFs between 0.5 and 0.8.

Dependence of $\mathrm{F_{CMB}}$ on CMF, similar to that on M_{pl}, is due to the combined effect of

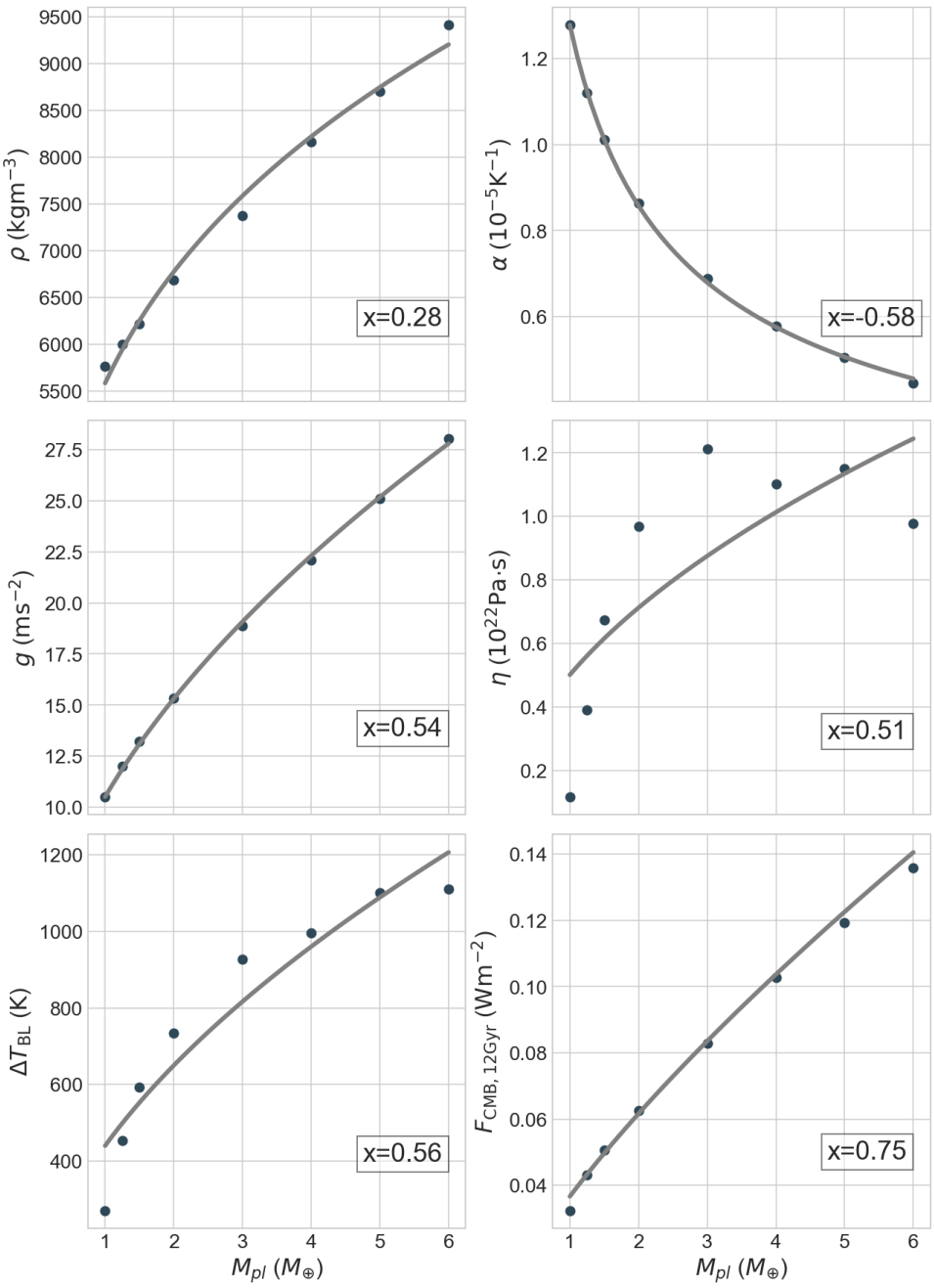

Figure 4.2.3: How density (ρ), thermal expansion coefficient (α), gravitational acceleration (g) and viscosity (η) of the thermal boundary layer in the lower mantle, and the temperature decrease across the thermal boundary layer in the lower mantle ($\Delta \mathrm{T_{BL}}$) and heat flux across CMB $\mathrm{F_{CMB}}$ at 12 Gyr vary as a function of M_{pl}. The dots are values calculated using thermal and structural profiles of planets at 12 Gyr in the simulation. Gray lines show the best fit power-laws for individual quantities. x is the power-law exponent for each quantity.

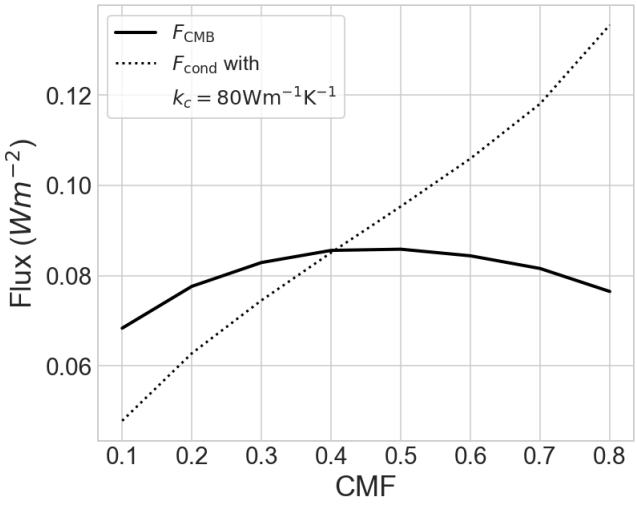

Figure 4.2.4: $F_{\rm CMB}$ (solid curve) and $F_{\rm cond}$ (dotted curve) at 12 Gyr for planets with various CMFs and $M_{pl} = 3M_{\oplus}$.

various thermophysical properties in the thermal boundary layer in the lower mantle. We assume the dependence of ρ, α, g, η and $\Delta_{\rm BL}$ on $\rm P_{CMB}$ follows a power-law relation,

$$F_{\rm CMB}(P_{\rm CMB}) \propto \left(\frac{P_{\rm CMB}}{P_{\rm CMB,CMF=0.8}}\right)^{\frac{4}{3}x_{\Delta \rm T_{BL}}+\frac{2}{3}x_{\rho}+\frac{1}{3}(x_{\alpha}+x_{g}-x_{\eta})}, \tag{4.4}$$

where $P_{\rm CMB,CMF=0.8}$ is the pressure level at the CMB for a $3M_{\oplus}$ planet with CMF=0.8. We choose $P_{\rm CMB,CMF=0.8}$ as the reference pressure because the planet with CMF=0.8 has the lowest pressure at its CMB among all $3M_{\oplus}$ planets, and $P_{\rm CMB}$ of planets with the same M_{pl} increases with decreasing CMF. The fitting results for all five quantities and $F_{\rm CMB}$ are summarized in Figure 4.2.5. $\Delta \rm T_{BL}$ and ρ are two terms that contribute to increasing the Rayleigh number (Ra) in the lower mantle as $P_{\rm CMB}$ increases, thus resulting in more vigorous mantle convection. However, their contribution to a more vigorous mantle convection is cancelled by the increasing in η and the decreasing in g and α as $P_{\rm CMB}$ increases. Thus $F_{\rm CMB}$ can remain relatively comparable among all CMFs considered in the simulations. We remind readers that the power-law fit to $\rm F_{CMB}$ is not a perfect fit, as the simple relation

does not fully capture the complex nature of mantle heat transport. Instead, the relation highlights the weak dependence of $\mathrm{F_{CMB}}$ on $\mathrm{P_{CMB}}$ and CMF.

Lastly, the lifetime of the dynamo in the liquid core is limited by the lifetime of the liquid core for massive planets ($M_{pl} > 6M_{\oplus}$) with smaller cores (CMF $\lesssim 0.5$). The short lifetimes of liquid cores of these planets are the result of a high level of $\mathrm{F_{CMB}}$ and a low core mass. As explained above in the section, F_{CMB} increases with growing planet mass. As a result, the solid inner core is able to grow faster in a more massive planet than in a less massive one. For $R_{\mathrm{ic}}/R_{\mathrm{c}}$ to grow to 0.5, it takes a $1M_{\oplus}$ planet with CMF=0.3 ∼6.5 Gyr and only ∼2 Gyr an $8M_{\oplus}$ planet with the same CMF. Further, the thermal energy needs to be lost by the core for it to fully solidify is more achievable for planets with smaller CMFs. In our simulations, the cores of $8M_{\oplus}$ planets with CMFs between 0.1 and 0.5 fully solidify within 12 Gyr and the drop in average core temperatures are all around 19000K. The decreases in average core temperature from $t = 0$ to when the core fully solidifies are comparable for planets with the same mass and various CMFs. However, by simply having a less massive core, the core in the case with CMF=0.1 becomes fully solid in ∼5.5 Gyr, while it takes the core in the case with CMF=0.5 ∼9.5 Gyr.

In addition to F_{CMB}, F_{cond} and the lifetime of liquid core, the thermal and magnetic history of rocky planets are subject to the thermal conductivity of mantle and core. In our simulations, we assume a constant thermal conductivity in the lower mantle, $k_{\mathrm{LM}} = 10\mathrm{Wm^{-1}K^{-1}}$, and 4 choices of thermal conductivity in the liquid core, k_c =40, 80, 120 and 160 $\mathrm{Wm^{-1}K^{-1}}$. With an increasing level of k_c, the threshold flux for maintaining a dynamo driven by thermal convection increases and results in a decrease in predicted lifetime of the dynamo in the liquid core. For an Earth-like case ($M_{pl} = 1M_{\oplus}$ and CMF=0.33), the predicted lifetime of the dynamo is over 12 Gyr, ∼5 Gyr, ∼2.5 Gyr and ∼1.6 Gyr, with k_c =40, 80, 120 and 160 $\mathrm{Wm^{-1}K^{-1}}$.

However, it has been proposed that the thermal conductivity of mantle silicate and

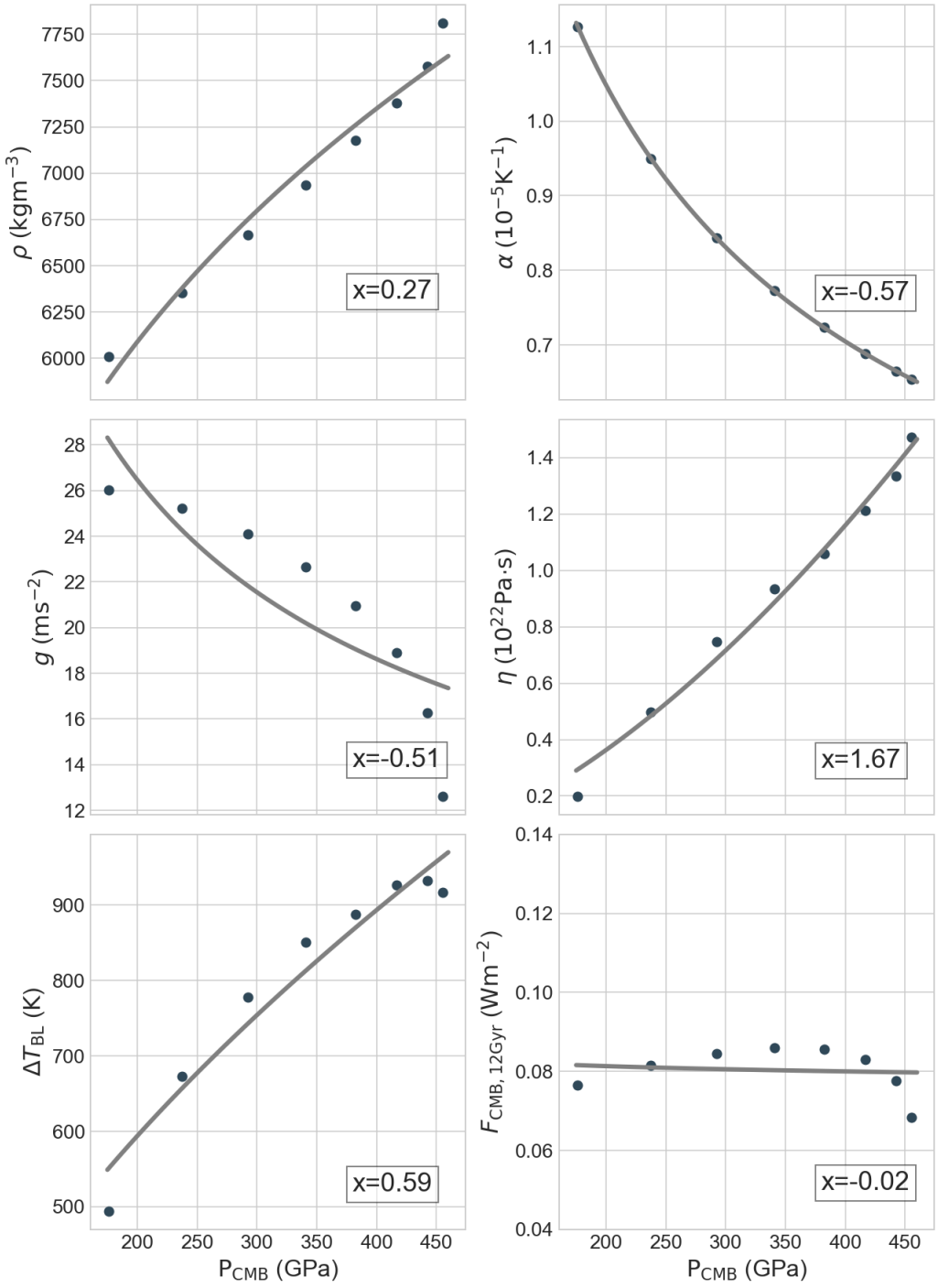

Figure 4.2.5: Same as Figure 4.2.3, except quantities are shown with respect to P_{CMB} of $3M_{\oplus}$ planets with CMFs between 0.1 and 0.8. P_{CMB} decreases with an increasing CMF for planets with the same M_{pl}.

liquid iron could increase for massive rocky planets due to the increase in the temperature and pressure levels [Stamenković et al., 2011]. On one hand, an increase in $k_{\rm LM}$ in massive rocky planets indicates a greater $F_{\rm CMB}$ than predicted in our simulations, and thus possibly lengthening the lifetime of the dynamo. On the other hand, an increase in k_c in massive rocky planets indicates that threshold flux for maintaining thermal convection and dynamo is greater than that of less massive planets. Inclusion of a thermal conductivity consistent with temperature and pressure levels for both the mantle and the core is left for a future study.

4.2.2 The lifetime of the dynamo driven by both thermal and compositional convection

In this section, we explore the effect of including compositional convection on the predicted lifetime of dynamo in the liquid core of rocky planets. Compositional convection is produced by light material released at the inner-core boundary. In our simulations, we consider 10% Si by mass as a proxy for light material in the core. We assume all Si partitions into the liquid outer core as the inner core solidifies. The lower density of light material compared to iron provides a buoyancy force that drives compositional convection in the liquid outer core in rocky planets. To evaluate the lifetime of the dynamo driven by both thermal and compositional convection, we calculate thermal and chemical buoyancy flux and the sum of two fluxes needs to stay positive for the dynamo in the liquid core to be active.

Including compositional convection could alter the magnetic history of a planet in various ways. Figure 4.2.6 shows the evolution of buoyancy fluxes in the liquid core of 1, 2, 5 and $8M_\oplus$ planets with CMF=0.4 and $k_c = 80 \mathrm{Wm}^{-1}\mathrm{K}^{-1}$, and the results indicate when the dynamo is active for individual planets, with or without the contribution of composition convection. For an $1M_\oplus$ planet, thermal convection in the liquid core shuts off after ∼2.5 Gyr and the liquid core becomes thermally stratified ($F_T < 0$). The core starts solidifying at ∼4 Gyr and

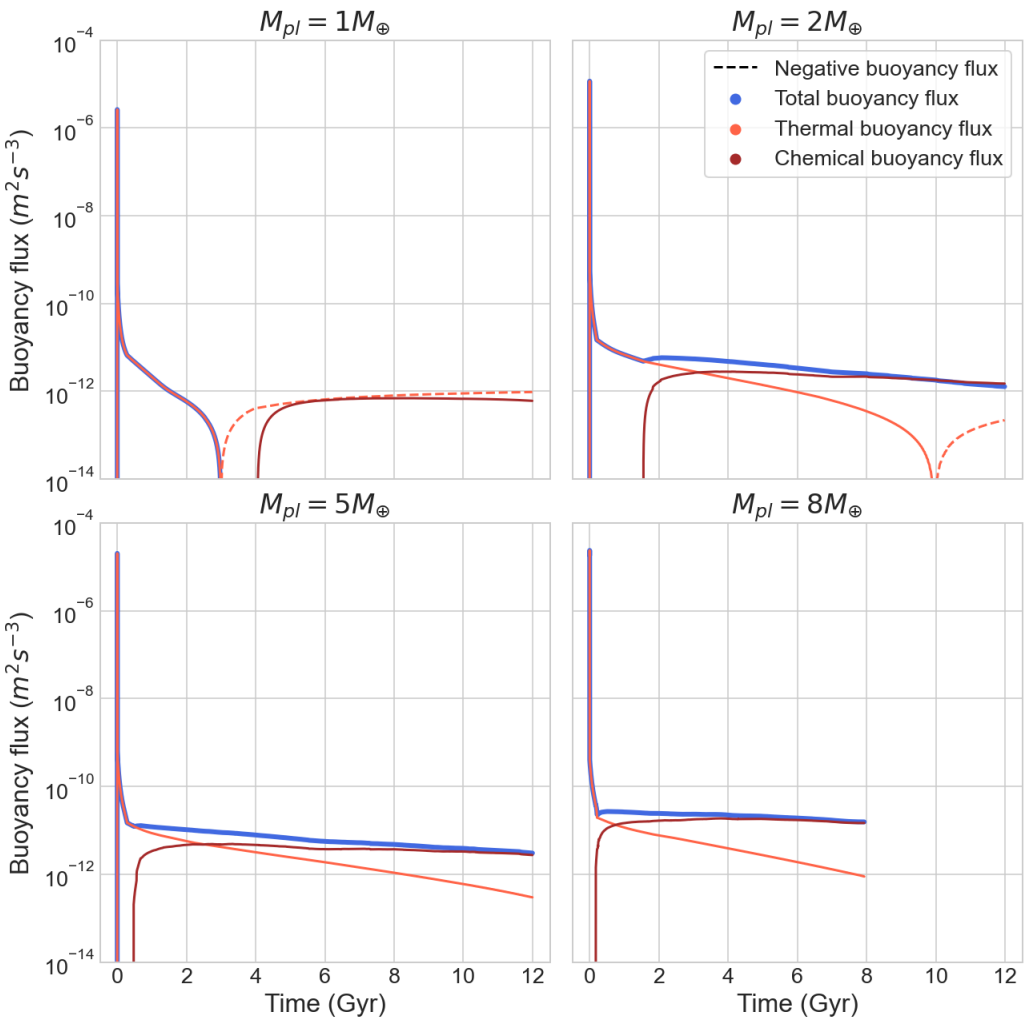

Figure 4.2.6: Evolution of thermal (red curves), chemical (brown curves) and total (blue curves) buoyancy fluxes for 1, 2, 5 and $8M_\oplus$ planets with CMF=0.4 and $k_c = 80$ $\mathrm{Wm^{-1}K^{-1}}$. Dashed curves indicate negative thermal buoyancy fluxes, which chemical buoyancy fluxes need to overcome to sustain dynamos in liquid cores. The evolution ends at 8 Gyr in the case of $8M_\oplus$ planet when the core fully solidifies.

F_x becomes positive. However, F_x is not able to overcome the thermal stratification in the liquid core due to the low F_T, and thus does not lengthen the lifetime of the dynamo in this case. For the case with $M_{pl} = 2M_\oplus$, F_x starts contributing to sustaining the dynamo at $\sim$1.8 Gyr and F_b stay positive for the entire simulation of 12 Gyr. Thermal convection shuts off at $\sim$10 Gyr and the dynamo is driven by composition convection alone from $t = 10$ Gyr to 12 Gyr. For 5 and $8M_\oplus$ planets, the inner cores start solidifying at $\sim$0.5 Gyr and $\sim$0.2 Gyr respectively. Both F_T and F_x of the two planets stay positive for the remainder of the evolution, indicating the core dynamo of these two planets are driven by both thermal and compositional convection. For the $5M_\oplus$ planet, a simulation of a longer time period than 12 Gyr is required to test if compositional convection may lengthen the lifetime of the dynamo. For the $8M_\oplus$ planet, the core fully solidifies at $\sim$8 Gyr, and as a result the lifetime of the dynamo remains the same with or without considering compositional convection.

Compositional convection lengthens the lifetime of the dynamo in the liquid core, so long as the total buoyancy flux ($F_b = F_T + F_x$) is positive and the liquid core still exists by the time F_b reduces to 0. Out of our simulations, a $6M_\oplus$ planet with CMF=0.1 has the greatest dynamo lifetime, exceeding 12 Gyr for all k_c considered. The dynamo lifetime for an Earth-like case ($M_{pl} = 1M_\oplus$ and CMF=0.33) is over 12 Gyr for k_c =40 and 80Wm^{-1}K^{-1}, and $\sim$6 Gyr for $k_c = 80\mathrm{Wm}^{-1}\mathrm{K}^{-1}$. When $k_c = 160\mathrm{Wm}^{-1}\mathrm{K}^{-1}$, the dynamo lifetime for the Earth-like case is only $\sim$1.8 Gyr, indicating that an additional amount of radiogenic heating in the liquid core might be required for an active dynamo at current time.

How the lifetime of the dynamo driven by both thermal and compositional convection scales with M_{pl} and CMF is similar to that of the dynamo driven by thermal convection alone. The lifetime of the dynamo increases as M_{pl} increases and CMF decreases, and starts decreasing after M_{pl} reaches $\sim 6M_\oplus$ and CMF reaches $\sim$ 0.5. The determining factor is how fast the core loses heat, i.e. F_{CMB}. A high F_{CMB} indicates a fast growing inner core and thus resulting in a high F_x (equation 2.57). Given the same CMF, an increase in planet

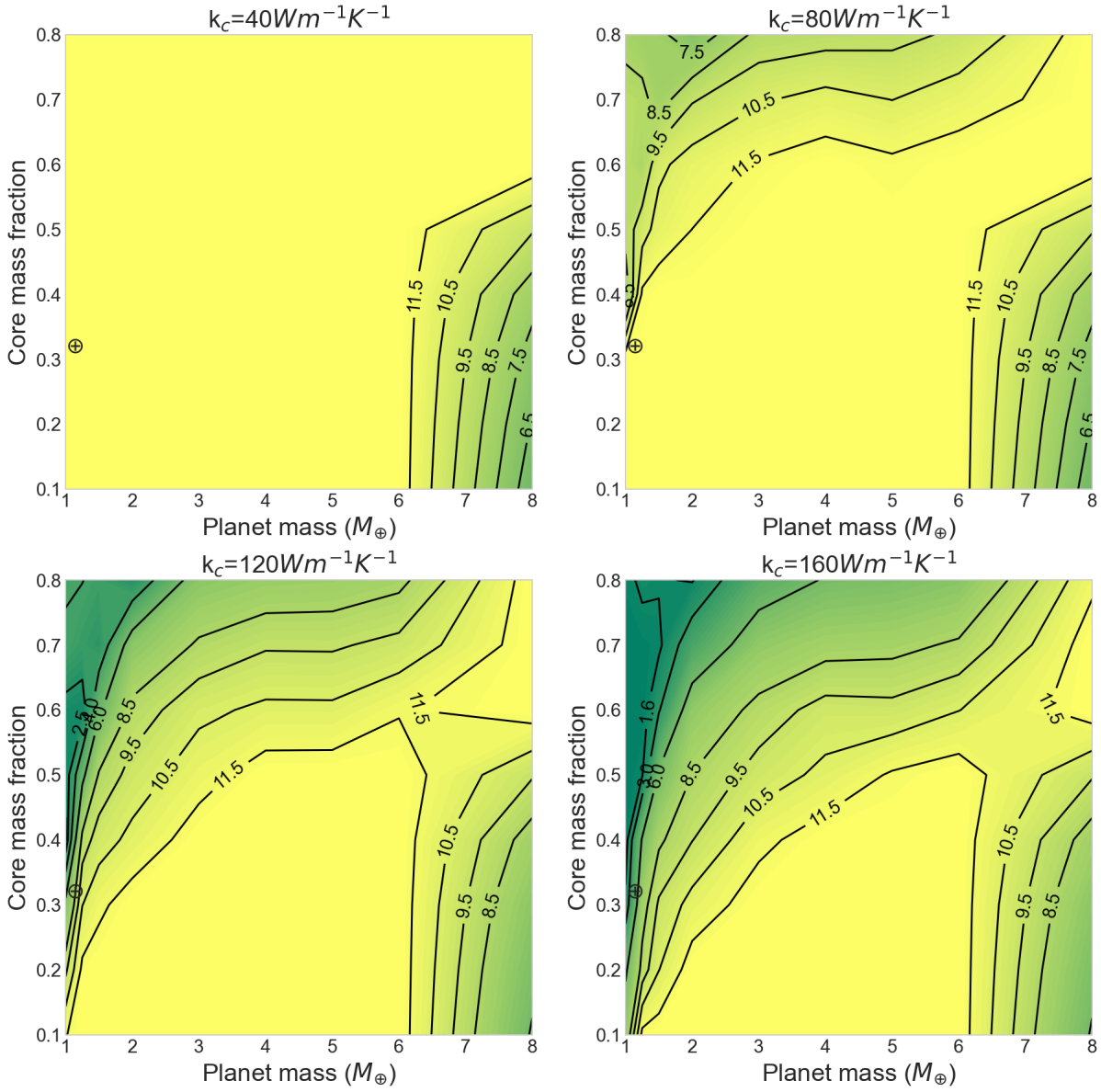

Figure 4.2.7: Same as figure 4.2.1, except that the dynamo is driven by both thermal and compositional convection.

mass leads to a greater $F_{\rm CMB}$ (as explained in section 4.2.1) and thus a higher F_x. For example, with CMF=0.4, $F_{\rm CMB}$ at 5 Gyr increases from ∼0.06 $\rm Wm^{-2}$ to ∼0.45 $\rm Wm^{-2}$ as M_{pl} increases from 1 to $8M_\oplus$, and F_x at the same time increases from $4.77 \times 10^{-13}\rm m^2s^{-3}$ to $1.82 \times 10^{-11}\rm m^2s^{-3}$. In addition, $F_{\rm conv} = F_{\rm CMB} - F_{\rm cond}$ grows with increasing M_{pl} and decreasing CMF, leading to two possible scenarios. In one scenario, F_T eventually becomes negative and it is more attainable for F_x to overcome the negative thermal buoyancy flux in a more massive planet with a smaller CMF. Therefore, dynamo driven by both thermal and compositional convection in the liquid cores of massive planets with small CMFs could last longer. In the other scenario, for the most massive planets with smaller CMFs out of our simulations ($M_{pl} > 6M_\oplus$ and CMF$\lesssim$ 0.5), the core fully solidifies before F_T could become negative. Thus, the dynamo lifetime is limited by the age of the liquid core.

4.3 Impact of mantle viscosity on the lifetime of the dynamo in the liquid core

In this section, we present results of the same grid of planets as in section 4.2 calculated with a different model of viscosity of post-perovskite. The lifetimes of the dynamo driven by thermal convection alone and both thermal and compositional convection are summarized in Figures 4.3.1 and 4.3.2.

Compared to the fiducial case (Figures 4.2.1 and 4.2.7), the dynamo lifetime shown in Figures 4.3.1 and 4.3.2 exhibits a different dependence on planet mass. Applying the upper-bound rheology for ppv in the evolution calculation, we find that the $3M_\oplus$ planet with CMF=0.1 has the longest predicted lifetime of the dynamo driven by thermal convection, ∼8.5 Gyr, ∼8.4 Gyr and ∼6.3 Gyr with k_c =80, 120 and 160$\rm Wm^{-1}K^{-1}$, instead of the $6M_\oplus$ planet with CMF=0.1 using the lower-bound rheology for ppv. When $k_c = 40\rm Wm^{-1}K^{-1}$, the $2M_\oplus$ planet with CMF=0.1 has the longest predicted dynamo lifetime (over 12 Gyr), as the dynamo lifetime of the $3M_\oplus$ planet with CMF=0.1 is ∼8.5 Gyr, limited by the lifetime of

the liquid core. For cases with CMF=0.3, $k_c = 120\mathrm{Wm}^{-1}\mathrm{K}^{-1}$ and the upper-bound rheology for ppv, the lifetime of the dynamo driven by thermal convection increases from ∼1.8 Gyr with $M_{pl} = 1M_\oplus$ to ∼6.2 Gyr with $M_{pl} = 3M_\oplus$. The dynamo lifetime then decreases to ∼0.6 Gyr as M_{pl} increases to $8M_\oplus$. Including compositional convection as an additional driver for the dynamo, the predicted dynamo lifetime for cases with the same CMF, k_c and the model for viscosity of ppv could reach ∼1.9 Gyr and ∼12 Gyr with $M_{pl} = 1M_\oplus$ and $3M_\oplus$. The dynamo lifetimes for planets with masses greater than $3M_\oplus$ remain the same with the addition of compositional convection as the core fully solidifies before thermal convection shuts off.

The difference in the predicted dynamo lifetime between the fiducial case and the case presented in this section lies in how viscosities of ppv with upper- and lower-bound rheologies depend on temperature and pressure. The contour maps shown in Figure 4.3.3 show the viscosity of ppv with two rheologies. The dashed curve indicates temperature and pressure levels where two rheologies lead to the same viscosity for ppv. The regions above and below the curve are temperature and pressure levels where the lower-bound rheology (the fiducial choice) leads to a higher and lower viscosity for ppv than the lower-bound rheology. For example, the mantle temperature profile of the $1M_\oplus$ planet with CMF=0.3 is in the lower region in the viscosity map, and the viscosity at the base of the mantle predicted by the lower-bound rheology is ∼1 order of magnitude lower than that by the upper-bound rheology. As a result, the case with the lower-bound rheology for ppv has a higher F_{CMB} than the case with the upper-bound rheology ($\sim 0.22\mathrm{Wm}^{-2}$ vs $\sim 0.18\mathrm{Wm}^{-2}$ at 1 Gyr), which leads to a longer predicted dynamo lifetime. The lifetimes of the dynamo driven by thermal convection predicted using the lower- and upper-bound rheologies for ppv for this planet are ∼5.4 Gyr and ∼3.0 Gyr. However, for a $5M_\oplus$ planet with CMF=0.3, the temperature and pressure levels in the lower thermal boundary layer in the mantle are in the upper region of the contour map. The lower-bound rheology for ppv predicts a viscosity that is ∼2 orders of

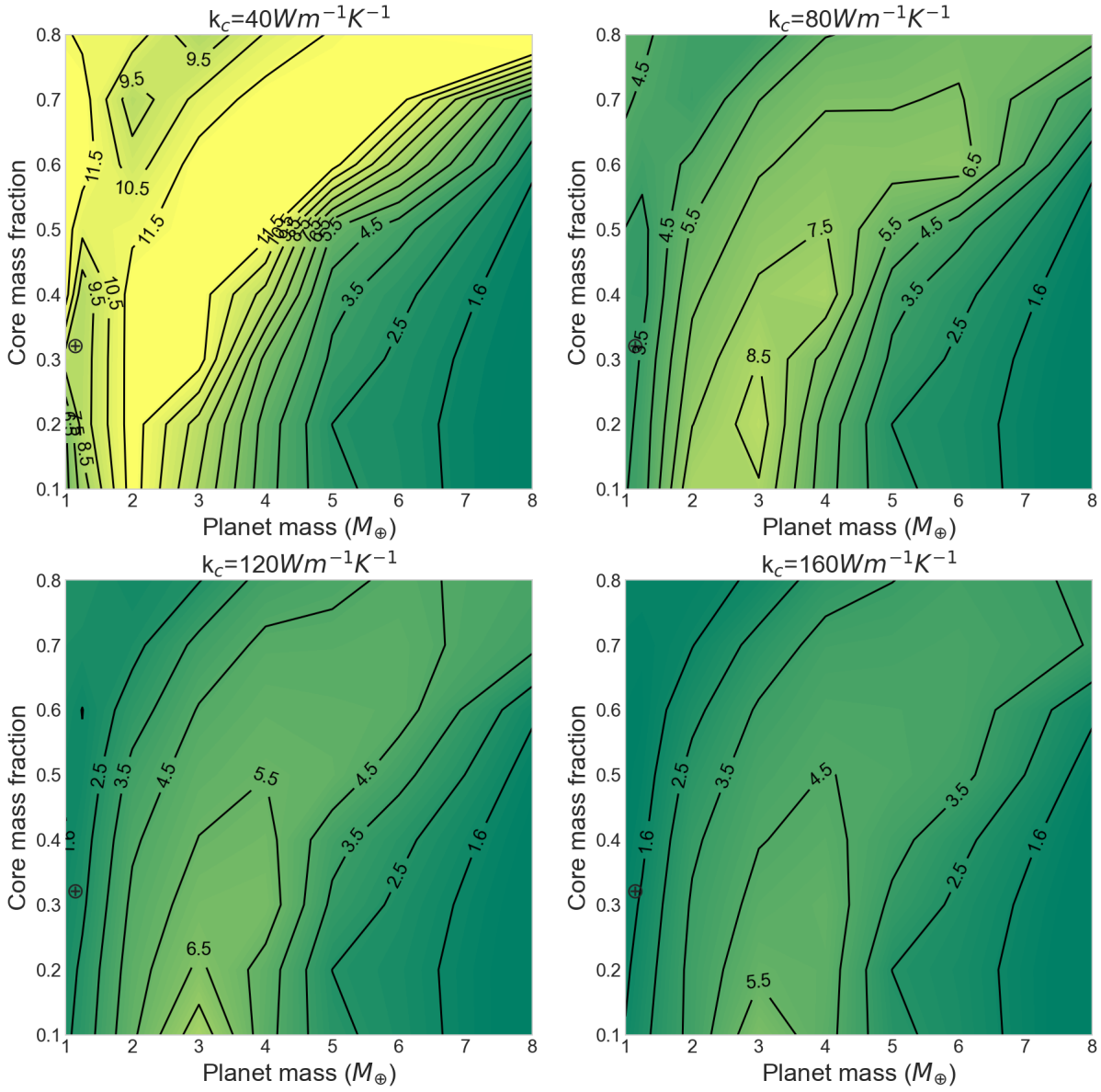

Figure 4.3.1: Same as figure 4.2.1, except that we consider the lower-bound rheology for the viscosity of post-perovskite [Tackley et al., 2013].

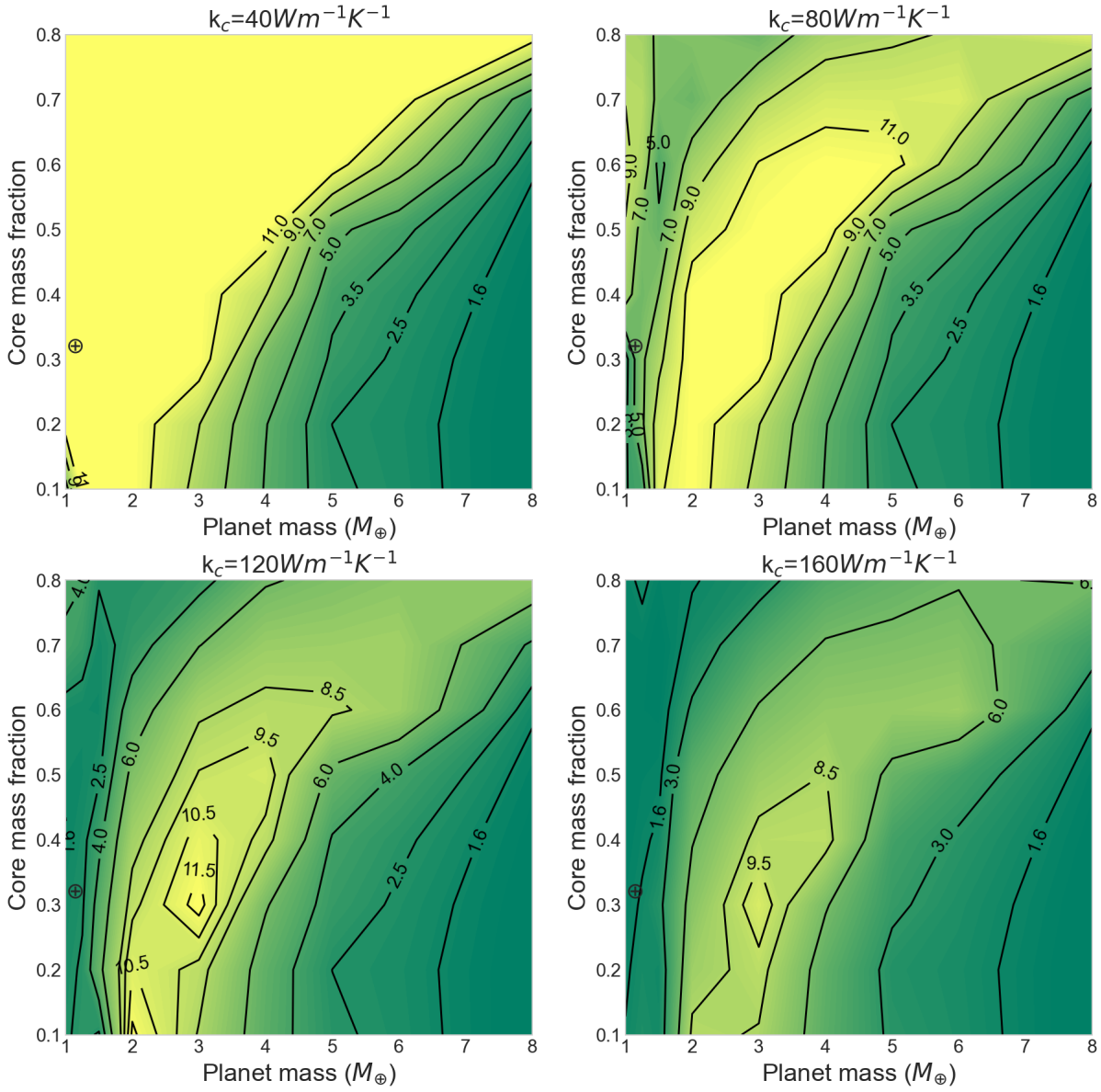

Figure 4.3.2: Same as figure 4.2.1, except that the dynamo is driven by both thermal and compositional convection.

magnitude higher than the upper-bound rheology. For this planet, the case with the upper-bound rheology for ppv has a higher F_{CMB} than the case with the lower-bound rheology ($\sim 1.87\mathrm{Wm}^{-2}$ vs $\sim 0.88\mathrm{Wm}^{-2}$ at 1 Gyr). F_{CMB} for the case with the upper-bound rheology is high enough such that the core fully solidifies in ∼3.28 Gyr, which shuts off the dynamo. In contrast, the liquid core could persist for over 12 Gyr in the case with the lower-bound rheology.

4.4 Impact of radiogenic heating in the core

Radiogenic heating in the core provides extra energy for magnetic field generation, in addition to the leftover energy from planet formation as well as latent heat and gravitational energy release due to inner core growth. Radiogenic heating could decrease the rate at which the core temperature decreases, thus extend the time period for which the CMB heat flux stays above the threshold heat flux for maintaining thermal convection and core dynamo. The exact effect of radiogenic heating in the core on the thermal and magnetic history of rocky planets depend on how much radiogenic elements can partition into the metallic core during planet formation.

The exact amount of radiogenic heating in the core of Earth remains unclear. For K, experimental studies and ab initio calculations suggest that its concentration in Earth's core could be between 25 ppm and several hundred ppm [Gessmann and Wood, 2002, Murthy et al., 2003, Hirao et al., 2006, Watanabe et al., 2014, Blanchard et al., 2017, Xiong et al., 2018]. In the fiducial case, we consider ∼140 ppm of K in the core of rocky planets. This value is motivated by the Earth-like case presented in Chapter 3, which requires ∼140 ppm of K in its core to match the present inner core size and maintain dynamo action with $k_c = 80\mathrm{Wm}^{-1}\mathrm{K}^{-1}$. To quantify the effect of radiogenic heating in the core on the thermal and magnetic history of rocky exoplanets, we compute the thermal history of the same grid of rocky planets as presented in section 4.2 with zero radiogenic heating in the core and

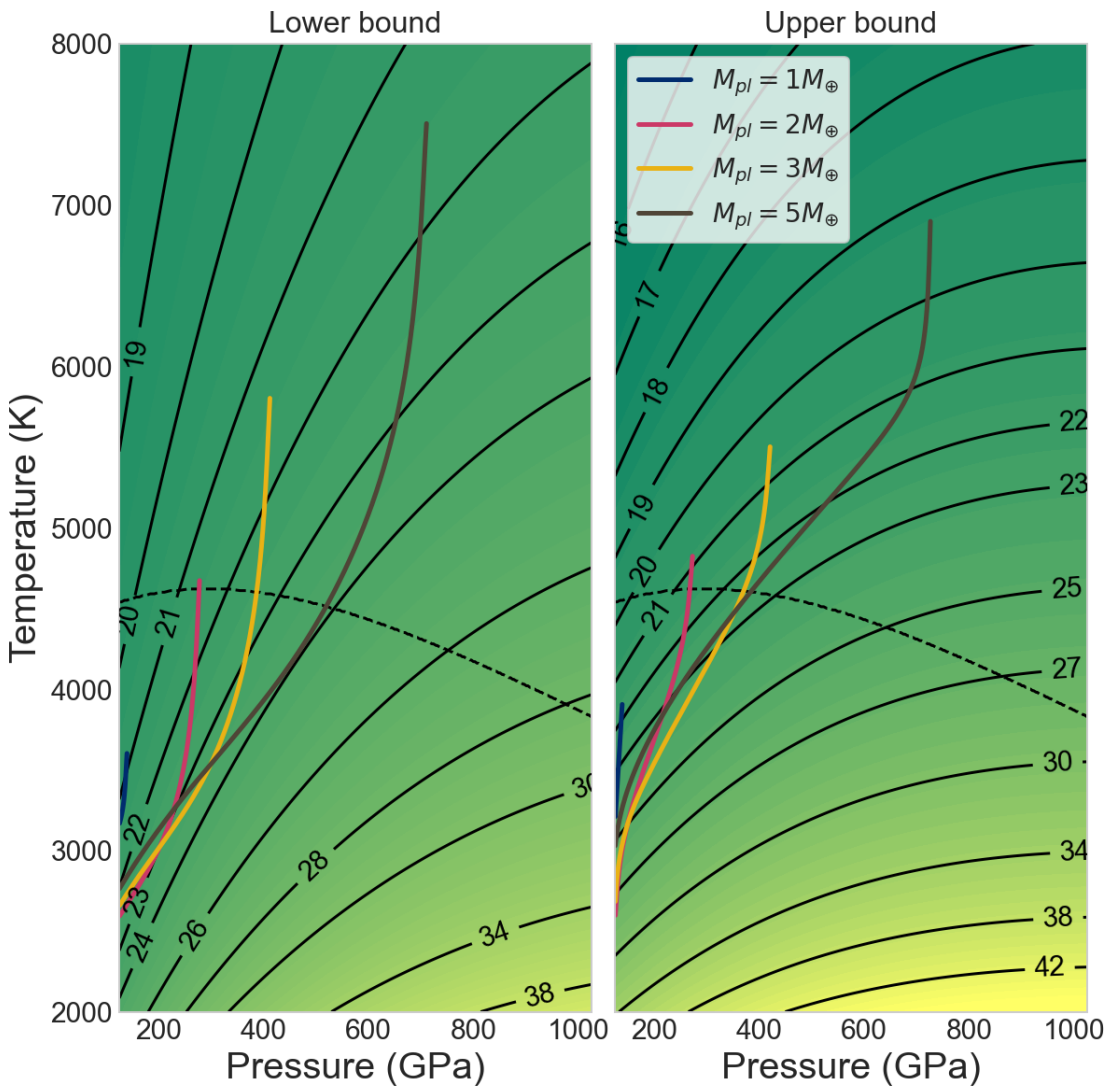

Figure 4.3.3: Viscosity of post-perovskite (ppv) in Pa s calculated based on upper- and lower-bound rheology of ppv [Tackley et al., 2013]. Contour lines indicate the log base 10 of viscosity in Pa s. Dashed curve indicates temperature and pressure levels where both rheologies produce the same viscosity for ppv. Regions below and above the dashed curve indicate temperature and pressure levels where the lower-bound rheology produces lower and higher viscosity respectively than the upper-bound rheology does. Dark blue, pink, yellow and brown curves are the temperature profiles of the mantle in ppv phase at 12 Gyr for 1, 2, 3 and $5M_\oplus$ planets with CMF=0.3.

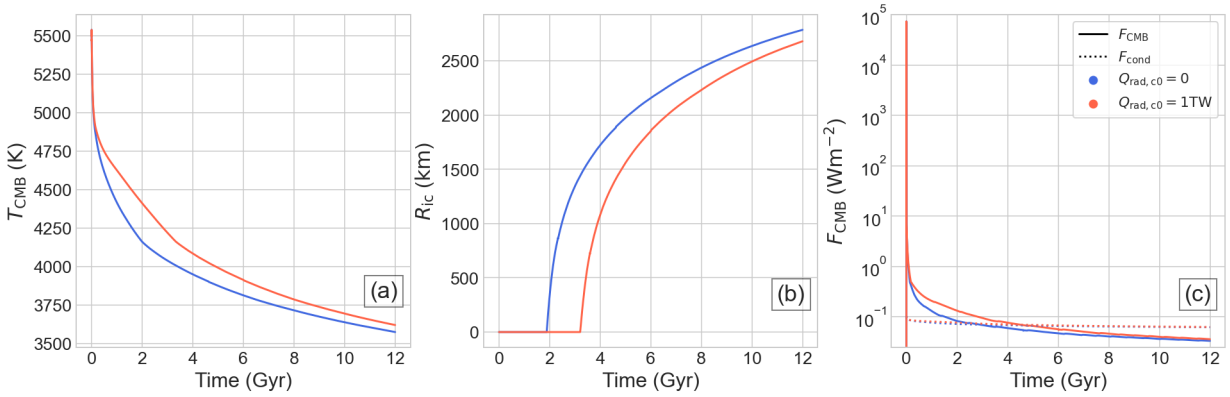

Figure 4.4.1: Time evolution of (a) temperature at the CMB, (b) radius of the solid inner core and (c) heat flux at the CMB for a $1M_{\oplus}$ planet with CMF=0.33 and two levels of radiogenic heating in the core. Red and blue curves represent cases with a current day radiogenic heating of 1 TW (the fiducial choice) and 0 in the core.

compare the results to the fiducial case.

Figures 4.4.1 (a) and (c) show the decline in temperature at the CMB and growth of solid inner core for an Earth-like case ($M_{\rm pl} = 1M_{\oplus}$ and CMF=0.33). Figure 4.4.1 (b) shows the change in $F_{\rm CMB}$ of the same planet. Compared to the fiducial case (red curves in figure 4.4.1), the lack of radiogenic heating in the core leads to an overall cooler core throughout the evolution; at 4.5 Gyr, $T_{\rm CMB}$ is 124 K cooler (3912 K vs 4036 K). The onset of the inner core solidification is earlier by ∼1.33 Gyr compared to the fiducial case, and the predicted inner core radius at 4.5 Gyr is ∼500 km thicker (∼1350 km vs ∼1850 km). With a cooler core in the case with zero core radioactivity, the temperature contrast between the core and the mantle is smaller, which leads to a lower $F_{\rm CMB}$. For example, we predicted $F_{\rm CMB}$ to be ∼0.07 and ∼0.056 Wm^{-2} at 4.5 Gyr for the fiducial case and the case with no radiogenic heating in the core. As a result, the core dynamo shuts off earlier in the case with no radiogenic heating in the core. With a k_c of 80 Wm^{-1}K^{-1}, the dynamo driven by only thermal convection shuts off at ∼4.5 Gyr and ∼2.9 Gyr for the fiducial case and the case with no radiogenic heating in the core. As the rate of radiogenic heat production in the core decays exponentially over time, the difference in the thermal structure of the core

between two cases continues to decrease. The differences in the predicted $T_{\rm CMB}$, $R_{\rm ic}$ and $F_{\rm CMB}$ between two cases reduce to ∼46 K, ∼106 km and ∼0.0027 $\rm Wm^{-2}$.

In addition, we run simulations for $3M_{\oplus}$ planets with various CMFs and two levels of radiogenic heat production rate in the core to illustrate the effect of core radioactivity on the thermal and magnetic history of rocky exoplanets. Results are summarized in Figure 4.4.2. Similar to the Earth-like case described above in this subsection, less and more radiogenic heat production in the core result in lower and higher $F_{\rm CMB}$, larger and smaller solid inner cores, as well as shorter and longer ages of the core dynamo.

Given the same concentration of potassium in the cores of various planets, the total radiogenic heat production in the core increases with increasing CMFs. For example, the rates of radiogenic heat production in the core of $3M_{\oplus}$ planets with CMF=0.1 and 0.8 at 4.5 Gyr are ∼39 TW and ∼309 TW. As a result, the impact of radiogenic heat production in the core on the age of the core dynamo is more prominent for planets with higher CMFs than those with lower CMFs. When $k_c = 120 \rm Wm^{-1}K^{-1}$, the difference in the lifetimes of the core dynamo with two levels of radiogenic heat production in the core increases from ∼0.83 Gyr to ∼1.23 Gyr with CMF increasing from 0.1 to 0.8. The behavior of $F_{\rm CMB}$ as a function of CMF is complicated, because of the competing effect of $Q_{rad,c}$ as an additional power to elevate $F_{\rm CMB}$ and the changes in the core-mantle temperature contrast. The former effect alone tends to elevate $F_{\rm CMB}$ more with increasing CMF. However, a greater level of $Q_{rad,c}$ tend to heat up the mantle more in cases with higher CMFs due to their smaller mantle mass, which would decrease the core-mantle temperature contrast. As shown in the top panel of Figure 4.4.2, the difference in $F_{\rm CMB}$ at 10 Gyr has a maximum at CMF=0.6. The difference in $R_{\rm ic}$ at 10 Gyr is the smallest for the case with CMF=0.8, despite of having the greatest radiogenic heat production in the core, as shown in the middle panel of Figure 4.4.2. This is due to the slope of the melting curve of the core. The melting curve of the core is less steeper for planets with lower CMFs and the same $M_{\rm pl}$ because of a lower pressure level in the cores

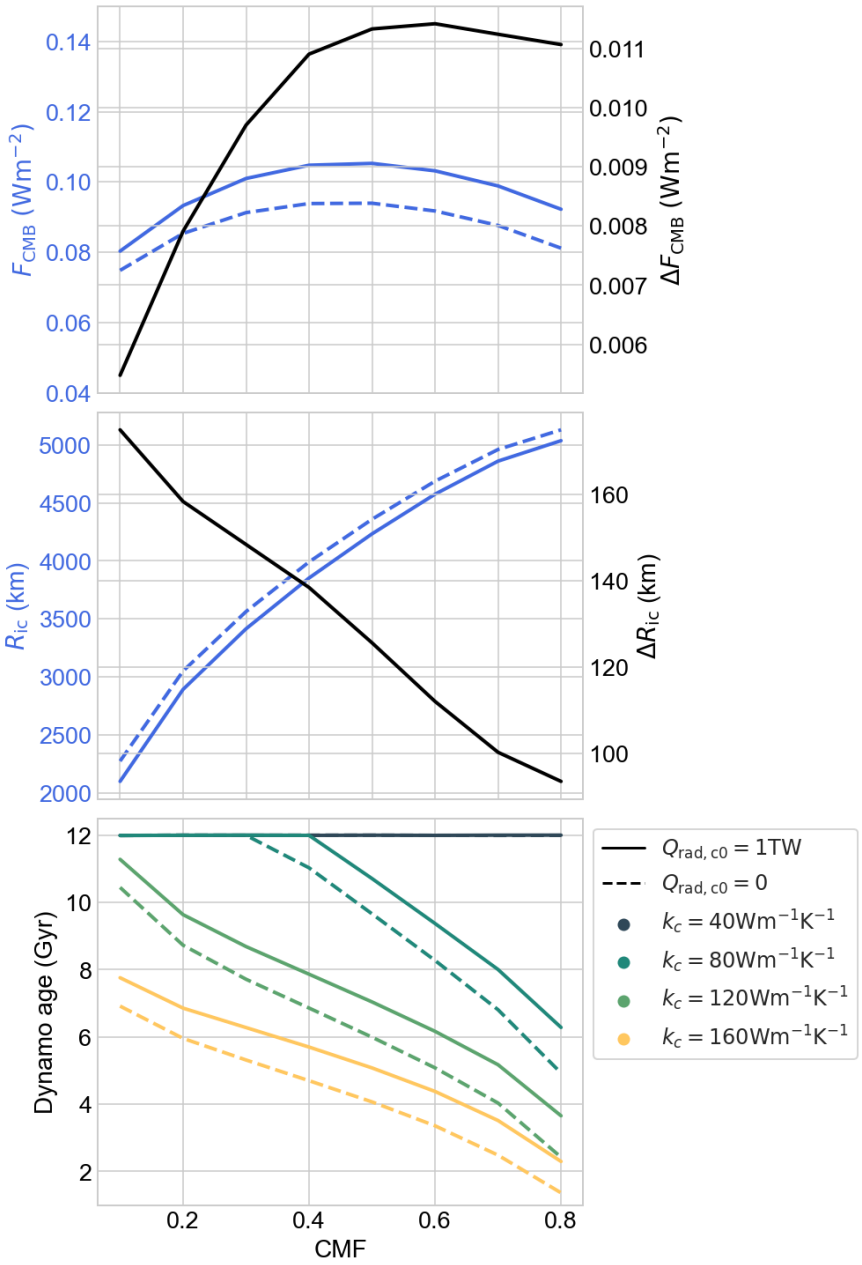

Figure 4.4.2: Thermal and magnetic results for $3M_\oplus$ planets with various CMFs and 2 levels of radiogenic heat production in the core, the fiducial case with ∼140 ppm of potassium and another case with no radiogenic heating in the core. Top panel: $F_{\rm CMB}$ at 10 Gyr. Blue solid and dashed curves represent cases with ∼140 ppm of potassium and no radiogenic heat production in the core. Black curve indicates the difference in $F_{\rm CMB}$ between two cases. Middle panel: same as the top panel but for $R_{\rm ic}$. Bottom panel: ages of core dynamo with 4 levels of k_c and two levels of radiogenic heat production in the core. The lifetime of the core dynamo is capped at 12 Gyr.

of these planets. Hence, for the same decrease in $T_{\rm CMB}$, $R_{\rm ic}$ increases more in planets with lower CMFs. For example, at 10 Gyr, $R_{\rm ic}$ would increase by $\sim$2.97 km as $T_{\rm CMB}$ by 1 K in the $3M_\oplus$ planet with CMF=0.1, and by $\sim$1.2 km in the $3M_\oplus$ planet with CMF=0.8.

The exact amount of radiogenic heating in the iron-dominated core of rocky exoplanets depends on the abundance of radioactive elements in the host stars, planet composition and the planet formation process. In particular, the stellar abundance limits the maximum amount of radiogenic elements that could be present in the planet. The partitioning of radiogenic elements between the silicate mantle and iron-dominated core depends on temperature, pressure and the oxygen fugacity of the mantle [e.g., Wilson et al., 2023]. The results shown in this section is a simple exercise to isolate the effect of radiogenic heat production in the core and explore its impact on the thermal and magnetic history of rocky planets quantitatively. A systematic study of radiogenic heat production for a range of planets with different masses, CMFs and compositions is left for the future.

4.5 Conclusion

We developed a 1D thermal evolution model coupled with a Henyey solver to study the effect of planetary mass and core mass fraction on the thermal history of and possible dynamo source regions in exoplanets. We extended the modified mixing length theory and applied it to model the convective heat flow within 1- and 2-phase regions in the silicate mantle. Here, we offer a summary on the thermal evolution and dynamo source region results.

1. The heat loss rate of the core, $F_{\rm CMB}$, is predicted to increase with increasing planet mass. In cases where the convection shuts off before the liquid core fully solidifies, the predicted lifetime of the core dynamo increases with increasing planet mass, due to elevated levels of $F_{\rm CMB}$. In cases where the liquid core where fully solidifies before convection shuts off, the lifetime of the dynamo is limited by the age of the liquid core. The predicted lifetime of the core dynamo decreases with increasing planet mass, as

the solid core grows faster due to the elevated $F_{\rm CMB}$.

2. Given the same planet mass, the heat loss rates of cores in planets with various CMFs are comparable. However, more heat can be transported in the liquid cores in the form of thermal conduction in cases with higher CMFs, owing to steeper adiabatic temperature gradients at the CMB of these planets. Hence, convection tends to shut off earlier in planets with higher CMFs, resulting in shorter predicted lifetimes of the core dynamo for these planets.

3. Varying the thermal conductivity of iron, k_c, within its uncertainty range may change the lifetime of the dynamo in the liquid core. For example, for a $3M_\oplus$ planet with a CMF of 0.4, the lifetime of the core dynamo driven by thermal convection alone decreases from over 12 Gyr to ∼11.5 Gyr, ∼8 Gyr and ∼5.5 Gyr when k_c increases from 40 $\mathrm{Wm^{-1}K^{-1}}$ to 80 $\mathrm{Wm^{-1}K^{-1}}$, 120 $\mathrm{Wm^{-1}K^{-1}}$ and 160 $\mathrm{Wm^{-1}K^{-1}}$. However, the dynamo lifetime is limited by the age of the liquid core in cases where the liquid core fully solidifies before convection shuts off. Thus varying k_c in this case has no effect on the dynamo lifetime.

4. Mantle viscosity is the most uncertain thermophysical property in our model. The predicted lifetime of the core dynamo sensitively depends on the choice of the model for mantle viscosity. For example, with lower-bound rheology for post-perovskite (the fiducial choice), the lifetime of the core dynamo driven by thermal convection is ∼8 Gyr with $k_c = 120\mathrm{Wm^{-1}K^{-1}}$ for the case with $M_{\rm pl}$=$3M_\oplus$ and CMF=0.4. However, the lifetime reduces to ∼5.5 Gyr with the upper-bound rheology for post-perovskite. Some recent studies suggest that mantle viscosity in large rocky planets may be low at depth, as post-perovskite dissociates into MgO and $\mathrm{MgSi_2O_5}$. The exact viscosity of this mixture depends on the volumetric fraction of MgO. Experimental and/or numerical study of the viscosity of such a mixture at extreme pressure levels (> 0.9 TPa) will be

necessary to improve predictions of the thermal and magnetic history of large rocky exoplanets.

5. More and less radiogenic heat production in the core results in longer and shorter lifetime of the core dynamo respectively. For example, with $k_c = 120\mathrm{Wm}^{-1}\mathrm{K}^{-1}$, the predicted lifetimes of the core dynamo for a $3M_\oplus$ planet with a CMF of 0.4 are $\sim$7.86 Gyr and $\sim$6.85 Gyr for cases with $\sim$140 ppm and no potassium in the core. However, the exact abundance of radiogenic elements in the core depends on their abundance in host stars, partitioning of these elements between the metallic core and the silicate mantle, as well as planet formation history.

The thermal and dynamo histories of rocky planets are subtle and complex. In this work, we isolate the effect of planet mass and core mass fraction on planet thermal and magnetic history. We also conduct a simple exercise to quantify the effect of uncertainty in mantle viscosity and radiogenic heat production in the core on the predicted dynamo lifetime. In addition, the model can be readily extended to enable a broader exploration of planet parameter space by including additional EOSs for other bulk compositions, investigating various atmospheric boundary conditions, and considering different convection regimes (e.g., mobile-/sluggish-lid convection). Ultimately, we aim to develop the code presented here into a premier modeling tool to help guide and interpret observational searches for strong planetary-scale magnetic fields on low-mass exoplanets.

CHAPTER 5

FUTURE WORK

In this chapter, we discuss various ways to further improve the current thermal evolution model for exoplanets and a few directions we can utilize the model to study planet evolution. We provide a brief description of these ideas in the rest of the chapter.

5.1 Dynamo source region in sub-Neptunes

A decade of space-based exoplanet searches have revealed that the most common planets in the galaxy are ones with mass smaller than Neptune (sub-Neptunes) and larger than Earth (super-Earths) [e.g., Borucki et al., 2011, Thompson et al., 2018]. Moreover, these planets have been resolved into two distinct sub-populations: sub-Neptunes seem to have an extended gaseous envelope, while super-Earths are primarily rocky with a negligible gas envelope.

The next major advance in our thermal model is to incorporate the effect of a primordial H/He envelope. The goal is to simulate the concomitant thermal evolution of both the gas envelope and the rock interior to explore the possibility of the planet hosting a dynamo source in its iron-dominated core and/or magma ocean. On one hand, the gas envelope may impede the convection in the core and cause the dynamo action to stop; on the other hand, the temperature and pressure conditions may be such that silicates near the interior/envelope boundary are molten and thus the magma ocean could host a dynamo. In particular, we will consider two scenarios: 1) a simple case of 3 distinct layers (iron-dominated core/silicate mantle/gas envelope); 2) a case allowing mixing between rock and volatiles. One application of the new thermal model is to interpret the magnetic field detection of a Neptune-sized exoplanet, HAT-P-11 b [Ben-Jaffel et al., 2022], and constrain the geometry of its dynamo source region.

5.2 Dynamo source region in lava planets

Lava planets are exoplanets with extremely high equilibrium temperature and their rocky surface melts into a magma ocean. These are one of the best candidates of terrestrial planets for which detailed characterization is currently feasible with the James Webb Space Telescope, and they provide unique opportunities to learn about magma oceans via remote sensing rather than geophysical modelling. These planets are expected to be tidally locked, which results in a permanent day-side with surface temperature exceeding 2000 K and a permanent night-side with a temperature of several hundred kelvin.

Magnetic fields could be important for the atmosphere of lava planets because thermal ionization ensures that the atmosphere is tightly coupled to the planetary magnetic field. At the very least, this leads to magnetic drag (slower winds) and ohmic dissipation (local warming of the atmosphere); in more extreme cases the atmospheric dynamics could be the realm of magnetohydrodynamics. As an initial exploration of the possibility of these planets hosting a dynamo, we will couple two 1-D models, one for the day-side hemisphere and the other one for the night-side hemisphere. The boundary conditions at the top of the two 1D columns would reflect the temperatures of the day- and night-side. The two 1-D models for the iron-dominated core would be shared, as temperature gradients along the core mantle boundary is small.

5.3 Mantle minerology of rocky exoplanets

As an initial step to assess the dependence of the lifetime of core dynamo on $M_{\rm pl}$ and CMF, we assumed a 1:1 Mg/Si ratio and ignore possible pressure induced phases of silicate beyond post-perovskite. In addition, we considered no other elements such as Al, Ca and Fe in the mantle. However, the exact composition of mantles in exoplanets should reflect those of the host stars and planet formation processes. By adopting EoSs for various compositions, we

will be able to explore the impact of various mantle compositions on mantle dynamics and planet magnetic history. Here, we list a few of these possible effects.

The thermal and magnetic history of a planet are strongly influenced by its radial viscosity profile, which is determined by the rheological properties of the constituent minerals. Adopting two end-member rheologies for post-perovskite predicted by Ammann et al. [2010] and Tackley et al. [2013], we demonstrated the impact of the uncertainty in mantle viscosity could have on the predicted lifetime of the core dynamo in rocky planets. Mantle composition may add additional uncertainty to mantle viscosity estimates. In general, oxides such as MgO and FeO are weaker than silicates. It has been proposed that Ca- and Mg-post-perovskite could dissociate into (Mg,Ca)O and $(Mg, Ca)Si_2O_5$ between 600-900 GPa, and $MgSi_2O_5$ could further dissociate into MgO and SiO_2 at $\sim$2.1 TPa [Umemoto and Wentzcovitch, 2011]. As a result, the viscosity of the deep mantle of rocky exoplanets may decrease as planet mass increases, owing to the increasing volume fraction of oxides. An accurate description of viscosity of mantle silicate with various compositions will be necessary to further improve our prediction in the planet thermal history and dynamo lifetime.

As the magma ocean solidifies, Fe and trace elements could exsolve into the magma ocean and affect the mantle dynamics. The new solid that forms at the solid/liquid boundary at later times during the solidification has a higher concentration in Fe and the trace elements, which would influence its density. This may lead to a gravitationally unstable density profile with denser material at the top compared to the bottom of the solid mantle. Consequently, cold dense material may sink to the bottom of the mantle and light material may float up. The mass transfer may transport additional heat from the deep interior to the surface in addition to convective heat transfer considered in our model. We need a realistic compositional model coupled with our thermal evolution model to study the feedback between mantle dynamics and chemical compositions.

REFERENCES

Y. Abe. Early evolution of the terrestrial planets. Journal of Physics of the Earth, 43(4): 515–532, Jan 1995.

Yutaka Abe. Thermal and chemical evolution of the terrestrial magma ocean. Physics of the Earth and Planetary Interiors, 100(1):27–39, March 1997. doi:10.1016/S0031-9201(96)03229-3.

E. R. Adams, S. Seager, and L. Elkins-Tanton. Ocean Planet or Thick Atmosphere: On the Mass-Radius Relationship for Solid Exoplanets with Massive Atmospheres. , 673(2): 1160–1164, February 2008. doi:10.1086/524925.

Artyom Aguichine, Olivier Mousis, Magali Deleuil, and Emmanuel Marcq. Mass-Radius Relationships for Irradiated Ocean Planets. , 914(2):84, June 2021. doi:10.3847/1538-4357/abfa99.

F. Alibay, J. C. Kasper, J. Lazio, and T. L. Neilsen. SunRISE Mission Concept Step 2 Study Status. In AGU Fall Meeting Abstracts, volume 2017, pages A41I–2410, Dec 2017.

L. V. Al'Tshuler, S. E. Brusnikin, and E. A. Kuz'menkov. Isotherms and Grüneisen functions for 25 metals. Journal of Applied Mechanics and Technical Physics, 28(1):129–141, Jan 1987. doi:10.1007/BF00918785.

M. W. Ammann, J. P. Brodholt, J. Wookey, and D. P. Dobson. First-principles constraints on diffusion in lower-mantle minerals and a weak D" layer. , 465(7297):462–465, May 2010. doi:10.1038/nature09052.

Orson L. Anderson and Al Duba. Experimental melting curve of iron revisited. , 102(B10): 22,659–22,669, October 1997. doi:10.1029/97JB01641.

Lotfi Ben-Jaffel, Gilda E. Ballester, Antonio García Muñoz, Panayotis Lavvas, David K. Sing, Jorge Sanz-Forcada, Ofer Cohen, Tiffany Kataria, Gregory W. Henry, Lars Buchhave, Thomas Mikal-Evans, Hannah R. Wakeford, and Mercedes López-Morales. Signatures of strong magnetization and a metal-poor atmosphere for a Neptune-sized exoplanet. Nature Astronomy, 6:141–153, January 2022. doi:10.1038/s41550-021-01505-x.

Francis Birch. Elasticity and Constitution of the Earth's Interior. , 57(2):227–286, Jun 1952. doi:10.1029/JZ057i002p00227.

Ingrid Blanchard, Julien Siebert, Stephan Borensztajn, and James Badro. The solubility of heat-producing elements in earth's core. Geochemical Perspectives Letters, 5:1–5, 10 2017. doi:10.7185/geochemlet.1737.

C. H. Blaske and J. G. O'Rourke. Energetic Requirements for Dynamos in the Metallic Cores of Super-Earth and Super-Venus Exoplanets. Journal of Geophysical Research (Planets), 126(7):e06739, July 2021. doi:10.1029/2020JE006739.

Irene Bonati, Marine Lasbleis, and Lena Noack. Structure and Thermal Evolution of Exoplanetary Cores. Journal of Geophysical Research (Planets), 126(5):e06724, May 2021. doi:10.1029/2020JE006724.

Richard K. Bono, John A. Tarduno, Francis Nimmo, and Rory D. Cottrell. Young inner core inferred from Ediacaran ultra-low geomagnetic field intensity. Nature Geoscience, 12(2): 143–147, January 2019. doi:10.1038/s41561-018-0288-0.

William J. Borucki, David G. Koch, Gibor Basri, Natalie Batalha, Alan Boss, Timothy M. Brown, Douglas Caldwell, Jørgen Christensen-Dalsgaard, William D. Cochran, Edna DeVore, Edward W. Dunham, Andrea K. Dupree, III Gautier, Thomas N., John C. Geary, Ronald Gilliland, Alan Gould, Steve B. Howell, Jon M. Jenkins, Hans Kjeldsen, David W. Latham, Jack J. Lissauer, Geoffrey W. Marcy, David G. Monet, Dimitar Sasselov, Jill Tarter, David Charbonneau, Laurance Doyle, Eric B. Ford, Jonathan Fortney, Matthew J. Holman, Sara Seager, Jason H. Steffen, William F. Welsh, Christopher Allen, Stephen T. Bryson, Lars Buchhave, Hema Chandrasekaran, Jessie L. Christiansen, David Ciardi, Bruce D. Clarke, Jessie L. Dotson, Michael Endl, Debra Fischer, Francois Fressin, Michael Haas, Elliott Horch, Andrew Howard, Howard Isaacson, Jeffery Kolodziejczak, Jie Li, Phillip MacQueen, Søren Meibom, Andrej Prsa, Elisa V. Quintana, Jason Rowe, William Sherry, Peter Tenenbaum, Guillermo Torres, Joseph D. Twicken, Jeffrey Van Cleve, Lucianne Walkowicz, and Hayley Wu. Characteristics of Kepler Planetary Candidates Based on the First Data Set. , 728(2):117, February 2011. doi:10.1088/0004-637X/728/2/117.

A. Boujibar, P. Driscoll, and Y. Fei. Super-Earth Internal Structures and Initial Thermal States. Journal of Geophysical Research (Planets), 125(5):e06124, May 2020. doi:10.1029/2019JE006124.

Dan J. Bower, Patrick Sanan, and Aaron S. Wolf. Numerical solution of a non-linear conservation law applicable to the interior dynamics of partially molten planets. Physics of the Earth and Planetary Interiors, 274:49–62, January 2018. doi:10.1016/j.pepi.2017.11.004.

Dan J. Bower, Daniel Kitzmann, Aaron S. Wolf, Patrick Sanan, Caroline Dorn, and Apurva V. Oza. Linking the evolution of terrestrial interiors and an early outgassed atmosphere to astrophysical observations. , 631:A103, November 2019. doi:10.1051/0004-6361/201935710.

B. F. Burke and K. L. Franklin. Observations of a Variable Radio Source Associated with the Planet Jupiter. , 60(2):213–217, Jun 1955. doi:10.1029/JZ060i002p00213.

U. R. Christensen. Dynamo Scaling Laws and Applications to the Planets. , 152(1-4): 565–590, May 2010. doi:10.1007/s11214-009-9553-2.

U. R. Christensen and J. Aubert. Scaling properties of convection-driven dynamos in rotating spherical shells and application to planetary magnetic fields. Geophysical Journal International, 166(1):97–114, July 2006. doi:10.1111/j.1365-246X.2006.03009.x.

Ulrich R. Christensen, Volkmar Holzwarth, and Ansgar Reiners. Energy flux determines magnetic field strength of planets and stars. , 457(7226):167–169, January 2009. doi:10.1038/nature07626.

J. H. Davies and D. R. Davies. Earth's surface heat flux. Solid Earth, 1(1):5–24, February 2010. doi:10.5194/se-1-5-2010.

Nico de Koker, Gerd Steinle-Neumann, and Vojtěch Vlček. Electrical resistivity and thermal conductivity of liquid Fe alloys at high P and T, and heat flux in Earth's core. Proceedings of the National Academy of Science, 109(11):4070–4073, Mar 2012. doi:10.1073/pnas.1111841109.

Agnès Dewaele, Paul Loubeyre, Florent Occelli, Mohamed Mezouar, Peter I. Dorogokupets, and Marc Torrent. Quasihydrostatic Equation of State of Iron above 2Mbar. , 97(21): 215504, Nov 2006. doi:10.1103/PhysRevLett.97.215504.

P. I. Dorogokupets, A. M. Dymshits, K. D. Litasov, and T. S. Sokolova. Thermodynamics and Equations of State of Iron to 350 GPa and 6000 K. Scientific Reports, 7:41863, Mar 2017. doi:10.1038/srep41863.

P. Driscoll and D. Bercovici. On the thermal and magnetic histories of Earth and Venus: Influences of melting, radioactivity, and conductivity. Physics of the Earth and Planetary Interiors, 236:36–51, November 2014. doi:10.1016/j.pepi.2014.08.004.

P. Driscoll and C. Davies. The "new core paradox": Challenges and potential solutions. Journal of Geophysical Research: Solid Earth, 128(1):e2022JB025355, 2023. doi:https://doi.org/10.1029/2022JB025355. URL `https://agupubs.onlinelibrary.wiley.com/doi/abs/10.1029/2022JB025355`. e2022JB025355 2022JB025355.

Adam M. Dziewonski and Don L. Anderson. Preliminary reference Earth model. Physics of the Earth and Planetary Interiors, 25(4):297–356, Jun 1981. doi:10.1016/0031-9201(81)90046-7.

L. T. Elkins-Tanton. Linked magma ocean solidification and atmospheric growth for Earth and Mars. Earth and Planetary Science Letters, 271(1-4):181–191, July 2008. doi:10.1016/j.epsl.2008.03.062.

S. W. Ellingson, T. E. Clarke, A. Cohen, J. Craig, N. E. Kassim, Y. Pihlstrom, L. J. Rickard, and G. B. Taylor. The Long Wavelength Array. IEEE Proceedings, 97(8):1421–1430, August 2009. doi:10.1109/JPROC.2009.2015683.

Y. Fei, J. van Orman, J. Li, W. van Westrenen, C. Sanloup, W. Minarik, K. Hirose, T. Komabayashi, M. Walter, and K. Funakoshi. Experimentally determined postspinel transformation boundary in Mg_2SiO_4 using MgO as an internal pressure standard and its geophysical implications. Journal of Geophysical Research (Solid Earth), 109(B2):B02305, Feb 2004. doi:10.1029/2003JB002562.

C. C. Finlay, S. Maus, C. D. Beggan, T. N. Bondar, A. Chambodut, T. A. Chernova, A. Chulliat, V. P. Golovkov, B. Hamilton, and M. Hamoudi. International Geomagnetic Reference Field: the eleventh generation. Geophysical Journal International, 183(3):1216–1230, Dec 2010. doi:10.1111/j.1365-246X.2010.04804.x.

G. Fiquet, A. L. Auzende, J. Siebert, A. Corgne, H. Bureau, H. Ozawa, and G. Garbarino. Melting of Peridotite to 140 Gigapascals. Science, 329(5998):1516, September 2010. doi:10.1126/science.1192448.

Rebecca A. Fischer, Andrew J. Campbell, Razvan Caracas, Daniel M. Reaman, Przymyslaw Dera, and Vitali B. Prakapenka. Equation of state and phase diagram of Fe-16Si alloy as a candidate component of Earth's core. Earth and Planetary Science Letters, 357:268–276, December 2012. doi:10.1016/j.epsl.2012.09.022.

S. E. Gelman, L. T. Elkins-Tanton, and S. Seager. Effects of Stellar Flux on Tidally Locked Terrestrial Planets: Degree-1 Mantle Convection and Local Magma Ponds. , 735(2):72, July 2011. doi:10.1088/0004-637X/735/2/72.

C. K. Gessmann and B. J. Wood. Potassium in the Earth's core? Earth and Planetary Science Letters, 200(1-2):63–78, June 2002. doi:10.1016/S0012-821X(02)00593-9.

Herbert Gunell, Romain Maggiolo, Hans Nilsson, Gabriella Stenberg Wieser, Rikard Slapak, Jesper Lindkvist, Maria Hamrin, and Johan De Keyser. Why an intrinsic magnetic field does not protect a planet against atmospheric escape. , 614:L3, Jun 2018. doi:10.1051/0004-6361/201832934.

G. Hallinan, S. K. Sirothia, A. Antonova, C. H. Ishwara-Chand ra, S. Bourke, J. G. Doyle, J. Hartman, and A. Golden. Looking for a Pulse: A Search for Rotationally Modulated Radio Emission from the Hot Jupiter, τ Boötis b. , 762(1):34, Jan 2013. doi:10.1088/0004-637X/762/1/34.

R. J. Hemley, L. Stixrude, Y. Fei, and H. K. Mao. Constraints on lower mantle composition from P-V-T measurements of (Fe, Mg)SiO_3-perovskite and (Fe, Mg)O. Washington DC American Geophysical Union Geophysical Monograph Series, 67:183–189, January 1992. doi:10.1029/GM067p0183.

L. G. Henyey, L. Wilets, K. H. Böhm, R. Lelevier, and R. D. Levee. A Method for Automatic Computation of Stellar Evolution. , 129:628, May 1959. doi:10.1086/146661.

P. C. Hess. Komatities and the Archean Mantle. In Lunar and Planetary Science Conference, volume 21 of Lunar and Planetary Science Conference, page 501, March 1990.

Naohisa Hirao, Eiji Ohtani, Tadashi Kondo, Noriaki Endo, Toshiko Kuba, Toshiaki Suzuki, and Takumi Kikegawa. Partitioning of potassium between iron and silicate at the core-mantle boundary. , 33(8):L08303, April 2006. doi:10.1029/2005GL025324.

S. Honda, D. A. Yuen, S. Balachandar, and D. Reuteler. Three-Dimensional Instabilities of Mantle Convection with Multiple Phase Transitions. Science, 259(5099):1308–1311, Feb 1993. doi:10.1126/science.259.5099.1308.

Chenliang Huang, David R. Rice, and Jason H. Steffen. MAGRATHEA: an open-source spherical symmetric planet interior structure code. , 513(4):5256–5269, July 2022. doi:10.1093/mnras/stac1133.

Hayato Inoue, Sho Suehiro, Kenji Ohta, Kei Hirose, and Yasuo Ohishi. Resistivity saturation of hcp Fe-Si alloys in an internally heated diamond anvil cell: A key to assessing the Earth's core conductivity. Earth and Planetary Science Letters, 543:116357, August 2020. doi:10.1016/j.epsl.2020.116357.

Melodie M. Kao, Gregg Hallinan, J. Sebastian Pineda, David Stevenson, and Adam Burgasser. The Strongest Magnetic Fields on the Coolest Brown Dwarfs. The Astrophysical Journal Supplement Series, 237:25, Aug 2018. doi:10.3847/1538-4365/aac2d5.

M. G. Kivelson, K. K. Khurana, C. T. Russell, R. J. Walker, J. Warnecke, F. V. Coroniti, C. Polanskey, D. J. Southwood, and G. Schubert. Discovery of Ganymede's magnetic field by the Galileo spacecraft. , 384(6609):537–541, Dec 1996. doi:10.1038/384537a0.

Zuzana Konôpková, R. Stewart McWilliams, Natalia Gómez-Pérez, and Alexander F. Goncharov. Direct measurement of thermal conductivity in solid iron at planetary core conditions. , 534(7605):99–101, Jun 2016. doi:10.1038/nature18009.

S. Labrosse, J. W. Hernlund, and N. Coltice. A crystallizing dense magma ocean at the base of the Earth's mantle. , 450(7171):866–869, December 2007. doi:10.1038/nature06355.

Stéphane Labrosse. Thermal evolution of the core with a high thermal conductivity. Physics of the Earth and Planetary Interiors, 247:36–55, October 2015. doi:10.1016/j.pepi.2015.02.002.

T. Lebrun, H. Massol, E. ChassefièRe, A. Davaille, E. Marcq, P. Sarda, F. Leblanc, and G. Brandeis. Thermal evolution of an early magma ocean in interaction with the atmosphere. Journal of Geophysical Research (Planets), 118(6):1155–1176, June 2013. doi:10.1002/jgre.20068.

Rickard Lundin, Helmut Lammer, and Ignasi Ribas. Planetary Magnetic Fields and Solar Forcing: Implications for Atmospheric Evolution. , 129(1-3):245–278, Mar 2007. doi:10.1007/s11214-007-9176-4.

W. F. McDonough and S. s. Sun. The composition of the Earth. Chemical Geology, 120 (3-4):223–253, March 1995. doi:10.1016/0009-2541(94)00140-4.

J. Monteux, A. M. Jellinek, and C. L. Johnson. Why might planets and moons have early dynamos? Earth and Planetary Science Letters, 310(3):349–359, October 2011. doi:10.1016/j.epsl.2011.08.014.

G. Morard, J. Bouchet, D. Valencia, S. Mazevet, and F. Guyot. The melting curve of iron at extreme pressures: Implications for planetary cores. High Energy Density Physics, 7 (3):141–144, September 2011. doi:10.1016/j.hedp.2011.02.001.

Jed L. Mosenfelder, Paul D. Asimow, Daniel J. Frost, David C. Rubie, and Thomas J. Ahrens. The $MgSiO_3$ system at high pressure: Thermodynamic properties of perovskite, postperovskite, and melt from global inversion of shock and static compression data. Journal of Geophysical Research (Solid Earth), 114(B1):B01203, January 2009. doi:10.1029/2008JB005900.

V. Rama Murthy, Wim van Westrenen, and Yingwei Fei. Experimental evidence that potassium is a substantial radioactive heat source in planetary cores. , 423(6936):163–165, May 2003. doi:10.1038/nature01560.

N. F. Ness, K. W. Behannon, R. P. Lepping, and Y. C. Whang. Magnetic field of Mercury confirmed. , 255(5505):204–205, May 1975. doi:10.1038/255204a0.

N. F. Ness, M. H. Acuna, K. W. Behannon, L. F. Burlaga, J. E. P. Connerney, R. P. Lepping, and Fritz M. Neubauer. Magnetic Fields at Uranus. Science, 233(4759):85–89, Jul 1986. doi:10.1126/science.233.4759.85.

Norman F. Ness, Mario H. Acuna, Leonard F. Burlaga, John E. P. Connerney, Ronald P. Lepping, and Fritz M. Neubauer. Magnetic Fields at Neptune. Science, 246(4936):1473–1478, Dec 1989. doi:10.1126/science.246.4936.1473.

Francis Nimmo, Joel Primack, S. M. Faber, Enrico Ramirez-Ruiz, and Mohammadtaher Safarzadeh. Radiogenic Heating and Its Influence on Rocky Planet Dynamos and Habitability. , 903(2):L37, November 2020. doi:10.3847/2041-8213/abc251.

Artem R. Oganov and Shigeaki Ono. Theoretical and experimental evidence for a post-perovskite phase of $MgSiO_3$ in Earth's D" layer. , 430(6998):445–448, July 2004. doi:10.1038/nature02701.

Kenji Ohta, Yasuhiro Kuwayama, Kei Hirose, Katsuya Shimizu, and Yasuo Ohishi. Experimental determination of the electrical resistivity of iron at Earth's core conditions. , 534 (7605):95–98, Jun 2016. doi:10.1038/nature17957.

Andreea M. Papuc and Geoffrey F. Davies. The internal activity and thermal evolution of Earth-like planets. , 195(1):447–458, May 2008. doi:10.1016/j.icarus.2007.12.016.

L. V. Pourovskii, J. Mravlje, M. Pozzo, and D. Alfè. Electronic correlations and transport in iron at Earth's core conditions. Nature Communications, 11:4105, August 2020. doi:10.1038/s41467-020-18003-9.

Monica Pozzo, Chris Davies, David Gubbins, and Dario Alfè. Thermal and electrical conductivity of iron at Earth's core conditions. , 485(7398):355–358, May 2012. doi:10.1038/nature11031.

Monica Pozzo, Chris Davies, David Gubbins, and Dario Alfè. Thermal and electrical conductivity of solid iron and iron-silicon mixtures at Earth's core conditions. Earth and Planetary Science Letters, 393:159–164, May 2014. doi:10.1016/j.epsl.2014.02.047.

Giorgio Ranalli. Mantle rheology: radial and lateral viscosity variations inferred from microphysical creep laws. Journal of Geodynamics, 32(4):425–444, Dec 2001. doi:10.1016/S0264-3707(01)00042-4.

L. A. Rogers and S. Seager. A Framework for Quantifying the Degeneracies of Exoplanet Interior Compositions. , 712(2):974–991, Apr 2010. doi:10.1088/0004-637X/712/2/974.

Yaakov Rosenfeld and Pedro Tarazona. Density functional theory and the asymptotic high density expansion of the free energy of classical solids and fluids. Molecular Physics, 95 (2):141–150, October 1998. doi:10.1080/00268979809483145.

Sho Sasaki and Kiyoshi Nakazawa. Metal-silicate fractionation in the growing Earth: Energy source for the terrestrial magma ocean. Journal of Geophysical Research, 91:9231–9238, August 1986a. doi:10.1029/JB091iB09p09231.

Sho Sasaki and Kiyoshi Nakazawa. Metal-silicate fractionation in the growing Earth: Energy source for the terrestrial magma ocean. , 91(B9):9231–9238, Aug 1986b. doi:10.1029/JB091iB09p09231.

Hiroki Senshu, Kiyoshi Kuramoto, and Takafumi Matsui. Thermal evolution of a growing Mars. Journal of Geophysical Research (Planets), 107(E12):5118, Dec 2002. doi:10.1029/2001JE001819.

E. J. Smith, L. Davis, D. E. Jones, P. J. Coleman, D. S. Colburn, P. Dyal, and C. P. Sonett. Saturn's Magnetic Field and Magnetosphere. Science, 207(4429):407–410, Jan 1980. doi:10.1126/science.207.4429.407.

V. Solomatov. 9.04 - magma oceans and primordial mantle differentiation. In Gerald Schubert, editor, Treatise on Geophysics (Second Edition), pages 81–104. Elsevier, Oxford, second edition edition, 2015. ISBN 978-0-444-53803-1. doi:https://doi.org/10.1016/B978-0-444-53802-4.00155-X. URL https://www.sciencedirect.com/science/article/pii/B978044453802400155X.

C. Sotin, O. Grasset, and A. Mocquet. Mass radius curve for extrasolar Earth-like planets and ocean planets. , 191(1):337–351, November 2007. doi:10.1016/j.icarus.2007.04.006.

François Soubiran and Burkhard Militzer. Electrical conductivity and magnetic dynamos in magma oceans of Super-Earths. Nature Communications, 9:3883, Sep 2018. doi:10.1038/s41467-018-06432-6.

Frank J. Spera, Mark S. Ghiorso, and Dean Nevins. Structure, thermodynamic and transport properties of liquid MgSiO $_3$: Comparison of molecular models and laboratory results. , 75(5):1272–1296, March 2011. doi:10.1016/j.gca.2010.12.004.

Frank D. Stacey and Paul M. Davis. Physics of the Earth. 2008.

Vlada Stamenković, Doris Breuer, and Tilman Spohn. Thermal and transport properties of mantle rock at high pressure: Applications to super-Earths. , 216:572–596, December 2011. doi:10.1016/j.icarus.2011.09.030.

Vlada Stamenković, Lena Noack, Doris Breuer, and Tilman Spohn. The Influence of Pressure-dependent Viscosity on the Thermal Evolution of Super-Earths. , 748(1):41, March 2012. doi:10.1088/0004-637X/748/1/41.

Sabine Stanley and Gary A. Glatzmaier. Dynamo Models for Planets Other Than Earth. , 152(1-4):617–649, May 2010. doi:10.1007/s11214-009-9573-y.

D. J. Stevenson, T. Spohn, and G. Schubert. Magnetism and thermal evolution of the terrestrial planets. , 54(3):466–489, Jun 1983. doi:10.1016/0019-1035(83)90241-5.

David J. Stevenson. Planetary Magnetic Fields: Achievements and Prospects. , 152(1-4): 651–664, May 2010. doi:10.1007/s11214-009-9572-z.

L. Stixrude. Melting in super-earths. Philosophical Transactions of the Royal Society of London Series A, 372(2014):20130076–20130076, March 2014. doi:10.1098/rsta.2013.0076.

Lars Stixrude, Roberto Scipioni, and Michael P. Desjarlais. A silicate dynamo in the early Earth. Nature Communications, 11:935, February 2020. doi:10.1038/s41467-020-14773-4.

Terry-Ann Suer, Julien Siebert, Laurent Remusat, James M. D. Day, Stephan Borensztajn, Beatrice Doisneau, and Guillaume Fiquet. Reconciling metal-silicate partitioning and late accretion in the Earth. Nature Communications, 12:2913, January 2021. doi:10.1038/s41467-021-23137-5.

Ningyu Sun, Wei Wei, Shunjie Han, Junhao Song, Xinyang Li, Yunfei Duan, Vitali B. Prakapenka, and Zhu Mao. Phase transition and thermal equations of state of (Fe,Al)-bridgmanite and post-perovskite: Implication for the chemical heterogeneity at the lowermost mantle. Earth and Planetary Science Letters, 490:161–169, May 2018. doi:10.1016/j.epsl.2018.03.004.

C. Tachinami, H. Senshu, and S. Ida. Thermal Evolution and Lifetime of Intrinsic Magnetic Fields of Super-Earths in Habitable Zones. , 726(2):70, Jan 2011. doi:10.1088/0004-637X/726/2/70.

P. J. Tackley, M. Ammann, J. P. Brodholt, D. P. Dobson, and D. Valencia. Mantle dynamics in super-Earths: Post-perovskite rheology and self-regulation of viscosity. , 225(1):50–61, July 2013. doi:10.1016/j.icarus.2013.03.013.

Susan E. Thompson, Jeffrey L. Coughlin, Kelsey Hoffman, Fergal Mullally, Jessie L. Christiansen, Christopher J. Burke, Steve Bryson, Natalie Batalha, Michael R. Haas, Joseph Catanzarite, Jason F. Rowe, Geert Barentsen, Douglas A. Caldwell, Bruce D. Clarke,

Jon M. Jenkins, Jie Li, David W. Latham, Jack J. Lissauer, Savita Mathur, Robert L. Morris, Shawn E. Seader, Jeffrey C. Smith, Todd C. Klaus, Joseph D. Twicken, Jeffrey E. Van Cleve, Bill Wohler, Rachel Akeson, David R. Ciardi, William D. Cochran, Christopher E. Henze, Steve B. Howell, Daniel Huber, Andrej Prša, Solange V. Ramírez, Timothy D. Morton, Thomas Barclay, Jennifer R. Campbell, William J. Chaplin, David Charbonneau, Jørgen Christensen-Dalsgaard, Jessie L. Dotson, Laurance Doyle, Edward W. Dunham, Andrea K. Dupree, Eric B. Ford, John C. Geary, Forrest R. Girouard, Howard Isaacson, Hans Kjeldsen, Elisa V. Quintana, Darin Ragozzine, Megan Shabram, Avi Shporer, Victor Silva Aguirre, Jason H. Steffen, Martin Still, Peter Tenenbaum, William F. Welsh, Angie Wolfgang, Khadeejah A. Zamudio, David G. Koch, and William J. Borucki. Planetary Candidates Observed by Kepler. VIII. A Fully Automated Catalog with Measured Completeness and Reliability Based on Data Release 25. , 235(2):38, April 2018. doi:10.3847/1538-4365/aab4f9.

Jake D. Turner, Philippe Zarka, Jean-Mathias Grießmeier, Joseph Lazio, Baptiste Cecconi, J. Emilio Enriquez, Julien N. Girard, Ray Jayawardhana, Laurent Lamy, Jonathan D. Nichols, and Imke de Pater. The search for radio emission from the exoplanetary systems 55 Cancri, υ Andromedae, and τ Boötis using LOFAR beam-formed observations. arXiv e-prints, art. arXiv:2012.07926, December 2020.

Koichiro Umemoto and Renata M. Wentzcovitch. Two-stage dissociation in MgSiO $_3$ post-perovskite. Earth and Planetary Science Letters, 311(3):225–229, November 2011. doi:10.1016/j.epsl.2011.09.032.

C. T. Unterborn and W. R. Panero. The Pressure and Temperature Limits of Likely Rocky Exoplanets. Journal of Geophysical Research (Planets), 124(7):1704–1716, July 2019. doi:10.1029/2018JE005844.

Pierre Vacher, Antoine Mocquet, and Christophe Sotin. Computation of seismic profiles from mineral physics: the importance of the non-olivine components for explaining the 660 km depth discontinuity. Physics of the Earth and Planetary Interiors, 106(3-4):275–298, April 1998. doi:10.1016/S0031-9201(98)00076-4.

Diana Valencia, Richard J. O'Connell, and Dimitar Sasselov. Internal structure of massive terrestrial planets. , 181(2):545–554, Apr 2006. doi:10.1016/j.icarus.2005.11.021.

M. P. van Haarlem, M. W. Wise, A. W. Gunst, G. Heald, J. P. McKean, J. W. T. Hessels, A. G. de Bruyn, R. Nijboer, J. Swinbank, R. Fallows, M. Brentjens, A. Nelles, R. Beck, H. Falcke, R. Fender, J. Hörandel, L. V. E. Koopmans, G. Mann, G. Miley, H. Röttgering, B. W. Stappers, R. A. M. J. Wijers, S. Zaroubi, M. van den Akker, A. Alexov, J. Anderson, K. Anderson, A. van Ardenne, M. Arts, A. Asgekar, I. M. Avruch, F. Batejat, L. Bähren, M. E. Bell, M. R. Bell, I. van Bemmel, P. Bennema, M. J. Bentum, G. Bernardi, P. Best, L. Bîrzan, A. Bonafede, A. J. Boonstra, R. Braun, J. Bregman, F. Breitling, R. H. van de Brink, J. Broderick, P. C. Broekema, W. N. Brouw, M. Brüggen, H. R. Butcher, W. van Cappellen, B. Ciardi, T. Coenen, J. Conway, A. Coolen, A. Corstanje, S. Damstra,

O. Davies, A. T. Deller, R. J. Dettmar, G. van Diepen, K. Dijkstra, P. Donker, A. Doorduin, J. Dromer, M. Drost, A. van Duin, J. Eislöffel, J. van Enst, C. Ferrari, W. Frieswijk, H. Gankema, M. A. Garrett, F. de Gasperin, M. Gerbers, E. de Geus, J. M. Grießmeier, T. Grit, P. Gruppen, J. P. Hamaker, T. Hassall, M. Hoeft, H. A. Holties, A. Horneffer, A. van der Horst, A. van Houwelingen, A. Huijgen, M. Iacobelli, H. Intema, N. Jackson, V. Jelic, A. de Jong, E. Juette, D. Kant, A. Karastergiou, A. Koers, H. Kollen, V. I. Kondratiev, E. Kooistra, Y. Koopman, A. Koster, M. Kuniyoshi, M. Kramer, G. Kuper, P. Lambropoulos, C. Law, J. van Leeuwen, J. Lemaitre, M. Loose, P. Maat, G. Macario, S. Markoff, J. Masters, R. A. McFadden, D. McKay-Bukowski, H. Meijering, H. Meulman, M. Mevius, E. Middelberg, R. Millenaar, J. C. A. Miller-Jones, R. N. Mohan, J. D. Mol, J. Morawietz, R. Morganti, D. D. Mulcahy, E. Mulder, H. Munk, L. Nieuwenhuis, R. van Nieuwpoort, J. E. Noordam, M. Norden, A. Noutsos, A. R. Offringa, H. Olofsson, A. Omar, E. Orrú, R. Overeem, H. Paas, M. Pandey-Pommier, V. N. Pandey, R. Pizzo, A. Polatidis, D. Rafferty, S. Rawlings, W. Reich, J. P. de Reijer, J. Reitsma, G. A. Renting, P. Riemers, E. Rol, J. W. Romein, J. Roosjen, M. Ruiter, A. Scaife, K. van der Schaaf, B. Scheers, P. Schellart, A. Schoenmakers, G. Schoonderbeek, M. Serylak, A. Shulevski, J. Sluman, O. Smirnov, C. Sobey, H. Spreeuw, M. Steinmetz, C. G. M. Sterks, H. J. Stiepel, K. Stuurwold, M. Tagger, Y. Tang, C. Tasse, I. Thomas, S. Thoudam, M. C. Toribio, B. van der Tol, O. Usov, M. van Veelen, A. J. van der Veen, S. ter Veen, J. P. W. Verbiest, R. Vermeulen, N. Vermaas, C. Vocks, C. Vogt, M. de Vos, E. van der Wal, R. van Weeren, H. Weggemans, P. Weltevrede, S. White, S. J. Wijnholds, T. Wilhelmsson, O. Wucknitz, S. Yatawatta, P. Zarka, A. Zensus, and J. van Zwieten. LOFAR: The LOw-Frequency ARray. , 556:A2, August 2013. doi:10.1051/0004-6361/201220873.

Pascal Vinet, James H. Rose, John Ferrante, and John R. Smith. Universal features of the equation of state of solids. Journal of Physics Condensed Matter, 1(11):1941–1963, March 1989. doi:10.1088/0953-8984/1/11/002.

E. Vitense. Die Wasserstoffkonvektionszone der Sonne. Mit 11 Textabbildungen. , 32:135, January 1953.

F. W. Wagner, F. Sohl, H. Hussmann, M. Grott, and H. Rauer. Interior structure models of solid exoplanets using material laws in the infinite pressure limit. , 214(2):366–376, August 2011. doi:10.1016/j.icarus.2011.05.027.

F. W. Wagner, A. C. Plesa, and A. B. Rozel. Calibrating mixing-length theory for thermal convection in rocky planets. Geophysical Journal International, 217(1):75–89, Apr 2019. doi:10.1093/gji/ggy543.

Kosui Watanabe, Eiji Ohtani, Seiji Kamada, Tatsuya Sakamaki, Masaaki Miyahara, and Yoshinori Ito. The abundance of potassium in the Earth's core. Physics of the Earth and Planetary Interiors, 237:65–72, December 2014. doi:10.1016/j.pepi.2014.10.001.

Alfred J. Wilson, Monica Pozzo, Christopher J. Davies, Andrew M. Walker, and Dario Alfè. Examining the power supplied to Earth's dynamo by magnesium precipitation and

radiogenic heat production. Physics of the Earth and Planetary Interiors, 343:107073, October 2023. doi:10.1016/j.pepi.2023.107073.

D. Winterhalter, T. Kuiper, W. Majid, I. Chandra, J. Lazio, P. Zarka, C. Naudet, G. Bryden, W. Gonzalez, and R. Treumann. Search for Radio Emissions from Extrasolar Planets: the Observation Campaign. In Planetary Radio Emissions VI, pages 595–602, Jan 2006.

Aaron S. Wolf and Dan J. Bower. An equation of state for high pressure-temperature liquids (RTpress) with application to $MgSiO_3$ melt. Physics of the Earth and Planetary Interiors, 278:59–74, May 2018. doi:10.1016/j.pepi.2018.02.004.

Zhihua Xiong, Taku Tsuchiya, and Takashi Taniuchi. Ab Initio Prediction of Potassium Partitioning Into Earth's Core. Journal of Geophysical Research (Solid Earth), 123(8): 6451–6458, August 2018. doi:10.1029/2018JB015522.

Takesi Yukutake. The inner core and the surface heat flow as clues to estimating the initial temperature of the Earth's core. Physics of the Earth and Planetary Interiors, 121(1-2): 103–137, Sep 2000. doi:10.1016/S0031-9201(00)00163-1.

Philippe Zarka. Plasma interactions of exoplanets with their parent star and associated radio emissions. , 55(5):598–617, Apr 2007. doi:10.1016/j.pss.2006.05.045.

Jisheng Zhang and Leslie A. Rogers. Thermal Evolution and Magnetic History of Rocky Planets. , 938(2):131, October 2022. doi:10.3847/1538-4357/ac8e65.

Youjun Zhang, Mingqiang Hou, Guangtao Liu, Chengwei Zhang, Vitali B. Prakapenka, Eran Greenberg, Yingwei Fei, R. E. Cohen, and Jung-Fu Lin. Reconciliation of experiments and theory on transport properties of iron and the geodynamo. Phys. Rev. Lett., 125:078501, Aug 2020. doi:10.1103/PhysRevLett.125.078501. URL https://link.aps.org/doi/10.1103/PhysRevLett.125.078501.

Youjun Zhang, Kai Luo, Mingqiang Hou, Peter Driscoll, Nilesh P. Salke, Ján Minár, Vitali B. Prakapenka, Eran Greenberg, Russell J. Hemley, R. E. Cohen, and Jung-Fu Lin. Thermal conductivity of fe-si alloys and thermal stratification in earth’s core. Proceedings of the National Academy of Sciences, 119(1):e2119001119, 2022. doi:10.1073/pnas.2119001119. URL https://www.pnas.org/doi/abs/10.1073/pnas.2119001119.

Jorge I. Zuluaga, Sebastian Bustamante, Pablo A. Cuartas, and Jaime H. Hoyos. The Influence of Thermal Evolution in the Magnetic Protection of Terrestrial Planets. , 770 (1):23, June 2013. doi:10.1088/0004-637X/770/1/23.